

2018-01-01

Experimental Laser Powder Bed Fusion System For Difficult To Process Metallic Materials

Syed Zia Uddin

University of Texas at El Paso, syedzia.buet@gmail.com

Follow this and additional works at: https://digitalcommons.utep.edu/open_etd



Part of the [Mechanical Engineering Commons](#), and the [Physics Commons](#)

Recommended Citation

Uddin, Syed Zia, "Experimental Laser Powder Bed Fusion System For Difficult To Process Metallic Materials" (2018). *Open Access Theses & Dissertations*. 17.

https://digitalcommons.utep.edu/open_etd/17

This is brought to you for free and open access by DigitalCommons@UTEP. It has been accepted for inclusion in Open Access Theses & Dissertations by an authorized administrator of DigitalCommons@UTEP. For more information, please contact lweber@utep.edu.

EXPERIMENTAL LASER POWDER BED FUSION SYSTEM FOR DIFFICULT
TO PROCESS METALLIC MATERIALS

SYED ZIA UDDIN

Master's Program in Mechanical Engineering

APPROVED:

Ryan Wicker, Ph.D., Chair

David Espalin, Ph.D.

Amit Lopes, Ph.D.

Charles Ambler, Ph.D.
Dean of the Graduate School

Copyright ©

by

Syed Zia Uddin

2018

Dedication

This thesis is dedicated to my parents and my elder brother

EXPERIMENTAL LASER POWDER BED FUSION SYSTEM FOR DIFFICULT
TO PROCESS MATERIALS

by

SYED ZIA UDDIN, B.S.M.E.

THESIS

Presented to the Faculty of the Graduate School of

The University of Texas at El Paso

in Partial Fulfillment

of the Requirements

for the Degree of

MASTER OF SCIENCE

Department of Mechanical Engineering

THE UNIVERSITY OF TEXAS AT EL PASO

December 2018

Acknowledgements

I start with thanking Almighty Allah for keeping my ever-fleeting heart steadfast in its goal. My heartfelt thanks and respect to my mentor Dr. Ryan Wicker, director of W.M. Keck Center for 3D Innovation, to whom I owe the credits of this small accomplishment of MS degree in Mechanical Engineering. Beyond academics, I have learnt greater life lessons from Dr. Wicker on how to stay positive during failure, and the necessity of clear communication in life, science, and engineering. I would like to thank Jorge Mireles with whom I started learning about the very basics of additive manufacturing. Afterwards, Philip Morton, Dr. David Espalin, and Dr. Cesar Terrazas became great sources of support for me in generating and implementing ideas. With Dr. Espalin I wrote my first conference paper. During the latter days, I was fortunate to meet Dr. Frank Medina who greatly inspired me by his stellar career in the realm of additive manufacturing. I can never thank enough Alfonso Fernandez, a fellow researcher in the lab, without whom turning concepts into prototypes would be impossible for me. Dr. Lawrence Murr greatly helped me shape my first journal article and provided with valuable insight into the work. Dr. Mohammad Hossain and Dr. Jose Gonzalez, both of whom I met as PhD students in the metal team, were great mentors and resource for learning a lot of scientific techniques and culture of the lab. I must mention the contribution of Dr. Yves Hagedorn, the CEO of Aconity3D and the whole Aconity3D team who continuously provided technical support during the challenging times of running AconityONE machine. I am deeply indebted to Dr. Ralph Felice, the CEO of Far Associates for his technical support with the multi wavelength. I am also thankful to Mohammad Naim Jahangir and Kazi Masum Billah who had been a great company in and out of the lab. As a matter of fact, all the student researchers and the staff members of the Keck Center created an unparalleled support

system that raised me to fulfill the requirement of my master's degree. I want to wish well and thank from the bottom of my heart, my immediate successors in the metals team Moinuddin Shuvo and Hunter Taylor.

My utmost gratitude to my parents and elder brother for their continuous encouragement and sacrifice for sending me abroad, literally to the other side of the planet. I want to thank my sister, brother in law and younger brother for their timely support. I must also mention my fiancée who continuously encouraged me and shared words of comfort during this difficult task. Finally, the Bangladeshi community created a home away from home here in El Paso. Without all their support, I would not have made it this far. May Allah allow me the strength to make them all proud and contribute positively towards the society.

Abstract

The focus of this research was twofold, such as development of defect free fabrication parameters for laser powder bed fusion (LPBF) processing of crack prone or difficult to process metallic materials, and study of the temperature dependence of emissivity for some commonly used metal alloy powders in LPBF process. The later objective extends to the implementation of multiwavelength (MW) pyrometer technology for *in situ* true surface temperature measurement in LPBF process. LPBF is an additive manufacturing (AM) process capable of layer-by-layer manufacturing by successive laser melting of each layer according to CAD data. AM manufacturing has the inherent advantages of fabricating optimally designed geometry with least required material and the shortest lead time that would not be possible all at once by more conventional manufacturing techniques such as machining, casting, welding, etc. Tendency to crack during LPBF fabrication of some of the widely used aluminum alloys with large solidification range, such as AA6061, AA7075, etc. created a bottleneck where AM specific advantages of these materials important for aerospace and automotive industry could not be realized. An open architecture LPBF machine AcontyONE (Aconity3D, Aachen, Germany) enabled with powder bed heating up to 1000 °C was used for fabrication of aluminum 6061 alloy (AA6061) test coupons, such as cubes and cylindrical tensile specimens in the XY plane. Variation of processing parameters such as laser power, scanning speed, hatch spacing, layer thickness, and powder bed heating temperature was carried out to find a combination of parameters that allowed crack free fabrication of AA6061. The following parameters such as 450 W laser power, 1400 mm/s scan speed, 100 µm layer thickness, 80 to 100 µm hatch spacing, and 500 °C powder bed heating resulted in crack free specimens as confirmed by visual inspection, optical microscopy, and tensile testing. In scanning electron microscopy (SEM), coarsening of grains and precipitates

was observed due to high temperature preheating, and a preferential growth in [100] direction was also evident from X-ray diffraction (XRD) analysis. The heat treated, and as-fabricated tensile tested specimens showed equivalent ultimate tensile strength and yield strengths when compared to their wrought counterpart; however, loss in elongation at breakpoint was observed in the LPBF fabricated specimens. This part of the research showcased the potential of high temperature powder bed heating for LPBF processing of crack prone metallic materials without the need for additional preparation of the precursor metal powders.

Unlike the commercial LPBF systems currently in use, the open architecture experimental LPBF system used in this study had the capability of achieving controlled high temperature at the powder bed. Whether this high set temperature that proved to deter visible crack formation in AA6061 fabrication, would be carried throughout the height of a build- required true *in situ* surface temperature measurement of the powder bed. Therefore, an important aspect of the current research was to evaluate the thermal environment of the build area in LPBF process. Changing emissivity of metallic materials is a major difficulty in evaluation of true temperature during LPBF processes. The existing *in situ* monitoring systems relied on single or dual wavelength pyrometers, raw sensor data, high-speed visual cameras, and infrared (IR) thermography for monitoring and surface temperature measurements; but, without the emissivity information of the target materials, these systems output a qualitative measurement of temperature instead of an accurate surface temperature. The changing emissivity resulting from the non-grey nature of radiation from metallic materials upsets the assumptions of single and dual-wavelength pyrometry, and thereby, renders the measurements inaccurate. On the other hand, Multiwavelength (MW) pyrometer technology would not require any prior information of the target emissivity for accurate temperature measurement and provided a real-time value of emissivity of the target material by

analyzing the IR spectra it would receive from the target. During the LPBF process, on a given layer the precursor powder material in solid state would turn into molten metal tracks after interaction with laser at selected spots, and finally, consolidate to bulk solid state when the rest of the powder on the bed would not go through phase change. At least three different metal states with potentially different emissivity were identified, such as metal powder in solid state, molten metal tracks, and solidified metal tracks. To measure this emissivity for different materials and study their variation with temperature, a Whipmix Pro 200 (Whipmix Inc., Louisville, KY) furnace was modified for optical access to a SpectroPyrometer (FAR Associates, OH, USA) MW pyrometer system. These emissivity measurements could serve as input for IR thermography for extending accurate surface temperature measurements capability from a pointwise measurement using pyrometer to the accurate temperature mapping of an area using the IR thermography. Also, for demonstrating *in situ* temperature measurement in LPBF system using MW pyrometry, processing laser window and the viewing window of the AconityONE system situated on the top and the front side of the machine, respectively were redesigned and fabricated with the facility of quartz and ZnSe viewing ports through which a SpectroPyrometer (FAR Associates, Ohio, USA) MW pyrometer system and a FLIR SC645 IR camera (FLIR Systems, NM, USA) could operate.

Metal powders such as AA6061, AlSi10Mg, Ti-6Al-4V with two different particle size distributions, and Cu were heated in quartz crucibles inside the modified furnace at different temperatures. Argon gas at a pressure of 3 psi and 20 cubic-feet-per-hour were introduced to the heating chamber of the furnace. Despite the use of argon to create inert environment, oxidation of the metallic materials occurred and essentially the measurements made using this setup reflected the properties of the oxidized top layer instead of the intended powder material in its pristine form. However, the effect of powder particle size distribution on emissivity could still be observed as

larger particle size resulted in higher emissivity. Also, two different trends of emissivity changes were identified for the heating and the cooling portion of the furnace operation. Inserting the setup inside a glovebox, use of designed inert gas flow path inside the furnace, and use of better sealing materials for the instrument pass-throughs were recommended for improvement of the experimental setup for future research. On the other occasion of *in situ* measurements, the data obtained by using the MW pyrometer through the modified AconityONE window was affected by the 1070 nm processing laser since the measuring range of the MW pyrometer was 850 nm to 1650 nm. This problem could be overcome by filtering out the processing laser from the spectra that reaches the MW pyrometer system. Overall, the application of MW pyrometer technology in combination with IR thermography could be a viable option for *in situ* temperature mapping of the powder bed in LPBF systems.

Table of Contents

Acknowledgements	v
Abstract	vii
Table of Contents	xi
List of Tables	xiv
List of Figures	xv
Chapter 1: Introduction	1
1.1 Research Motivation	1
1.2 Thesis Objective.....	3
1.3 Project Overview	4
1.4 Summary of Results	6
1.5 Thesis Outline	9
Chapter 2: Literature Review	11
2.1 Additive Manufacturing (AM) and Laser Powder Bed Fusion (LPBF)	11
2.2 Fabrication of Aluminum 6061 Alloy.....	12
2.3 <i>In situ</i> Monitoring in LPBF: A Necessity	17
2.4 Rationale of the current research considering the literature review	37
Chapter 3: Experimental Setup and Methodology.....	40
3.1 AconityONE Experimental LPBF System.....	40
3.2 Description of Pyrometer Experiments.....	45
3.2.1 Materials	45
3.2.2 Whipmix Pro 200 furnace	46
3.2.3 Modified Whipmix Pro 200 furnace	47
3.3 Measuring Devices.....	53
3.3.1 Multi-wavelength or Spectro-Pyrometer	53
3.3.2 Thermocouple Data Acquisition System	55
3.4 In Situ Off Line Monitoring Windows	56
3.5 Pyrometer Data Analysis	59

Chapter 4: Pyrometry	62
4.1 Necessity of Non-contact Temperature Measurement in Additive Manufacturing	62
4.2 Introduction to Pyrometry	63
4.3 Manually Operated Pyrometers	66
4.3.1 Disappearing Filament Pyrometer	66
4.3.2 Two-color Pyrometers	69
4.4 Automatic Pyrometers	71
4.4.1 Single Wavelength Pyrometers	71
4.4.2 Dual Wavelength Pyrometers	72
4.4.3. Multi Wavelength Pyrometers	74
4.4.4 Time Resolution of Different Ratio Pyrometers	75
4.5 Automatic Pyrometers Components	76
4.5.1 Transmission Optics	76
4.5.2 Infrared Radiation (IR) Detectors	79
4.5.2 (i) Thermal Detectors	80
4.5.2 (ii) Photon Sensitive Quantum Detectors/Photodetectors/Photodiodes	82
4.5.3 Detectivity of Photodetectors	85
4.6 Wavelength Splitting/ Multiplexing	87
4.7 Challenges in Pyrometric Measurements of Metals	92
4.7.1 Challenge with Changing Emissivity	92
4.7.2 Dependence of Emissivity on Angle of View	92
4.7.3 Error Associated with Longer Wavelength	93
4.7.4 Selecting the Right Fiber Optic	94
Chapter 5: Published Work – Crack-Free Aluminum 6061 Fabrication Demonstration	96
5.1 Title, Authors, and Affiliations	96
5.2 Abstract	96
5.3 Methodology	97
5.3.1 Materials	97
5.3.2 LPBF Fabrication Process	100
5.3.3 Material Characterization	104
5.3.4 Mechanical Properties	106
5.3.4 (i) Microhardness	106

5.3.4 (ii) Tensile Properties.....	107
5.4 Results and Discussion	108
5.4.1 Density	108
5.4.2 Mechanical Properties.....	109
5.4.2 (i) Microhardness	109
5.4.2 (ii) Tensile Properties.....	110
5.4.3 Microstructure.....	111
5.4.3 (i) Optical Microscopy	111
5.4.3 (ii) XRD	117
5.5 Conclusion	119
Chapter 6: Results	121
6.1 Materials Under Study	122
6.2 Comparison of Measured Temperatures.....	127
6.3 Demonstration of Temperature Calculation Using Intensity Data	129
6.3.1 Understanding the .dat File	130
6.3.2 Calculation of Temperature	131
6.4 Emissivity Measurements of Different Powder Materials and Comparison	134
6.5 Results from in situ monitoring of AconityONE.....	139
Chapter 7: Conclusions and Recommendations	141
7.1 Conclusions.....	141
7.2 Recommendations for Future Work.....	142
7.2.1 Use of High Temperature Powder Bed Heating	142
7.2.2 Oxidation Problem.....	143
7.2.3 Establishing Temperature Mapping of Build Area in LPBF Process	145
7.2.4 Removal of Laser Line from MW Pyrometer.....	146
References	147
Appendix A Data on AA6061 Parameter Development.....	164
Appendix B Pyrometer Measurements and Calculations	176
Appendix C Permission to Reuse Published Article in Chapter 5	180

List of Tables

Table 3.1: Common file preparation parameters [55].....	41
Table 3.2 Supplier provided specification of the metal powders under study.....	46
Table 4.1 Time resolution of different ratio pyrometers.....	75
Table 4.2 Comparison of IR detector types (Rogalski <i>et al</i> [85].).....	79
Table 5.1 Range of LPBF parameters explored to find the crack-free parameter combination .	101
Table 5. 2 Microhardness values of LPBF fabricated AA6061 components under different conditions.....	109
Table 5.3 Comparison of mechanical properties of LPBF fabricated AA6061 and wrought annealed AA6061 for both annealed and T6 heat treated conditions	110
Table 6.1 Material and operating condition. A ramp of 10 °C/min was used in all cases to heat up the material to the maximum temperature	127
Table 6.2 Raw intensity data file i.e. .dat file obtained from the MW pyrometer after annotations	131
Table 6.3 Schematic matrix of calculated ratio temperatures using equation 6.1	132
Table 6.4 Calculated ratio temperatures using equation 6.1 from data file ‘Temp6188.dat’	132

List of Figures

Figure 2.1 Flowchart showing typical workflow during LPBF AM fabrication	12
Figure 2.2 Marangoni number greater than 10^5 result is turbulent and therefore more unstable melt pool as shown by Mukharjee <i>et al.</i> [38]	18
Figure 2.3 In line monitoring set up consisting of high-speed camera and photodiode sensor shown by Berumen <i>et al.</i> [41]	20
Figure 2.4 (a) gray scale image of the data obtained from the in-line high speed camera showing the dimensions of the melt pool in x and y direction (b) photodiode detected intensity of the light emitted from melt pool; increased intensity around layer 2000, 2600, and 3000 correspond to process error where larger amount of powder was deposited due to un-synced movement of the build platform [41].....	21
Figure 2.5 (a) block diagram of the different optical component required for the in-line melt-pool imaging setup invented by Lott <i>et al.</i> [42] (b) actual setup with an image of the melt pool and surrounding area with a 5 mm x 5 mm field of view.....	22
Figure 2.6 (a) Illustration of mapping algorithm used by Clijsters <i>et al.</i> [43] On the left is are the intensity values obtained by the photodiodes and corresponding grey scale values. Grey scale values were plotted in a rectangular grid as shown on the right side of image. Mapping of only a single vector is shown; when all the vectors in a layer is mapped, a grey value representation of the entire layer could be obtained. If multiple points corresponded to a single grid, the average of those intensities were considered for that grid (b) Porosity corresponding to high laser power and corresponding larger melt pool as detected by the proposed monitoring system.....	25
Figure 2.7 Image obtained from the visual observation system developed by Debenskaia <i>et al.</i> [44] where the effect of single and double scanning of the same layer is visible by difference in visual	

contrast. The layer that had been scanned once, appeared darker in the visual observation system 26

Figure 2.8 Signals from the pyrometer in arbitrary units showing the effect of change in hatch spacing on temperature as observed by Debenskaia *et al.* [44] Curves 1 through 6 represents builds with different hatch spacings when all the other scanning parameters were kept unchanged. Curve 1 represents the build with 1 mm hatch spacing and 6 represents a build with 70 μm layer hatch spacing. Layer temperature with smaller hatch spacing was considerably higher because of the higher energy input within the same area in the latter case 27

Figure 2.9 (a) the effect of laser power on the maximum temperature of laser and powder interaction zone as reported by Furumoto *et al.* [45]. However, caution should be maintained before considering the temperatures as true surface temperature since the effect of emissivity could was not considered. Also, the measured area was greater than the process interaction zone Temperature of the substrate plate was also captured (b) shows the scheme of temperature calculation from the signals of the photodiode detectors. Rise in signal levels in the detectors reflect the moment of laser irradiation and corresponding increase in temperature..... 29

Figure 2.10 Set up devised by Furumoto *et al.*[48] for investigating the consolidation behavior of metal powder upon laser irradiation 30

Figure 2.11 The change of temperature of the melt area with change in energy density during the melting of stainless steel powder by laser irradiation as reported by Furumoto *et al.*[48]. Caution should be maintained before considering the reported temperature as the true surface temperature since this study did not consider the effect of emissivity change as a function of temperature ... 31

Figure 2.13 Zavalov *et al.* [49] reported brightness temperature and corresponding signal intensity are shown for channels 1, 3, and 5 i.e. 0, 0.6, and 1.2 mm away from the laser and powder bed

interaction zone. Curves in black denote brightness temperatures, the colored graphs denote intensity values at the channel 1 (red), channel 2 (green), and channel 3 (blue).....	33
Figure 2.14 (a) Plots of normalized histogram of line to continuum ratio occurring at different disks i.e. different processing conditions (b) percent void, a measure of porosity at different processing conditions (c) Experimental set up used by Nassar <i>et al.</i> [53]	36
Figure 3.1 (a) and (b) depict different build file preparation parameters [55].....	42
Figure 3.2 A uniform power density could be ensured by introducing a moving lens to consistently adjust the beam focus and hence spot diameter. (a) Moving lens is kept static to depict that the focal plane could curve out of build surface (b) Movement of the lens ensures dynamic focus change and therefore, uniform power distribution throughout the build area. [56].....	43
Figure 3.3 Image showing measurements made on a single layer scanning of four 10 x 10 x 10 mm cubes on the build platform using one of the 100 kHz pyrometers. AlSi10Mg powder was used for the fabrication. The color-coded bar shows the mV readings from the thermocouple detector that was used to create the pseudo-temperature plots.	44
Figure 3.4 Single and dual stage operation of the Whipmix Pro 200 furnace	47
Figure 3.5 Cross section of the modified Whipmix Pro 200 furnace	48
Figure 3.6 Modified Whipmix Pro 200 furnace with pyrometer assembly	49
Figure 3.7 A top view of part of the modifications made to the Whipmix Pro 200 furnace. The modified top window of the furnace is shown in the picture and a closer view is presented in the inset	50
Figure 3.8 Picture of the interior of the modified furnace. Heating coil, the quartz viewing port for providing optical access to the MW pyrometer and the thermocouples are visible	51

Figure 3.9 To maintain inert gas atmosphere inside the furnace argon was continuously introduced inside the furnace chamber. Before purging with argon, the chamber would be vacuumed at 200 °C.....	52
Figure 3.10 Different components of the FMPI SpectroPyrometer (FAR Associate, OH, USA) MW pyrometer system.....	54
Figure 3.11 Different components of the thermocouple data acquisition system used in the current study.....	55
Figure 3.12 The top window of AconityONE after modification to incorporate MW pyrometer and an IR camera for in situ monitoring of the build. The original laser window of the AconityONE machine was replaced with this modified window	56
Figure 3.13 CAD model of the modified top window with the laser enclosure bottom part of which was made transparent (only in CAD model) for better visual. The transparent laser enclosure gives visual to the reduce size laser processing window.....	57
Figure 3.10 <i>In situ</i> monitoring setup including MW pyrometer mounted to the side window of AconityONE machine. The spectro-pyrometer box contains the means for dividing the incoming radiation in with a spectral resolution of close to 1 nm	58
Figure 3.15 An inclusive CAD of <i>in situ</i> monitoring set up where both the front and top monitoring windows are shown. The components were identified in the previous Figures	59
Figure 4.1 Electromagnetic spectrum showing the visible and IR radiation ranges that are usually utilized in pyrometry [61]	64
Figure 4.2 Classification of pyrometers based on spectral response and method of operation [62]	65
Figure 4.3 Main components of an automatic pyrometer	71

Figure 4.4 Schematic of a two-wavelength pyrometer circuit [68]	72
Figure 4.5 (a) Blackbody radiation characteristics based on temperature. (b) Transmittance of typical IR window [62]	77
Figure 4.6 l/d designation of lenses used in pyrometry	78
Figure 4.7 Basic construction of a micro-bolometer (Wikipedia)	81
Figure 4.8 (a) Pulse type detection system schematic (b) a typical signal as detected in a pulse-based system [91].....	83
Figure 4.9 Spectral response of photovoltaic (PV) detectors made of MCT structures with and without cooling [96].....	86
Figure 4.10 Comparison of directivity between HgCdTe or MCT and GaAs/AlGaAs based QWIPs photodetectors [998]	87
Figure 4.11 (a) bandpass filters (b) notch filters (c) short-pass filters (d) long-pass filters [100]	88
Figure 4.12 Schematic representation of a dichroic mirror placed at 45° with the incoming radiation [100].....	89
Figure 4.13 Schematic of an arrayed waveguide grating in demultiplexing (splitting a spectral signal into discrete bands) [103]	91
Figure 4.14 Long wavelength could result in peak broadening and subsequent inaccurate output of temperature [91].....	94
Figure 4.15 Basic construction of a fiber optic cable with cladding to provide total internal reflection of the light signal that falls within angle of acceptance [106].....	95
Figure 5.1 (a) SEM images of AA6061 gas atomized powder. Powder particles were spherical, and semi-spherical with satellites. Some irregular shaped powder was also observed	99
Figure 5.1 (b) Histogram of AA6061 powder size distribution.....	100

Figure 5. 2 (a) Scan-head of the AconityONE system consisting of the Galvo mirrors and f- θ lens. The optical fiber receives the 1030 nm wavelength, near infrared laser from the laser module where Nd:YAG crystals were used for solid state amplification. The scan-head is capable of rastering over an area of 400 mm in diameter. However, during heated bed configuration a reduced scan area with 200 mm in diameter is covered.	101
Figure 5.2 (b) A schematic representation of the AconityONE LPBF system used for the study. (i) Solid state Nd:YAG laser of 1030nm wavelength and 1kW capacity and an induction heater (not shown in figure) underneath the build platform that can raise the powder bed temperature to 1000°C are featured. (ii) The re-coater brush is made of carbon fiber to impart flexibility and high heat resistance.	103
Figure 5.3 Relative density of AA6061 cube coupons fabricated using different laser power and scanning speed with and without heating of the powder bed	108
Figure 5.4 Microstructure of AA6061 specimens fabricated on unheated powder bed. Figure 5.4 (a) and (b) illustrate the XY plane (perpendicular to build direction). Figure 5.4 (c) and (d) show the ZX plane (build direction). Cracks, porosity, melt-pool, and melt-track banding are evident in the microstructure	112
Figure 5.5 Microstructure of AA6061 specimens fabricated on powder bed heated to 500 °C. Figure 5.5 (a) and (b) illustrate the XY plane (perpendicular to build direction). Figure 5.5 (c) and (d) show the ZX plane (build direction). Cracks, porosity, melt pool, and melt-track banding removed from the microstructure, and a columnar grain growth is observed in the build direction	113

Figure 5.6 SEM (a) and STEM (b) images of primarily Al-Si-O noncoherent precipitates shown in Figure 5.5. The same area is imaged in (a) and (b) and the magnification for both is given in (a).	115
Figure 5.7 Representative stress-strain diagram of LPBF fabricated AA6061 specimens as fabricated and T6 heat treated. Figure 5.7(b) Solid cylinders built in X direction and still on build plate; tensile specimens were machined out of these cylinders. Figure 5.7(c) LPBF fabricated AA6061 tensile testing specimen after fractured.....	116
Figure 5.8 XRD spectra for AA6061 fabricated with and without heating of the powder bed (a) and (b) show XRD spectra in unheated XY and ZX reference planes. (c) and (d) show XRD spectra in heated XY and ZX reference plane.....	118
Figure 6.1 (a) Particle size distribution of Cu powder (b) SEM image of the Cu powder used for the current study showing spherical powder with a lot of satellites and irregular shape powder.....	123
Figure 6.2 (a) Particle size distribution of Ti-6Al-4V powder of EBM grade (b) SEM image of the Ti-6Al-4V powder of EBM grade used for the current study showing spherical powder.....	125
Figure 6.3 (a) Particle size distribution of Ti-6Al-4V powder of LPBF grade (b) SEM image of the Ti-6Al-4V powder of LPBF grade used for the current study showing mostly spherical powder with occasional satellite	126
Figure 6.4 Comparison of temperature measured by the pyrometer and the thermocouple when EBM grade Ti-6Al-4V was heated up to 950 °C Figure 6.4 (a) and (b) demonstrates the comparison during heating up and cooling down, respectively	128
Figure 6.5 Comparison of measured temperature, that was obtained as an output from the MW pyrometer, with the temperature calculated by algorithm applied by the author	129

Figure 6.6 Change of emissivity with temperature during the heating of Ti-6Al-4V. Two different particle sizes, i.e. EPBF and LPBF grade powders were tested and compared	135
Figure 6.7 Change of emissivity with temperature during the cooling of Ti-6Al-4V. Two different particle sizes, i.e. EBM and LPBF grade Ti-6Al-4V powders and EBM powder with a different material i.e. copper powder were tested and compared	136
Figure 6.8 Change of emissivity with temperature during the heating of Ti-6Al-4V. Two different particle sizes, i.e. EBM and LPBF grade Ti-6Al-4V powders and a EBM powder with a different material i.e. copper powder were tested and compared	137
Figure 6.9 Comparison of emissivity of AA6061 and AlSi10Mg when cooled down from 650 °C to 350 °C	138
Figure 6.10 The two most typical data files obtained during the <i>in situ</i> MW pyrometer measurement in AconityONE machine. The corresponding temperature outputs were given underneath the intensity graphs where high value of tolerance for the measurement affected with processing laser indicates lack of accuracy. The other measurement however captured the accurate surface temperature measured on a powder layer atop the pre-heated build plate	139
Figure 7.1 Laser-powder interaction occurs in zone 1. Zone 1, 2,3, and 4 could be different in phase and temperature and therefore differ in emissivity. To truly map the build area using an IR camera would require emissivity feedback from the MW pyrometer array	145

Chapter 1: Introduction

1.1 Research Motivation

Additive manufacturing (AM) is a freeform fabrication technology where end user parts are manufactured directly from the 3D models created using computer aided design (CAD) software. The requirement for part specific tooling and multiple manufacturing steps involved in the conventional manufacturing processes that account for a long lead time and added costs, could be avoided in AM technologies. For example, the production of a gas turbine blade require four main process steps such as casting, forging, different types of machining, and coating along an array of sub-processing steps [1]. On the other hand, a single step process of manufacturing similar turbine blade directly from CAD was experimentally shown by Fabrizia *et al.* [2]. This is only a single example of cost effectiveness realized by AM processes. Among the different AM technologies, laser powder bed fusion (LPBF) is used for manufacturing of metal parts by selective melting of thin layer of metal powders spread on a solid surface for the first layer and on the previous consolidated surfaces for the subsequent layers.

One of the restricting factors that inhibits the realization of metal AM advantages on an industrial scale is the lack of developed processing parameters for the range of metal alloys used across different industries, such as aerospace, automotive, biomedical, etc. Despite being one of the most widely used aluminum alloys for the automotive and aerospace industries, aluminum 6061 alloy (AA6061) processing parameters have not been developed for fabrication using LPBF AM process due to crack formation [3] [4] [5]. Such a shortcoming deterred the application of LPBF in fabrication of AA6061 and resulting advantages of the process. Also, there are alloys such as AA7075 and AA2024 with cooling characteristics like AA6061 that could not be processed

using LPBF due to cracking. Development of processing conditions and parameters for such alloys could be of benefit to the industry. It could be hypothesized that a high thermal gradient resulting from the nature of LPBF process and a large solidification range typical of AA6061 might result in high strain in the melt pool. Such strain, when reached a critical stage, could result in crack formation following the route proposed by Pellini [6] for welding cracks. Use of preheating has been demonstrated for crack free fabrication of M2 high speed steel (HSS) tools [7]. Therefore, in this research, application of powder bed heating was used to explore the crack free fabrication of AA6061.

In the course of the research on AA6061 fabrication, the necessity of understanding and quantifying how the powder bed preheating affected the thermal environment that resulted in observable crack-free LPBF fabrication of AA6061. This requirement called for accurate *in situ* measurement of temperature. Accurate measurement of temperature in LPBF could also be vital for process standardization and qualification, quality control of the products, establishing feedback monitoring control systems for automatic correction of defects, etc. It was found from the literature review that the state-of-the-art in measurement of *in situ* true surface temperature lacked in methods and instrumentation. Most of the current approaches in surface temperature measurement relied on merely providing the sensor data that could be best labelled as pseudo temperature measurement. Everchanging emissivity of metallic materials rendered accurate temperature measurement a difficult task. In addition, at any given time in a LPBF process when the processing laser operates, there coexists at least three different material states; namely, metal powder in solid state, molten metal tracks, and solidified metal tracks, each with a different emissivity. Existing *in situ* monitoring techniques that deals with temperature measurement could be categorized as (i) in-line with laser, (ii) a fixed-point temperature measurement on the powder

bed and (iii) infrared (IR) thermography of the total build area, a more detailed discussion of which could be found in Chapter 2. None of the approaches mentioned above considered the variation of emissivity and therefore, could not provide accurate temperature. One of the overlooked temperature measurement techniques in these studies was the multiwavelength (MW) pyrometry. MW pyrometers would not require a target emissivity input; in fact, the MW pyrometers measured absolute temperature by analyzing the spectral data obtained from the target and gave output a target emissivity value in the process. Therefore, in the current research, MW pyrometer was considered for *in situ* temperature measurement of LPBF process. However, considering the distinct material states present during the LPBF processes, two different setups were used for the study of thermal environment; one, a modified furnace inside which precursor powder were studied at different elevated temperatures, and the other, modified machine windows through which surface temperature measurements at a single point was enabled. For the latter case, the measured single point would undergo all the three material states discussed above and the corresponding temperature values would be captured.

Considering the industrial pull for parameter development of high strength aluminum alloys and control of build environment for quality assurance, high temperature powder bed heating during LPBF fabrication and accurate *in situ* temperature measurements could be deemed valuable. Thus, the ideas discussed, methods proposed, and preliminary results and setups presented during this thesis, drew motivation from the real life LPBF AM problems.

1.2 Thesis Objective

The overarching objective of this research project was to more completely understand the effect of powder bed heating during the fabrication of crack prone aluminum alloys using LPBF AM technology and demonstrate crack free fabrication of AA6061 using the same technology. In

the process of this investigation, the question of measuring the accurate surface temperature of the powder bed and the solid part during the fabrication process became prominent and transpired to an independent research objective. The main objectives of the current thesis could be captured in the following statements,

- 1) Development of processing parameters for the crack free LPBF fabrication of AA6061
- 2) Study the effect of powder bed heating on the fabrication of AA6061
- 3) Design and fabrication of *in situ* monitoring setup for AconityONE
- 4) Determination of temperature dependence of emissivity of metal powders with different compositions, and particle sizes
- 5) Develop and demonstrate an algorithm to calculate temperature from spectral intensities

This project is still a work in progress with the goal of developing fully equipped LPBF system with detailed monitoring and control of the build. Such equipment would be necessary for furthering the capability of metal additive manufacturing of difficult to process metal alloys. Part qualification and standardization of the production line could be realized in a more scientific manner with the application of process monitoring and control.

1.3 Project Overview

In view of the thesis objectives, this project involved the development of crack free LPBF manufacturing parameters of AA6061, and design and fabrication of *in situ* monitoring set up for determining accurate surface temperature of the part under fabrication. Open architecture experimental LPBF system AconityOne (Aconity3D, Aachen, Germany) was employed for the experimentation due to its heating capability of the powder bed up to a 1000 °C using an induction

heater, and laser power up to 1 kW. Given the high laser reflectivity and high thermal conductivity of AA6061, the use of powder bed heating and high laser power became worthwhile.

Different LPBF parameters, such as laser power, scanning speed, hatch spacing, layer thickness, powder bed temperature, etc. were varied in a series of experiments to identify the set of parameters that would result in observable crack-free fabrication of AA6061. Optical microscopy (OM), scanning electron microscopy (SEM), and X-ray diffraction (XRD) techniques were applied to investigate the presence of cracks or absence thereof. To determine the applicability of the developed parameters in fabrication of end user parts, tensile testing specimens were built, heat treated and tested.

Another major focus of the project was to develop, test, and recommend *in situ* monitoring systems primarily for accurate surface temperature measurements. To achieve this, the top and side windows of the AconityONE machine were modified to incorporate viewing ports made of quartz and zinc selenide (ZnSe). The quartz window provided optical access for SpectroPyrometer, and the ZnSe worked as a viewing port for the IR thermography. To ensure laser safety through the modified windows, custom laser enclosures were 3D printed using nylon. These monitoring windows were *in situ* but off-line i.e. only a single perspective measurement would be possible since the pyrometer and IR camera would remain fixed on a single axis.

Another *in situ* monitoring set up consisting of two 100 kHz single wavelength pyrometer and a 5 kHz CMOS camera was installed in the AconityONE system. These pyrometers and high-speed camera were in-line with laser that would capture the route of laser pointwise and provided highly dynamic images of the melt track. Due to the lack in knowledge of emissivity, the highspeed single wavelength pyrometers would only provide a qualitative measurement of temperature by means of the signal value of the detectors in mV unit.

Multi wavelength (MW) pyrometry technique require no prior information of the target emissivity to yield accurate surface temperature, and in fact, provides emissivity values of the target object as an output. In the current project, three different approaches were adopted during the experimentation with a SpectroPyrometer (FAR Associates, OH, USA) MW pyrometer system. Such as, the MW pyrometer was used for- (i) off-line *in situ* measurements of the builds, (ii) *in situ* build temperature measurement in-line with laser, however without much success, and (iii) emissivity measurement of different meatal powders inside a modified furnace Whipmix Pro 200 (Whipmix Inc., Louisville, KY).

With a view to profiling the emissivity of different metal powders, such as Cu, AlSi10Mg, Ti6Al4V, etc. through a range of temperatures, these powders were heated inside a modified Whipmix Pro 200 (Whipmix Inc., Louisville, KY) furnace. The furnace top was modified to incorporate a quartz window for MW IR thermometry, and a compression sealed port for including a thermocouple. The furnace had a capacity of heating up to 1200 °C. The tests were performed under argon atmosphere.

1.4 Summary of Results

Fabrication of AA6061 alloy without any observable crack formation was demonstrated using powder bed heating in an open architecture LPBF system AconityONE. Parameters such as laser power, scanning speed, hatch spacing, and layer thickness were changed to achieve observable crack free fabrication. As shown in the microstructural images Figure 5.4 in Chapter 5, mud-like cracking was observed in both- the build direction and perpendicular to build direction for the cube specimens produced without powder bed heating. On the other hand, as depicted in Figure 5.5 in the same chapter, the microstructural images corresponding to the cube specimens produced with powder bed heating showed no visible cracks. Amount of porosity also decreased

markedly, and more notably, the melt-pool banding which is a typical microstructural feature of LPBF processes was eliminated with a supposed positive impact on mechanical properties. Semi-lunar and longitudinally overlaid melt-pool bandings usually delineated the heat affected zones resulting from the melt tracks created by the travelling laser beam. Absence of such as melt-pool banding when high temperature powder bed heating was used, indicated reduction of heat affected zone from the fabricated parts as well as removing cracks.

A highest relative density of 98.7% was measured for the cubic coupons produced with powder bed heating at 500 °C. The relative density of the cube coupons fabricated without powder bed heating was generally at the lower end of 90%. The density comparison clearly indicated an advantage of using high temperature powder bed heating for AA6061 LPBF fabrication.

Mechanical testing was performed on cylindrical tensile specimens of AA6061 fabricated using laser powder bed fusion (LPBF) process. These specimens were fabricated using the highest density parameters obtained from the parameter development study with the cube coupons. All the tested tensile specimens were produced on heated powder bed since the tensile specimens produced without powder bed heating lacked so much in properties that they could not be cut-off from the build plate without being broken. Such fragility of larger AA6061 components compared to cube specimens, indicated the value of using of powder bed heating for LPBF processing of alloys such as AA6061. Out of the four specimens produced with powder bed heating, two were heat treated and two were tested in as-fabricated condition. The two heat treated specimens showed ultimate tensile strength (UTS) of 308 and 318 MPa that were comparable to the T6 heat treated wrought AA6061 with UTS of 310 MPa. The as-fabricated specimens showed UTS of 133 and 141 MPa that were comparable to annealed wrought AA6061 with UTS of 124 MPa. A reduced elongation at breakpoint was observed for the LPBF fabricated specimens indicating loss

of ductility during AM fabrication. Coarsening of grains and precipitates were observed due to high temperature powder bed heating.

The setups with the modified furnace for studying powder emissivity at different elevated temperature and the modified process monitoring windows on AconityONE resulted in some noteworthy observations. In the modified Whipmix Pro 200 (Whipmix Inc., Louisville, KY) furnace, several commonly used metal alloy powders in powder bed fusion AM technology, such as Ti-6Al-4V powder with two different particle size distributions, AlSi10Mg, AA6061, and unalloyed copper (Cu) powder were heated up to 950 °C contained in quartz crucible and argon environment. The MW pyrometer measured the temperature and corresponding emissivity. The highest temperature achieved was limited by the furnace's capacity. From the visual inspection of the powders retrieved from the furnace, oxidation of the Ti-6Al-4V and Cu powders were evident from the change in colors. Since the Al based alloys did not have any transition metal in substantial quantity, they would not undergo any notable discoloration; however, the trend of emissivity value which reached a plateau after a certain temperature for all the materials indicated possible oxidation. Regardless of oxidation, the effect of powder particle size distribution on emissivity was determined; it was shown from experimental data that the larger metal particles demonstrated more emissivity. Also, powder materials with more surface irregularity showed higher emissivity. Also, the observations showed the importance of pointed research to find out correlation between the allowable oxygen level in the process chamber for different alloys in high temperature LPBF process since there existed a higher chance of oxidation at elevated temperature which might jeopardize the build quality and reuse of the material.

The setup for *in situ* monitoring in AconityONE involved modification of the machine's top window through which the processing laser operated, and the frontside window originally

meant for general viewing. Both windows were redesigned to hold quartz and ZnSe ports. Brackets and slotted arms ensured the installation of the MW pyrometer lens with the facility of adjustments for the location and the change of focus of the measuring spot. The IR thermography could be introduced through these modified monitoring windows but remained beyond the scope of current work. The *in situ* measurements showed that the set powder bed temperature was carried to the top surface of the build. However, when the processing laser was operated, the pyrometer measurements were adversely affected due to the detection of the 1070 nm of the processing laser since that wavelength was within the measuring wavelength range of the MW pyrometer. The MW pyrometer gathered spectral data within the wavelength range of 850 nm to 1650 nm. To avoid the detection of the processing laser, a filter could be used for blocking away any wavelength within 30 nm of the 1070 nm from reaching the MW pyrometer lens.

1.5 Thesis Outline

The following chapters contain literature reviews, description of experimentations, methodology for analysis, results, and recommendations for future research that the author thought could lead to useful findings for the additive manufacturing community. Chapter 2 contains a brief overview of AM technology and LPBF process followed by a review of LPBF fabrication of AA6061. Review of *in situ* monitoring of LPBF process consisting of pyrometers, infrared (IR) thermography, high speed videography, photography, and X-rays is also in Chapter 2. In Chapter 3, descriptions of the experimental setup including a discussion on AconityONE LPBF system, modification of a dental furnace, and modified windows for *in situ* monitoring in AconityONE is discussed. Chapter 4 includes discussion on pyrometric measurement principles, different hardware requirement for pyrometer construction and challenges associated with temperature

measurements using pyrometers, particularly that of metallic materials. Chapter 5 contains the published work with LPBF fabrication of AA6061. Different sections of the published articles, such as abstract, methodology, results, etc. are included as sub section of Chapter 5. Literature review on LPBF fabrication of AA6061 was included in Chapter 2 after being adopted from the introduction section of the published journal article. The result section of the current document included as Chapter 6 contains result from mostly the temperature and emissivity study of the metallic powder materials and some *in situ* monitoring data from AconityONE. Finally, Chapter 7 contains the conclusions drawn from the study and recommendation for future research to improve the method of in situ temperature monitoring in LPBF process. A schematic of a setup that could achieve the accurate temperature mapping of the total build area in combination with multiple MW pyrometers and high-speed IR thermography was proposed. *In situ* accurate temperature measurement would assist in achieving improved build quality, automatic control of the LPBF process and standardization of the technology for greater acceptance in a more diverse and mission critical manufacturing industries. The appendix section of the current document provides additional data from different experiments and MATLAB[®] scripts used for the analysis of the data.

Chapter 2: Literature Review

2.1 Additive Manufacturing (AM) and Laser Powder Bed Fusion (LPBF)

Additive manufacturing (AM) is defined as a layer-upon-layer material joining process as opposed to subtractive material manufacturing methodologies. Other names for the technology include: additive fabrication, additive processes, additive techniques, additive layer manufacturing, layer manufacturing, and freeform fabrication according to ASTM standards [8]. Manufacturing industry has historically relied on different subtractive techniques and complementing shaping and forming techniques for part productions. Due to high design flexibility, lower material usage, shorter lead times, and other industry specific advantages, there has been a rapid expansion of AM, and so far seven different process categories of AM technologies have been identified by ISO/ASTM 52900:2015-standards [9]. Originally developed around polymeric materials, waxes, and paper laminates- AM's latest focusing area has been metals and ceramics [10].

In AM, a 3D model, designed using any CAD software, is sliced into required thickness using data processing software specific to the AM technology to be used for fabrication. In material extrusion process, which is a widely used AM technology for polymeric materials, stock materials in the form of wires or pellets are fed through an extruder hot enough to melt and maintain a continuous flow of material at the tip. The extruder head moves on the build plane according to the contour and infill of that slice and is raised by an amount equal to the layer thickness set during the data preparation. Vat polymerization is another AM technology meant for photo sensitive resins. This category of AM technology works according to the principle of selective curing of the resin vat by means of a laser source of specified wavelength. The general terminology for AM techniques that use powder materials spread on a build plate where high

energy laser or electron beam interacts with it is known as powder bed fusion (PBF) technologies. For PBF processes concerning polymeric materials, only sintering is achieved instead of full melting of the powder bed. ‘Sintering’ could be understood as the heating of the material without liquefaction whereas in ‘melting’ processes liquefaction occurs.

The two AM technologies that work for metallic materials are laser powder bed fusion (LPBF) and electron powder bed fusion (EPBF). A typical workflow of the LPBF AM process is shown in Figure 2.1.

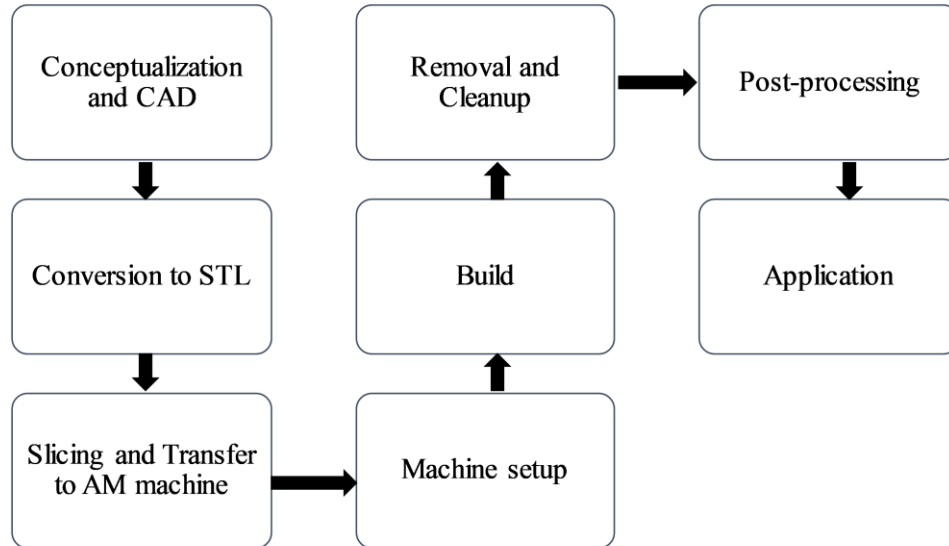


Figure 2.1 Flowchart showing typical workflow during LPBF AM fabrication

2.2 Fabrication of Aluminum 6061 Alloy

The following section was adopted from the author's published journal article entitled: Processing and characterization of crack-free aluminum 6061 using high-temperature heating in laser powder bed fusion additive manufacturing [11]. Permission of reuse of the article was acquired from Elsevier and relevant correspondence with the publisher was given in Appendix C.

Aluminum alloy (AA) 6061 is a heat-treatable alloy with silicon (Si) and magnesium (Mg) as its major alloying elements. AA6061 is widely used in the aerospace and automobile industries due to its high strength to weight ratio, corrosion resistance, and ease of conventional fabrication [12]. For instance, AA6061 can be extruded, rolled, forged, and cast. Different joining methods, such as riveting, welding, brazing, soldering, and adhesive bonding also work for AA6061 [12]. Alternatively, LPBF AM fabrication of AA6061 would add to the advantages of using the material by introducing topology optimization, mesh structures, thin features, internal features, and more that might be difficult to achieve using conventional manufacturing techniques [13,14]. As a result, AA6061 has been receiving attention from the AM community.

AA6061 has been a difficult alloy to process using LPBF because of high crack sensitivity of the material during solidification [5,15]. Solidification cracking of Al-Si-Mg alloy systems is widely discussed in the welding literature [16–18], from which valuable insight into the factors affecting crack formation in LPBF can be obtained. For instance, after reviewing solidification cracking in welds, Cross [19] identified that large difference between the solidus and liquidus temperatures (solidification range) of an alloy, the retardation of liquid transport phenomena to the shrinkage area due to complex dendritic network in the mushy zone, and the lack of eutectic points for a given alloy are some of the metallurgical factors responsible for solidification cracking. In addition, surface tension of the liquid metal affects solidification cracking by driving wettability of grain boundaries and inter dendritic liquid metal flow.

To explain solidification cracking from a mechanical standpoint, Pellini [6] proposed strain theory that involved the rupture of a liquid metal film when strained beyond a critical point as determined by the weld cooling rate and solidification range. Although nucleation and propagation of solidification cracking in welding are still issues of debate among researchers, the common

solution for welding AA6061 products is to use filler metals from the silicon rich 4000 series aluminum alloys or the magnesium rich 5000 series aluminum alloys. Kou [20] observed that introduction of filler material reduced the thermal gradient of the melt zone during solidification and thus, could be resolving the cracking problem during welding. Other methods such as preheating of the base materials [21] and use of backing strips [22] have also been investigated. In reference [21], preheating was achieved during the pulsed laser welding process by introducing a second continuous wave laser beam. The preheating resulted in reduced cracking in the case of autogenous bead-on-plate welding of a 6000 series alloy, namely 6016 (not AA6061). The backing strip method [22] proved to be useful for autogenous welding of 5000 series aluminum alloy but could not be used to achieve crack-free autogenous welding of any 6000 series aluminum alloy. From the welding literature reviewed, it can be deduced that the solidification range and the cooling rate (i.e., solidification rate) of the liquid metal are two of the main factors dictating solidification cracking. The review also suggests that the introduction of filler materials and preheating of the weld zone have been successfully applied in welding to avoid cracking.

In the case of LPBF processing of crack-free AA6061, only limited success has been reported to date. For instance, Louvis *et al.* [3] reported delamination, and low relative density (89.5%) when AA6061 was processed using LPBF, and identified the formation of an oxide film as the major reason behind these issues. It was argued that the aluminum oxide film had a higher melting point than the precursor powder, and instead of melting, the oxide layer would break down in the melt-pool upsetting the bonding between two consecutive layers and causing delamination. In another study, the tendency of the precursor powders to pick up oxygen was identified as a major factor leading to delamination [13]. Besides the issues associated with delamination, AA6061 has been found to be highly crack susceptible when fabricated with LPBF technology.

For example, Fulcher *et al.* [5] indicated that crack formation during LPBF processing of pre-alloyed AA6061 was directly related to the high coefficient of thermal expansion, and a large melting range of the material. Studies by Loh, *et al.* [23,24] have also described thermo-processing features of laser powder bed fusion on AA6061, and showed crack formation and growth spanning multiple grains [24].

To circumvent some of the issues with LPBF processing of AA6061, several strategies have been explored. For example, LPBF fabrication of an unalloyed mixture of aluminum (Al), and silicon (Si) powders in the same proportions as in nominal AA6061 was studied by Robert *et al.* [15]. In typical solidification of AA6061, incongruent solidification over a temperature range of 80 K can result in hot tearing, and hence, crack formation. Robert *et al.* expected a more congruent solidification by ensuring the melting of Al only, and encapsulation of the un-melted Si particles within the Al matrix. This approach reduced cracks in the microstructure but did not fully eliminate cracking. Moreover, an elemental mixture that does not include all the alloying elements of AA6061, is a fundamentally different precursor material compared to a pre-alloyed powder. Further, the study did not report any mechanical properties of the fabricated parts that could be compared against the wrought AA6061 properties.

In another study by Martin *et al.*, AA6061 and AA7075 powders coated with zirconium (Zr) nanoparticles were used to demonstrate LPBF fabrication of the functionalized material without cracking [25]. Their results indicated that the components fabricated using the Zr nanoparticles functionalized AA6061 and AA7075 powders were crack-free, and they exhibited uniform equiaxed grains with approximate grain sizes of $\sim 5 \mu\text{m}$. The suppression of crack formation and the fine equiaxed morphology were reasoned to originate from the introduction of many nucleation sites provided by the Zr nanoparticles. Although the study did not report on the

mechanical properties for functionalized AA6061, it did show that the mechanical properties of functionalized AA7075 were within the limits for the same wrought alloy in the T6 condition. Despite these results, the introduction of foreign particles such as Zr in the AA6061 and AA7075 would require the modified materials to be requalified and certified for aerospace and other critical applications. Also, functionalization of the precursor powders by Zr nanoparticles requires an additional procedure consisting of an electrostatic assembly technique that could incur added processing costs. From the foregoing discussion, it appears that the previous strategies described with the use of LPBF have yet to achieve fabrication of crack-free, and nearly fully dense components using pre-alloyed and unmodified AA6061 powder that also have desirable mechanical properties.

Preheating of the powder during the LPBF process has been shown to have some beneficial effects. For example, powder bed preheating was used by Kempen *et al.* [7] to demonstrate crack and delamination free fabrication of M2 HSS tool steel. It was argued that reduction in residual stresses achieved by powder bed preheating at 200 °C helped the successful fabrication of this material. Similarly, Ali *et al.* [26] demonstrated a reduction in residual stresses and the improvement in mechanical properties of LPBF processed Ti-6Al-4V alloy at an elevated bed temperature of 570 °C. An optimum preheating temperature of 250 °C was determined by Buchbinder *et al.* [27] for residual stress and distortion-free fabrication of AlSi10Mg alloy. From the foregoing discussion, it can be concluded that strategies such as material preheating [7] or the introduction of nucleants [25] show a prospect for achieving required solidification behavior for crack prevention during LPBF fabrication of AA6061.

2.3 *In situ* Monitoring in LPBF: A Necessity

Design and material flexibility, reduced requirement for part specific tooling, and shorter supply chains are a few of the marked advantages of AM manufacturing processes. Many of these advantages are realized due to the form of stock materials that are used in AM. For instance, in metal AM, be it laser powder bed fusion (LPBF) or electron powder bed fusion (EPBF), metal powder in the particle size range of 15 to 80 μm of is the precursor material in contrast with more conventional manufacturing techniques, such as machining or welding where the work pieces are usually larger monolithic blocks of materials. Scope of this discussion is to identify the possible root causes of some of the defects that could be more easily formed in AM processes than would be possible in the above-mentioned conventional manufacturing techniques such as laser welding. To draw a comparison between these two processes, the Marangoni effect could be considered. The Marangoni effect is usually observed at the liquid gas interface where there is a gradient of surface tension induced by whether variations in concentration of constituents of different phases [28] and/or temperature variations [29] along the interface. The following equation is often used to determine Marangoni number of a system,

$$M_a = -\frac{d\gamma}{dT} \left(\frac{L\Delta T}{\mu\alpha} \right)$$

where, γ is surface tension in N/m, L is the characteristic length of the system, α is thermal diffusivity in m^2/s , μ is dynamic viscosity and ΔT is temperature gradient along the interface. Temperature dependence of surface tension property of material dictates Marangoni number and in turn determines the shape of the weld-pool as found in welding literature [30]. Effect of $\frac{d\gamma}{dT}$ on Marangoni forces was explained in the classic work of Heiple *et al.*[31]. Marangoni effects

relevant to additive manufacturing have been studied for electron beam melting [32], and laser melting [33]. In metal powder bed fusion AM technology, defect formation mechanisms for porosity, spatter, and denudation zone were studied from a Marangoni effect perspective [34,35]. Also the effect of Marangoni number was studied in directed energy deposition (DED) processes by Mukharjee *et al.*[36]. As suggested in the literature [37], a Marangoni number greater than 10^5

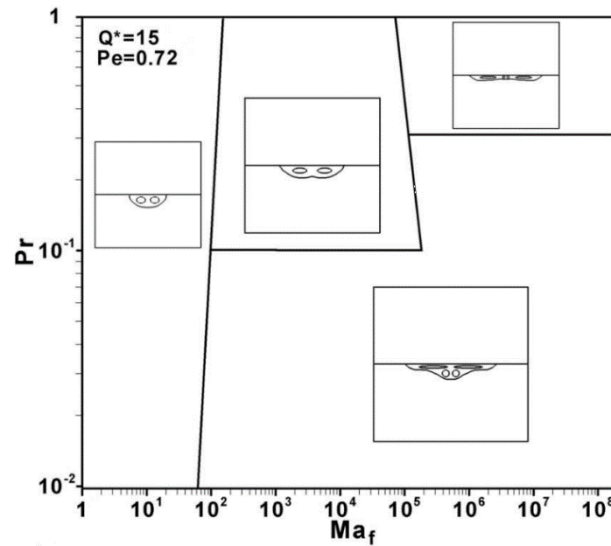


Figure 2.2 Marangoni number greater than 10^5 result is turbulent and therefore more unstable melt pool as shown by Mukharjee *et al.*[38]

would result in unstable melt-pool. Similar observations from numerical simulations were proposed by Mukharjee *et al.* [38] as shown in the Figure 2.2.

Due to much greater surface area of metallic materials in powder form than in the bulk form, smaller thermal diffusivity of powder material, and inherent larger thermal gradients in layer-wise AM process, there exists greater possibility of attaining larger Marangoni number for a melt-pool in powder bed fusion AM processes than in welding processes. This simple comparison of the two processes suggests that metal AM processes could be more defect prone; hence requires

elaborate process control to achieve the full potential of the technology. Control, however, could not be realized without *in situ* monitoring.

2.4 Review of in situ monitoring setups in LPBF processes:

Lack of accurate *in situ* monitoring and closed loop control techniques were identified as one of the key barriers for more widespread acceptance of metal AM in the manufacturing industry, and overcoming such barrier was set to be a high priority milestone in the roadmap for measurement sciences in metal AM by National Institute of Standard and Technology (NIST) [39]. Similar workshops and conferences around the world in AM communities also identified monitoring and control as one of the major issues with AM standardization [40].

Berumen *et al.*[41] described an in line monitoring system consisting of a high speed camera and photodiode sensors. The monitoring system was incorporated with Concept Laser GmbH (Lichtenfels, Deutschland) machine's quality management (QM) module. The initial design's detection system involved capturing the total build area in a single frame using a camera where the captured image would be converted to gray scale values based on the intensity of light emitted from different regions of the 250 mm x 250 mm build plate. Using the following equation 2.1, it was calculated that capturing a build with 150 μm hatch spacing and 500, 1000, and 2000 mm/s scan speed would require frame rates of 3333, 6666, and 13333 frames per second, respectively. Moreover, a camera sensor with 2000 x 2000 pixel to capture 250 mm x 250 mm build area would only devote 125 μm x 125 μm area per pixel. It would be worth mentioning that commercial LPBF machines usually employ a laser spot within 100 μm spot diameter. Therefore, 125 μm pixel would be insufficient to capture the melt pool's geometric features resulting in a very low-resolution image of the laser powder interaction zone. To capture the melt pool features, imaging of that zone should be done so that at least one and preferably multiple pixels cover the

area of the melt pool. In addition, an 8-bit image with 2200 x 2200-pixel resolution when captured at 16666 frames per second would generate 75.1 GB data per second. The quantity of data generated was calculated using equation 2.2 as shown below. This amount of data, a lot of which is imagery of build area beyond the point the point of interest, i.e. the laser-powder interaction zone, posed a formidable challenge for storage and processing; thereby, losing practical interest.

$$frames\ per\ second = \frac{scan\ speed}{hatch\ spacing} \quad (2.1)$$

$$data\ per\ second = (resolution_x)(resolution_y)(bit\ depth)(frames\ per\ second) \quad (2.2)$$

After identifying the problem, an in-line monitoring system such as the one shown in Figure 2.3 was proposed, which would only capture the data at the laser powder interaction zone and within its close proximity that would reduce the generated data to 0.636 GB with a 10 μm spatial resolution of the melt-pool. Such an improvement was realized by making sure that the

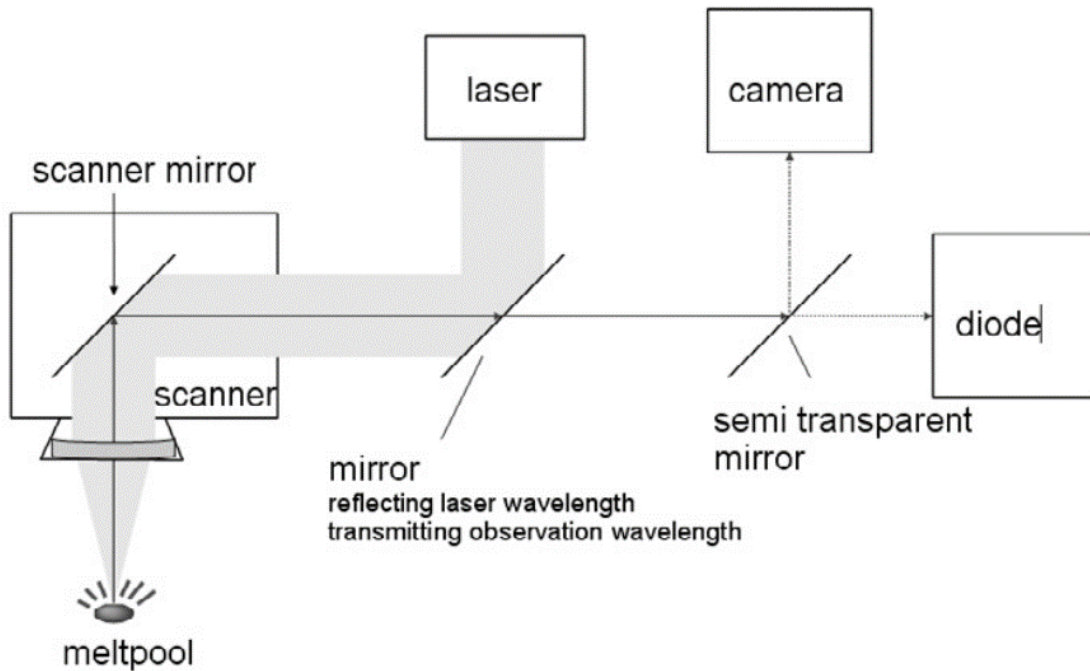


Figure 2.3 In line monitoring set up consisting of high-speed camera and photodiode sensor shown by Berumen *et al.* [41]

data were only captured from the region of interest instead of the whole build area. To complement the data obtained from the 10 kHz camera that provided information on the dimensions of the melt-pool, photodiodes were employed to obtain information on the amount of radiation from the melt-pool. Determination of utility for quality management by using the melt pool monitoring data, and different related processing algorithms were still under study during the publication of the article.

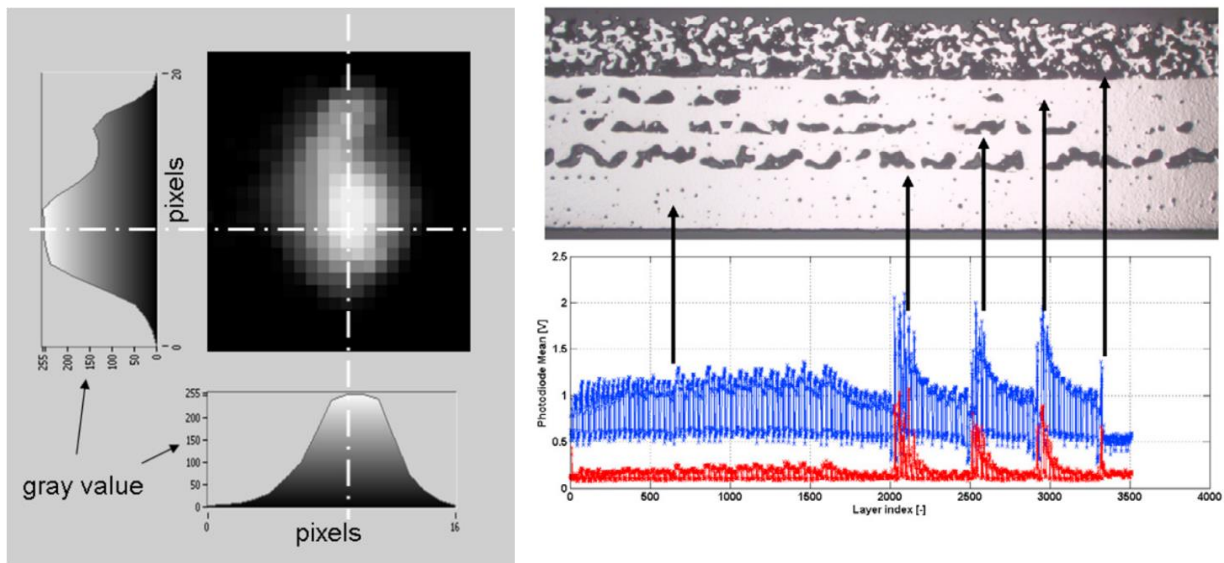


Figure 2.4 (a) gray scale image of the data obtained from the in-line high speed camera showing the dimensions of the melt pool in x and y direction (b) photodiode detected intensity of the light emitted from melt pool; increased intensity around layer 2000, 2600, and 3000 correspond to process error where larger amount of powder was deposited due to un-synced movement of the build platform [41]

Lott et al. [42] from Fraunhofer-Institute for Laser Technology ILT (Aachen, Germany) invented a setup for LPBF processes where a secondary illumination laser would be used to illuminate the melt-pool and surrounding area side by side with the processing laser. A

combination of optics consisting of dichroic mirror for the processing laser, beam splitter for the illumination laser and f- θ objective lenses were employed for capturing melt-pool dynamics. Being in line with the processing laser, the data obtained from the setup required high speed CMOS camera to match the laser scanning speed and provide enough data points to apply fast fourier transformation (FFT). Required optical components for the setup, and preliminary image obtained from the set up are shown in Figure 2.5.

Clijsters *et al.* [43], also from The Katholieke Universiteit Leuven (Leuven, Belgium), improved the analysis tool of Berumen *et al.*'s. [41] device. Instead of resolving the data in the time domain as it had been done in reference [41], the latest work in reference [43] resolved the data so that it could be related to a particular layer in the build and not merely to a point in time . The same monitoring system described in reference [41] was used for this study. The system consisted of a photodiode and a CMOS camera, both active in the spectral range of 400 nm to 1000 nm was used for this study. However, to avoid visible light and the processing laser of 1064 nm

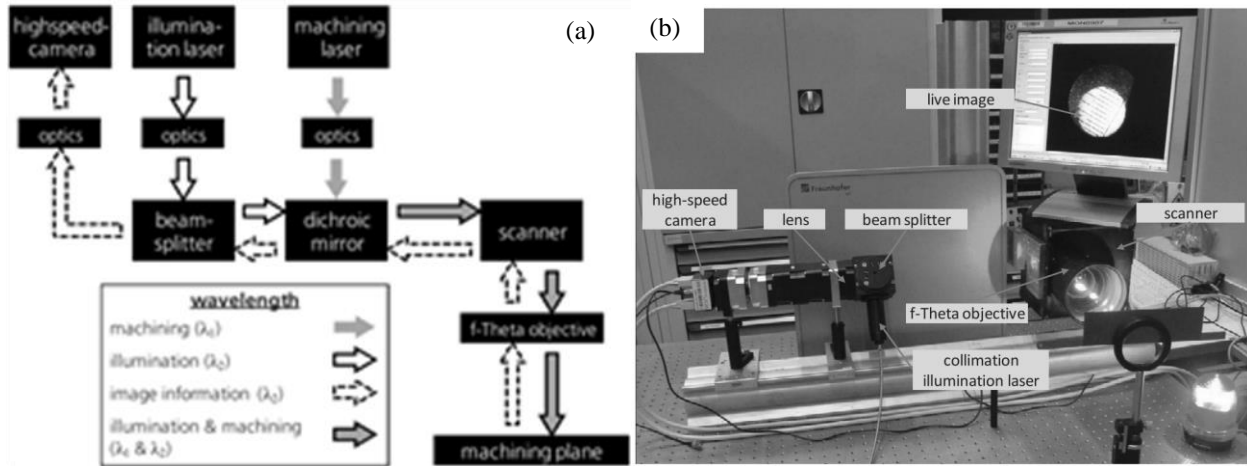


Figure 2.5 (a) block diagram of the different optical component required for the in-line melt-pool imaging setup invented by Lott *et al.*[42] (b) actual setup with an image of the melt pool and surrounding area with a 5 mm x 5 mm field of view

in the lower and higher end of the sensors' spectrum, optical filtering was implemented in such a manner as to allow only 780 nm to 950 nm radiation of be incident upon the sensors.

Data obtained from the two types of sensor would complement each other. For example, the photodiode would provide measure of the melt area in a high resolution by integrating the intensities during the melt time. However, the length and width of the melt-pool could not be discerned from the photodiode data alone since it represented the intensity of the whole, not along the length or width dimension in particular. To determine the dimensions, the CMOS camera that had a lower resolution than the photodiodes was found helpful. Clijsters *et al.* [43] indicated that the integration of a real time feedback control in the LPBF systems would require higher speed of data processing (i.e. >10 kHz) than could be availed using the existing image processing software. Therefore, field programmable gate arrays (FPGA), which is basically a dedicated computer on a chip, was used for data handling. It was determined that FPGA would require only a single clock cycle (40 MHz) to pass on the processed data to the controller for the feedback loop after the last bit the image data had entered the FPGA.

Clijsters *et al.* [43] developed a mapping algorithm for processing the photodiode and CMOS camera data as shown in Figure 2.6 (a). Figure 2.6 (b) demonstrated successful detection of porosity at the beginning of a scan vector corresponding to larger melt pool. Such an algorithm was deemed necessary to facilitate defect detection of the builds, quality control, and implementation of feedback control. For each scan vector, pointwise intensity values were obtained and correlated to a grey value. Only the scan vectors inside a 95% confidence level interval was considered for analysis. These grey values were then plotted in a regular grid. To determine quality of a build using such data, reference data in the form of 'perfect' build would be necessary. Two different methods of producing reference data were discussed; one, to qualify a

series of parts using the conventional analysis techniques such as density measurements, metallography, etc. and then using the corresponding parameter generated intensity values as reference, and two, to use prespecified dimensional accuracy, surface roughness, production speed, etc. as a gage of 'perfection' for the scan vectors. Sensor data from any arbitrary build would then be compared to a corresponding reference data to determine the quality of the build under

discussion. Porosity detection using the algorithm under discussion was demonstrated as shown

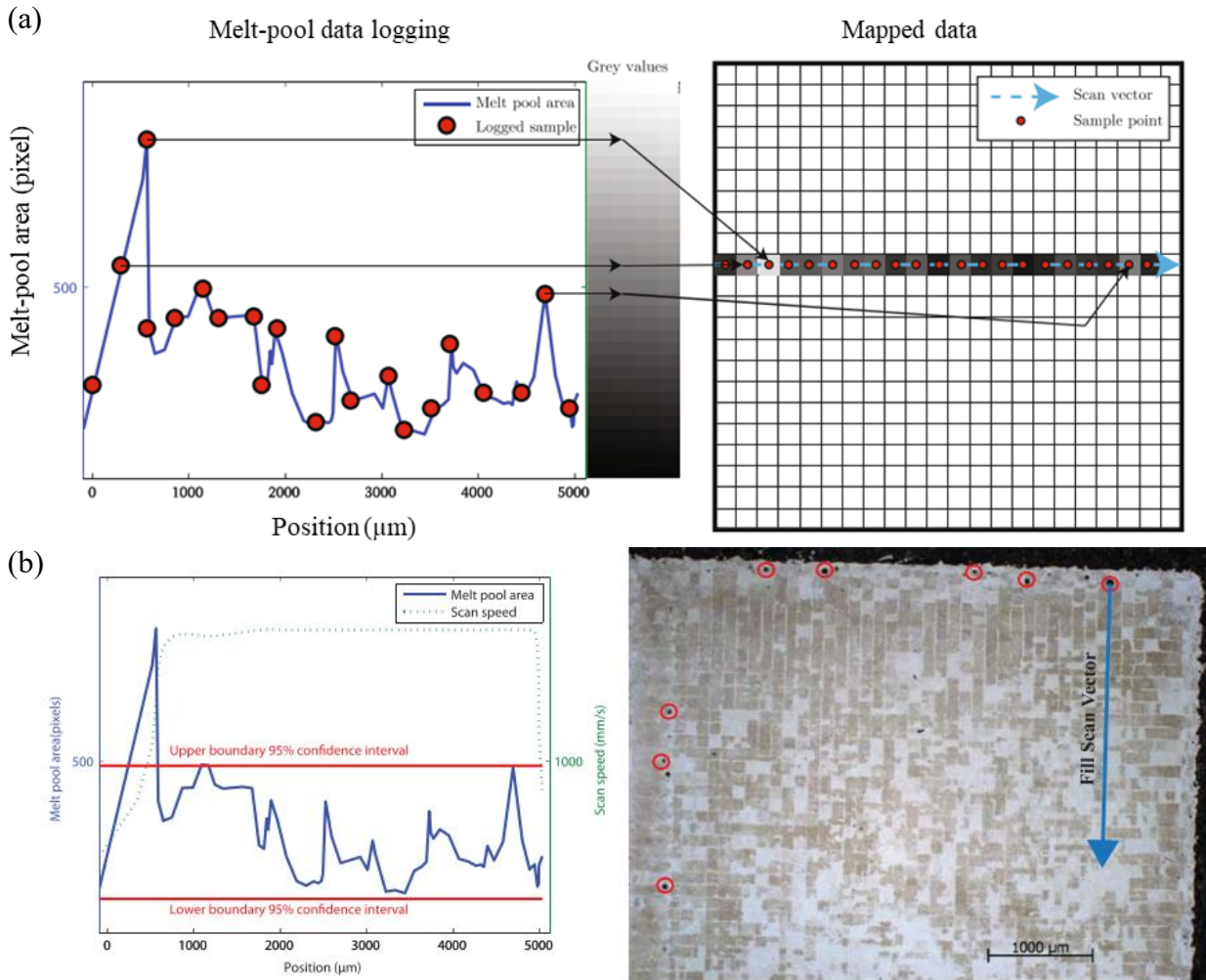


Figure 2.6 (a) Illustration of mapping algorithm used by Clijsters *et al.*[43] On the left is are the intensity values obtained by the photodiodes and corresponding grey scale values. Grey scale values were plotted in a rectangular grid as shown on the right side of image. Mapping of only a single vector is shown; when all the vectors in a layer is mapped, a grey value representation of the entire layer could be obtained. If multiple points corresponded to a single grid, the average of those intensities were considered for that grid (b) Porosity corresponding to high laser power and corresponding larger melt pool as detected by the proposed monitoring system

in the Figure 2.6 adapted from Clijsters *et al.* [43].

Doubenskaia *et al.*[44] developed an *in situ* monitoring system which was integrated with a PHENIX PM 100 (Phenix Systems, France) laser powder bed fusion system. The system consisted of visual monitoring capability of the build area and a two-color pyrometer. The visual monitoring system used an illumination laser of 440 nm and a video camera. An image captured using the visual observation system of the PHENIX PM 100 was shown in Figure.2.7. The surface temperature monitoring setup complementing the visual observation system used two InGaAs photodiodes with wavelengths 1.25 and 1.36 μm that could measure temperature in the range of

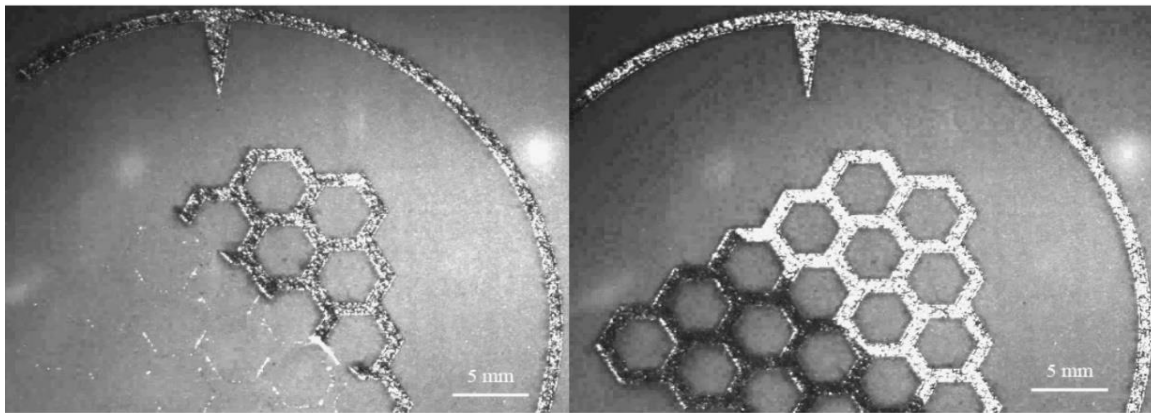


Figure 2.7 Image obtained from the visual observation system developed by Debenskaia *et al.*

[44] where the effect of single and double scanning of the same layer is visible by difference in visual contrast. The layer that had been scanned once, appeared darker in the visual observation system

900 to 2800 K when calibrated against a black body. Doubenskaia *et al.* [44] reported signals from

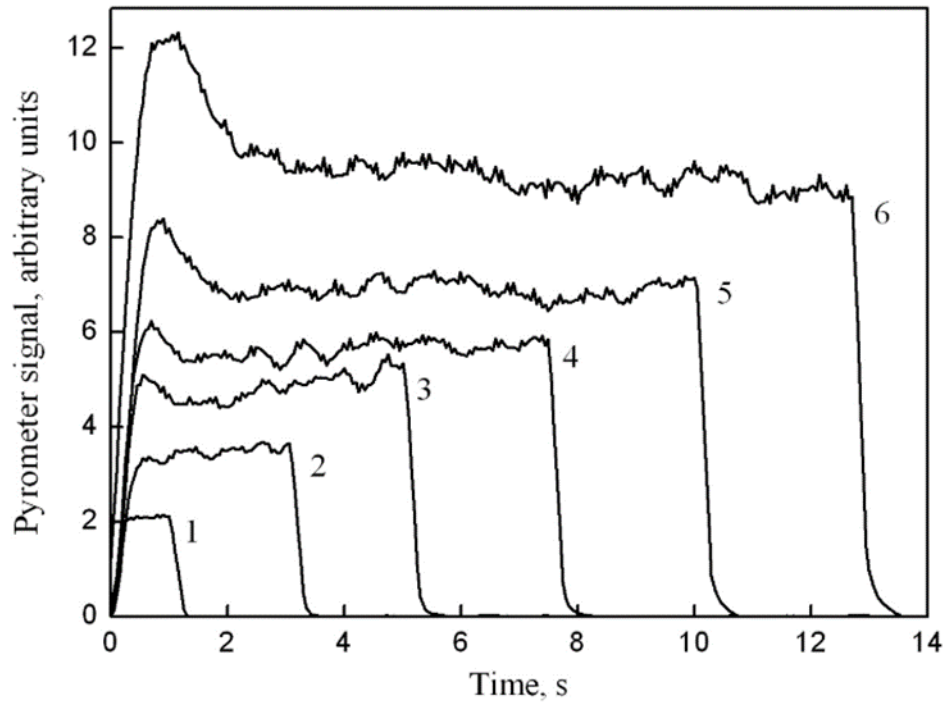


Figure 2.8 Signals from the pyrometer in arbitrary units showing the effect of change in hatch spacing on temperature as observed by Debenskaia *et al.* [44] Curves 1 through 6 represents builds with different hatch spacings when all the other scanning parameters were kept unchanged. Curve 1 represents the build with 1 mm hatch spacing and 6 represents a build with 70 μm layer hatch spacing. Layer temperature with smaller hatch spacing was considerably higher because of the higher energy input within the same area in the latter case

the photodiodes in arbitrary units that reflected change in processing parameters as shown in the Figure 2.8.

Furumoto *et al.* [45] devised a two-color pyrometer to study the consolidation of a mixture of nickel and copper powder when irradiated with laser. A sandwich of InAs and InSb detectors was used for detection of radiation with wavelength ranges 1 to 3 μm and 3 to 5.5 μm respectively.

Such a combination of detectors were used following the work of Ignatiev *et al.* [46]. The pyrometer was calibrated up-to 1000 °C using thermocouples, at 1510 °C by melting a steel sheet and at 2200 °C by melting of SiC. This work did not consider the effect of emissivity changes due to changes in surface condition. Also, in case of ratio pyrometry it is always desirable to calibrate the instrument using the materials that would be used during the actual test. These factors would render the temperature measurements from the two color as relative only and not actual surface temperature. However, Furumoto *et al.*[45] provided a functional description of the two color pyrometry that could be used for future development of two and other multi-color/multi-wavelength pyrometer. Although relative, the two-color pyrometer setup under discussion captured the change in maximum temperature with change in laser power during the consolidation of metal powder as shown in the Figure 2.9 (a). Another noticeable aspect of the work by

Furumoto *et al.*[45] is the functional description of how the temperature could be calculated using

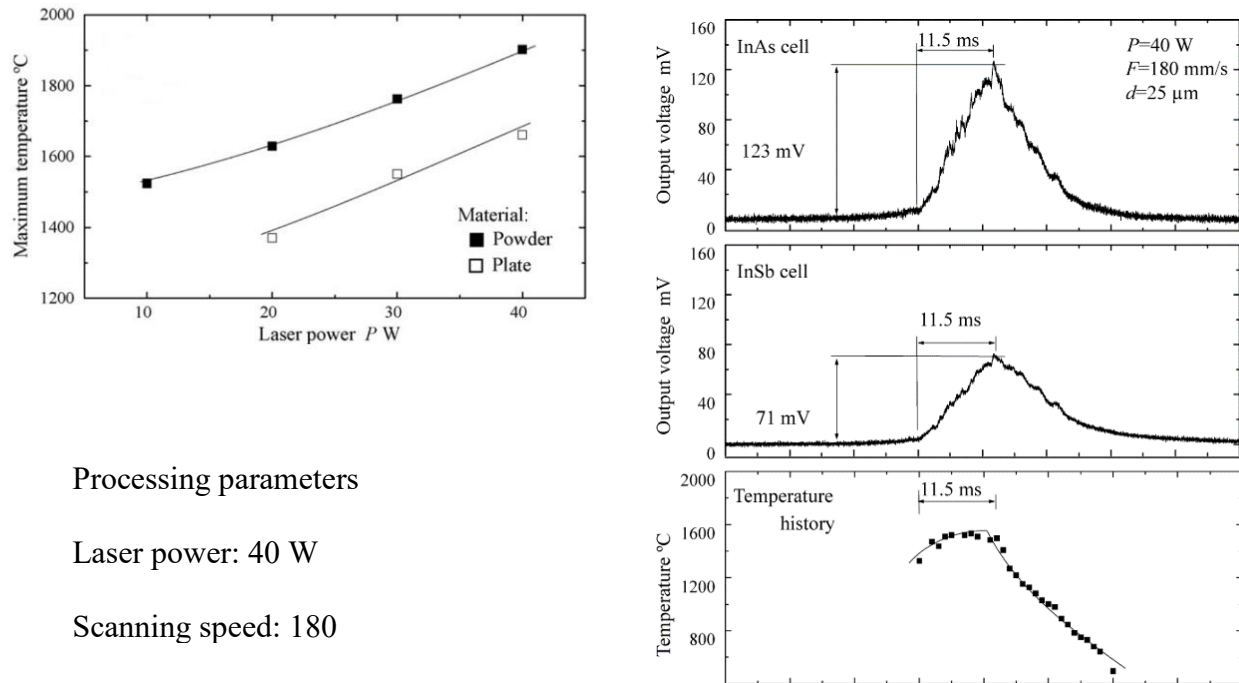


Figure 2.9 (a) the effect of laser power on the maximum temperature of laser and powder interaction zone as reported by Furumoto *et al.* [45]. However, caution should be maintained before considering the temperatures as true surface temperature since the effect of emissivity could not be considered. Also, the measured area was greater than the process interaction zone. Temperature of the substrate plate was the signal output from the detectors. Graphical representation of the concept is also shown in Figure 2.9 (b).

Furumoto *et al.* [47] also used high speed (10,000 frames per second) video imaging for monitoring the consolidation behavior of metal powders using the same custom machine as mentioned in the reference [45]. In this setup, the camera was set up vertically on top of the scan vector and the processing laser was placed at an angle of 45° . A metal halide lamp was used for illumination of the build area under imaging. The setup is shown in the Figure 2.10 as adopted

from Furumoto *et al.* [45]. The study in reference [47] was followed up with an investigation of temperature effects on powder consolidation and shrinkage behavior. It was argued by Furumoto *et al.*[48] that the laser irradiated molten metal powders pulled un-melted metal powders from the circumference of the melt-pool. Although the authors did not comment on the surface quality of

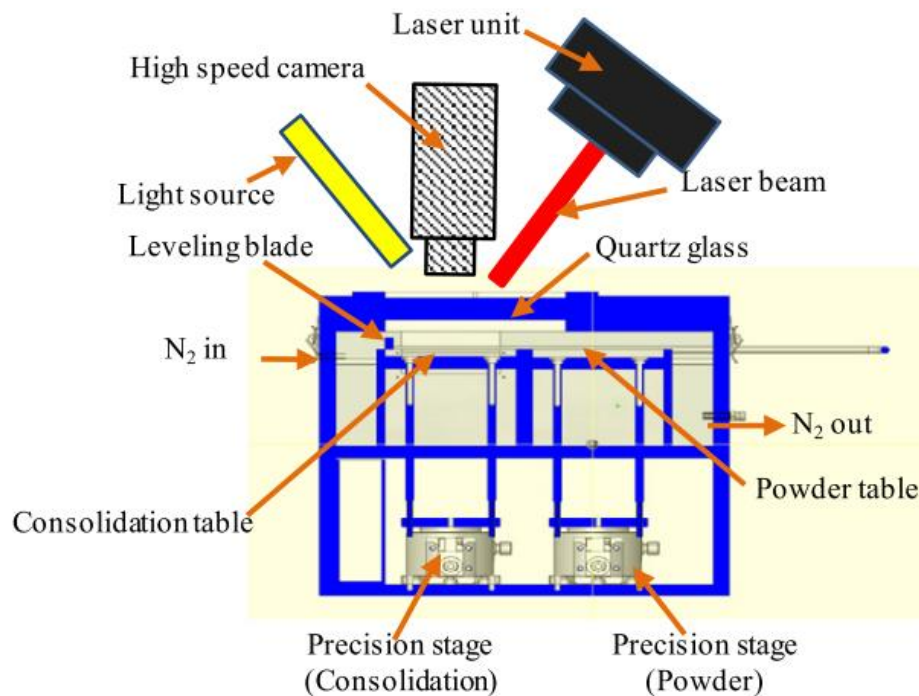


Figure 2.10 Set up devised by Furumoto *et al.*[48] for investigating the consolidation behavior of metal powder upon laser irradiation

the solidification, the images presented in the reference [48] borne evidence of balling or turning in spheroid shape due to over melting. Width of solidified single vectors scanned at different area-

based energy densities (i.e. J/mm^2) was presented as an indication of shrinkage behavior of the

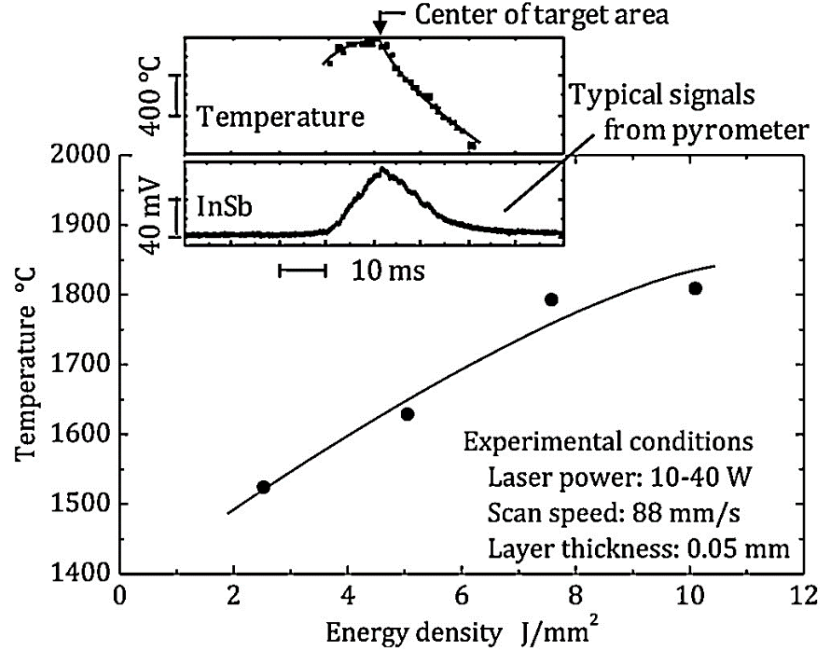


Figure 2.11 The change of temperature of the melt area with change in energy density during the melting of stainless steel powder by laser irradiation as reported by Furumoto *et al.*[48]. Caution should be maintained before considering the reported temperature as the true surface temperature since this study did not consider the effect of emissivity change as a function of temperature melt track. Also, the maximum temperature of the laser and powder interaction zone was showed to vary with input energy densities as shown in Figure2.11.

Zavalov *et al.*[49] developed a six channel setup to study a 3 mm diameter spot melting of 350 μm thick single layer of the alloy PR-NX17SR4 (IIP-HX17CP4) on a 3 mm thick stainless steel substrate. Each channel would acquire spectral data at different spatial location of on and around the laser powder bed interaction zone. The channels had two photodiodes each active at different spectral ranges, such as 1700 to 2200 nm, and 950 to 1400 nm. Use of two different type of photodiodes at each channel was to capture IR spectral data with and without the processing

laser. The first of photodiodes responsive at 1700 to 2200 nm would exclude the processing laser of 1070 nm. Acquired spectral data at each channel was integrated over an area of 70 μm diameter which was the spatial resolution of each channel. A schematic of the setup is shown in Figure 2.12.

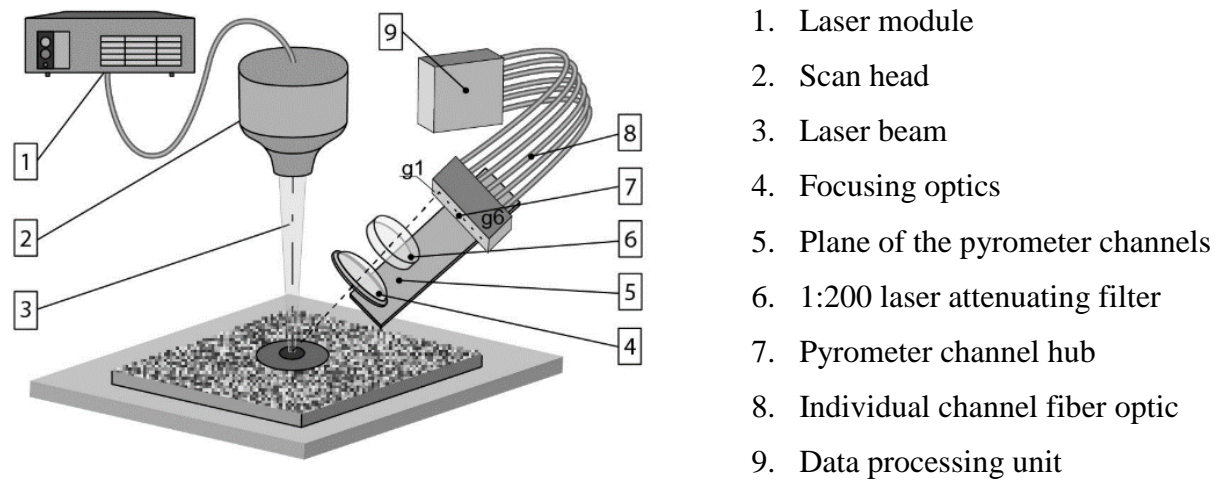


Figure 2.12 Multi channel spectral data analyzer developed by Zavalov *et al.* [49] Each channel collects data at different spatial locations and at two different wavelength ranges

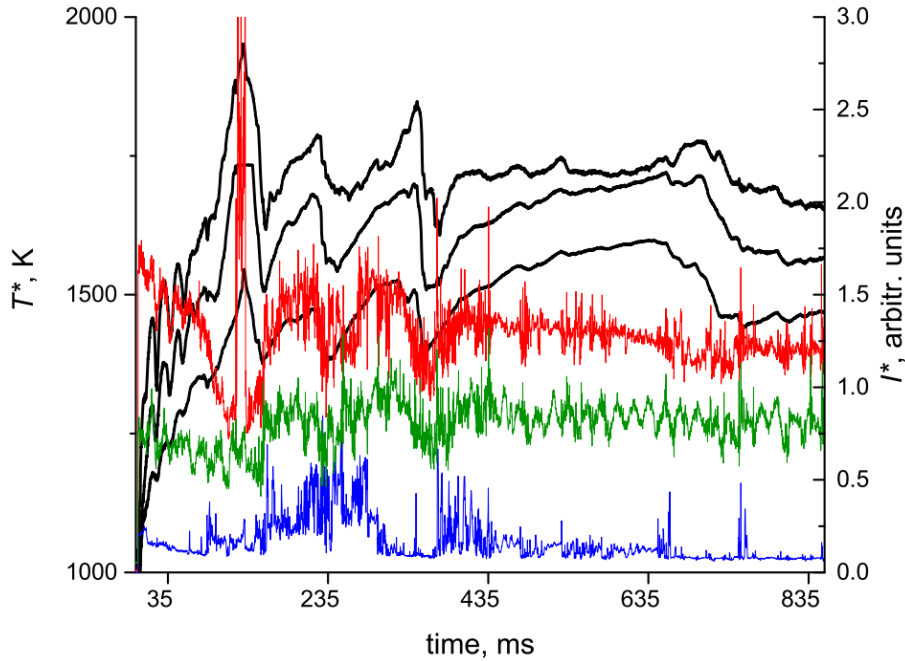


Figure 2.13 Zavalov *et al.* [49] reported brightness temperature and corresponding signal intensity are shown for channels 1, 3, and 5 i.e. 0, 0.6, and 1.2 mm away from the laser and powder bed interaction zone. Curves in black denote brightness temperatures, the colored graphs denote intensity values at the channel 1 (red), channel 2 (green), and channel 3 (blue)

Data obtained using this setup identified the temperature changes associated with different heat and mass transfer phenomena that occur in the laser powder bed interaction zone. A typical plot of pseudo or brightness temperature (T^*) i.e. temperature not corrected for emissivity, and raw signal intensity (I^*) from the channels 1, 3, and 5 from Zavalov *et al.* [49] is shown in the Figure2.13.

Montazeri *et al.*[50] monitored the melt-pool of a test artifact consisting of a designed overhang in a LPBF machine equipped with a short wavelength IR camera, a high speed video camera, and a photodetector installed off-line with the processing laser. The study reported a new approach, namely spectral graph technique, to analyze the sensor data to determine indication of

failure. The technique involved creating a dictionary of eigenvectors and eigenvalues extracted from the spectral graph obtained after mapping each individual sensor data using vertices and edges with weights specified according to spectral graph theory. The eigenvalues and eigenvectors were hypothesized to have signature peaks corresponding to the sensor values obtained from different regions of the build, such as bulk, overhangs, thin features, etc. The study tested the spectral graph theory on the three different sensors, data by feeding 250 randomly chosen build sequence in the model. Images from the thermal camera were found to be most successfully distinguish between overhang and bulk areas of the build.

Imani *et al.* [51] from the AM group at Penn State used DSLR still camera for process monitoring in LPBF process. Two pictures of each layer were captured; one, right after the melting, and the other, immediately after the recoating of the layer as the camera shutter was controlled by proximity sensors placed to detect rake movement. Post fabrication XCT analysis was performed and the effect of input laser energy density on porosity formation was studied. The monitoring aspect of the work included application of the spectral graph theory and multifractal analysis to the still images obtained at every layer and tracing them back to different processing conditions. The authors argued that combination of spectral graph and multifractal analysis was more suited for robust monitoring systems than the conventional statistical analysis tools. However, the authors also recognized the approach as indirect way of quality assessment in LPBF processes that could not indicate the location of the defect in the build, yet.

Yuan *et al.*[52] at Lawrence Livermore National Laboratory (CA, USA) used convoluted neural network (CNN) approach of machine learning to analyze video data obtained from single track scanning of SS 316 powder. The aim of the work was to develop a faster method of generating labelled features from videos obtained *in situ* measurements. The authors remarked

that although high speed images or videos were routinely captured using state of the art on-line and off-line monitoring setups, analysis of these images and videos still lacked development in methods and tools. In this work, 870 separate scans with a length of 5 mm and four different combinations of laser power and scan speed were made on a steel substrate. The consolidated scans were measured, and their heights were profiled by using a Keyence VR3000. These *ex situ* measurements were correlated to the corresponding video images by a mapping algorithm developed by Yuan *et al.*[52] where three distinct features such as, track, etch (depression due to laser engraving that could result during the process) and background (the substrate plate) were identified in the images. Those images were then used to train the CNN model to predict the properties of the scan tracks. The characteristics of the melt tracks that were evaluated in this study were the width, continuity, and standard deviation of the width measurements. Such models could be used for monitoring and quality management of the builds in LPBF on the fly.

Nassar *et al.* [53] studied the optical emission using two photodiodes sensitive at 520 nm and 530 nm, respectively when the optical radiation from the melt pool went into the sensors through bandpass filters with 10 nm FWHM tolerance around the respective wavelengths. Image of the total area of the build plate, instead of just the melt-pool, was projected on the photosensitive part of sensors after a magnification of -0.07. The monitoring was performed during LPBF processing of Inconel 718 cylindrical test coupons with different processing parameters. The control part that were expected to be defect free was scanned with parameters prescribed by the ProX 200 DMLS machine manufacturer 3D Systems. The authors proposed a parameter called ‘line to continuum ratio’ which was basically the ratio of difference between the response from the two photodiodes sensitive at 520 and 530 nm, and the response from the photodiode with sensitivity at 530 nm. This ratio was expected to correlate with the amount of porosity observed

in the parts after ex-situ analysis using XCT. The implicit hypothesis was that a high emission of

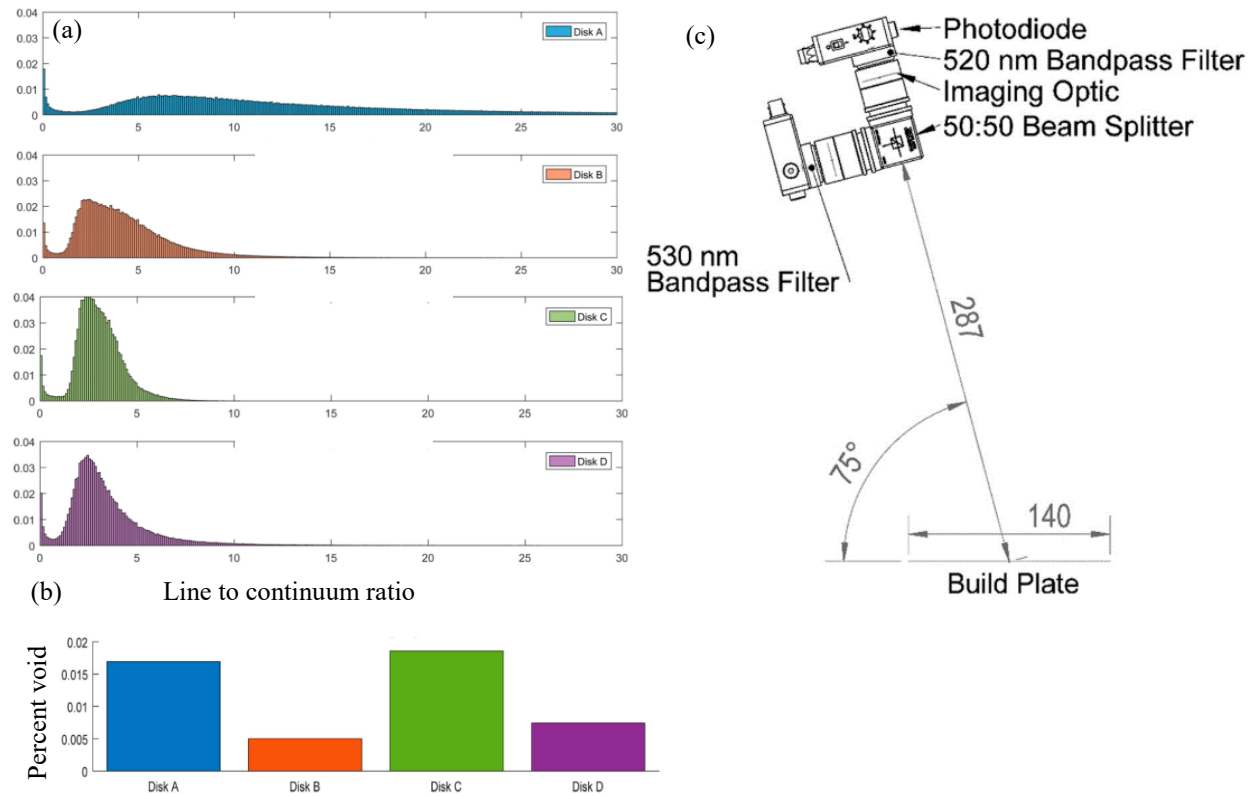


Figure 2.14 (a) Plots of normalized histogram of line to continuum ratio occurring at different disks i.e. different processing conditions (b) percent void, a measure of porosity at different processing conditions (c) Experimental set up used by Nassar *et al.*[53]

chromium would indicate overheating of the melt pool and corresponding porosity generation. The results did not show any decisive correlation between the porosity and line to continuum ratio as can be seen from Figure 2.14 adopted from Nassar *et al.*[53]. Comparing Figure 2.14 (a) and Figure 2.14 (b) it could be observed that although the disk A with a higher line to continuum ratio had a higher level of porosity, the opposite was true for disk C that had a higher porosity despite lower line to continuum ratio. The authors explained such behavior as lack of fusion in case of

disk C which, even if correct, would deter drawing any direct correlation between the line to continuum ratio and build quality until further improvement of the methods are proposed.

Leung *et al.* [54] used *in situ* high speed synchrotron X-ray imaging to study the melt pool dynamics during the first and second layer of a LPBF process. A small powder bed with dimensions 30 mm x 3 mm x 0.3 mm was inserted into the X-ray chamber. A 200W Ytterbium-doped fiber laser with a wavelength of 1070 nm was used as processing laser. The setup provided excellent insight into the physics and dynamics of melt-pool formation, spatter trajectory, formation and migration of porosity, effect of Marangoni force in defect transportation in LPBF process, etc. Such highly sophisticated instrumentation could provide data for process modelling and simulation as the authors recognized. However, applying this technique for monitoring parts' quality in industrial scale manufacturing operation is, unfortunately, a farfetched idea due to the high cost and limitation in setup.

2.4 Rationale of the current research considering the literature review

The literature review in section 2.1, 2.1 and 2.3 was intended to serve as a background and rationale for the research performed within the scope of the current thesis. In section 2.1 a brief overview of the AM process in general and LPBF process in particular was provided. Section 2.2 was dedicated for the review of LPBF fabrication of AA6061. From the literature, different challenges of AA6061 LPBF fabrication, such as low laser absorptivity of 7% or lower, tenacious oxide films, high thermal conductivity of 167 W/m-K, high coefficient of thermal expansion of $23.4\text{ }^{\circ}\text{C}^{-1}$, and wide solidification range of approximately 80 K were identified. These properties of AA6061 resulted in crack formation during LPBF fabrication of the alloy. Crack formation during the welding of AA6061 without using a filler material was obvious, and filler material would be routinely used for welding of the alloy. However, due to the nature of LPBF process as

described in section 2.1, use of such filler material would not be possible. Due to the design flexibility offered by AM processes, industrial pull for the LPBF fabrication of AA6061 and that of AA7075 with similar solidification characteristics was in place. Therefore, directing research towards the LPBF processing parameter development of these alloys was necessary. The use of preheating as a means of reducing residual stress and distortion of the fabricated parts had already been in practice for welding process. To address the issue of crack formation during the LPBF fabrication of AA6061, powder bed heating was used in the current research with the hypothesis that the preheating would help reduce the strain on liquid film during solidification process by widening the liquid metal transportation channels at the latter stage of solidification process.

Measurement and understanding of the effect of powder bed heating on LPBF fabrication process were deemed necessary. Accurate temperature of the build during fabrication could be considered as a property to indicate the effect of powder bed heating. Such monitoring could also serve for LPBF process control and standardization. Therefore, in section 2.3, literature on *in situ* monitoring of LPBF process was reviewed with an interest in studying the setups, instruments, and algorithms used for temperature measurement. The literature review revealed that the accurate temperature measurement could not be achieved due to the lack of understanding of the emissivity characteristics of the precursor metal powder as it underwent melting and subsequent solidification. A technique called multiwavelength (MW) pyrometry could measure the surface temperature without prior information of the target's emissivity. The genre of noncontact temperature measurement techniques called pyrometry is reviewed dedicatedly in Chapter 4. In the current study, MW pyrometry was employed for the emissivity profiling of the metal powder at different temperatures, and custom monitoring windows were designed and fabricated for

demonstrating *in situ* accurate temperature monitoring in an experimental open architecture LPBF system.

Chapter 3: Experimental Setup and Methodology

3.1 AconityONE Experimental LPBF System

Modularity and access to modification of software and hardware of the AconityONE machine justifies its reference as an open architecture system. The machine has the following principal modules, most of which could be independently controlled, but also integrated by the HTML based ‘AconityStudio’ software.

- 1) Laser unit with 3D scanning device
- 2) Induction heater unit
- 3) High-speed CMOS camera
- 4) High speed single wavelength pyrometers

There is a range of parameters available to alter and experiment within AconityONE. A description of the relevant terms used in laser powder bed data preparation is presented below in Table 3.1 and Figure3.1 [55]. When parameters such as hatch spacing, beam rotation, hatching stripe lengths, and others need to be configured in the data preparation software Materialise Magics or Netfabb, some other important parameters such as laser power, scanning speed, beam defocus, laser jump delay, etc. could be accessed and changed using both the data preparation software, and

Table 3.1: Common file preparation parameters [55]

Beam compensation	μm	Space between the center of the beam and the real contour of the part. (\sim half of melting bath width)
Beam diameter	μm	The diameter of the beam on the building surface
Number of contours	-	Common is one contour. Two or more contours could also be done
Contour 1 spacing	μm	Distance between innermost contour and the hatch
Contour 2 spacing	μm	Distance between the contour 1 and contour 2
Contour laser power	W	Laser power for scanning the contour vectors
Contour scanning speed	mm/s	Scanning speed for scanning the contour vectors
Hatch laser power	W	Laser power for scanning the hatch vectors
Hatch overlap	μm	The overlap of the welding trace
Hatch scanning speed	mm/s	Scanning speed for scanning the hatch vectors
Hatch spacing	μm	Space between hatch vectors.
Layer thickness	mm	Moving height of the platform per layer
Scan strategy	-	There are different scanning strategies. Stripes and checkerboards are common.
Stripe overlap	mm	The overlap between the stripes
Stripe/beam rotation	$^{\circ}$	The rotation of the stripes per layer
Stripe width	mm	Stripe width is the length of a vector

AconityStudio after the build file is loaded in the machine. In AconityONE, laser power and

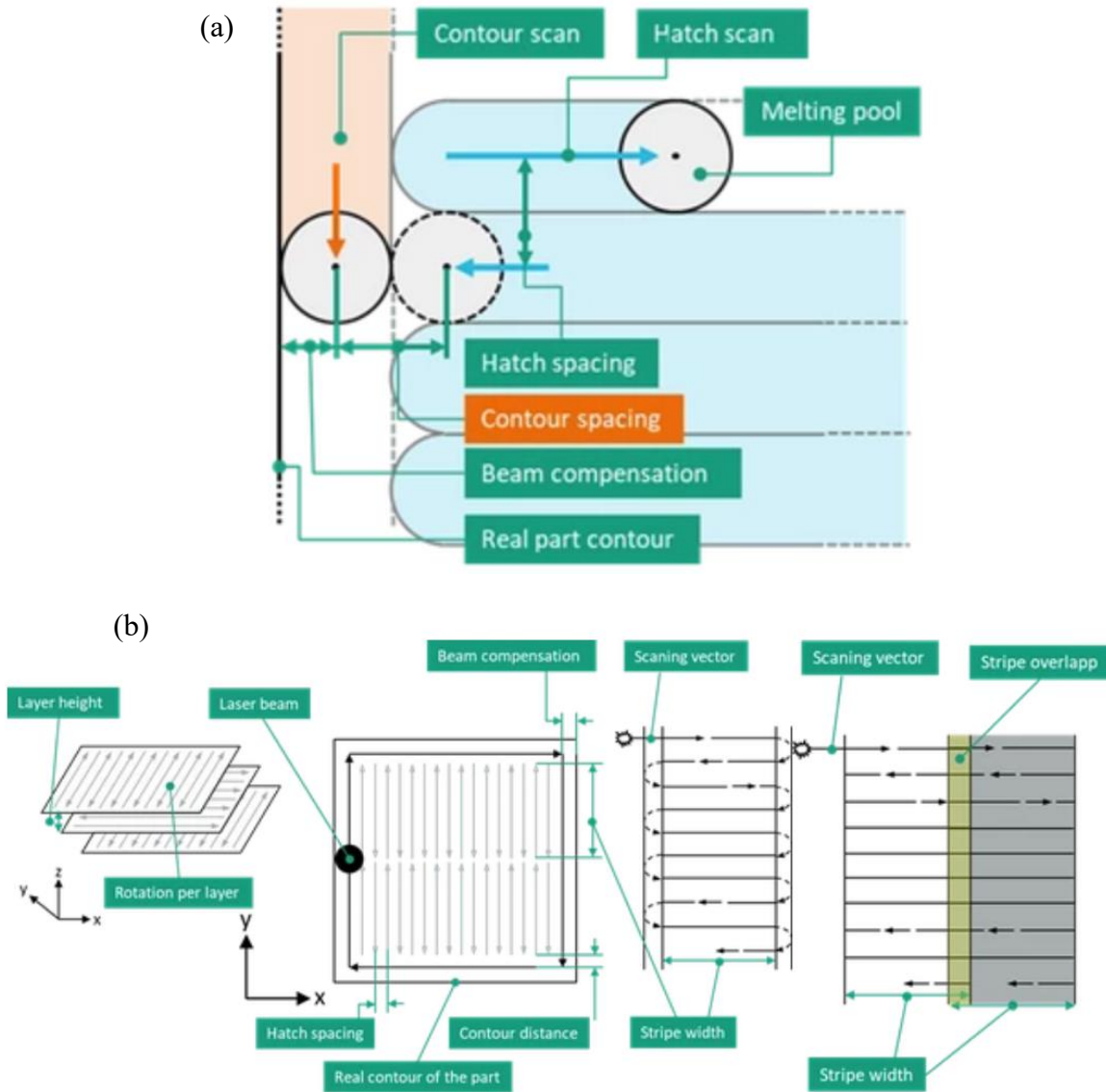


Figure 3.1 (a) and (b) depict different build file preparation parameters [55]

scanning speed for different components of the build file i.e. up skin, down skin, contour, infill, supports, etc could be altered in the middle of build by pausing the job.

AconityONE incorporates a 3D scanning device AXIALSCAN-12 (Raylase, Wessling, Germany). The scan-head has the capability of dynamically adjusting the focus spot diameter to

ensure uniform power density in a 600 mm by 600 mm field of scanning. The spot size could be

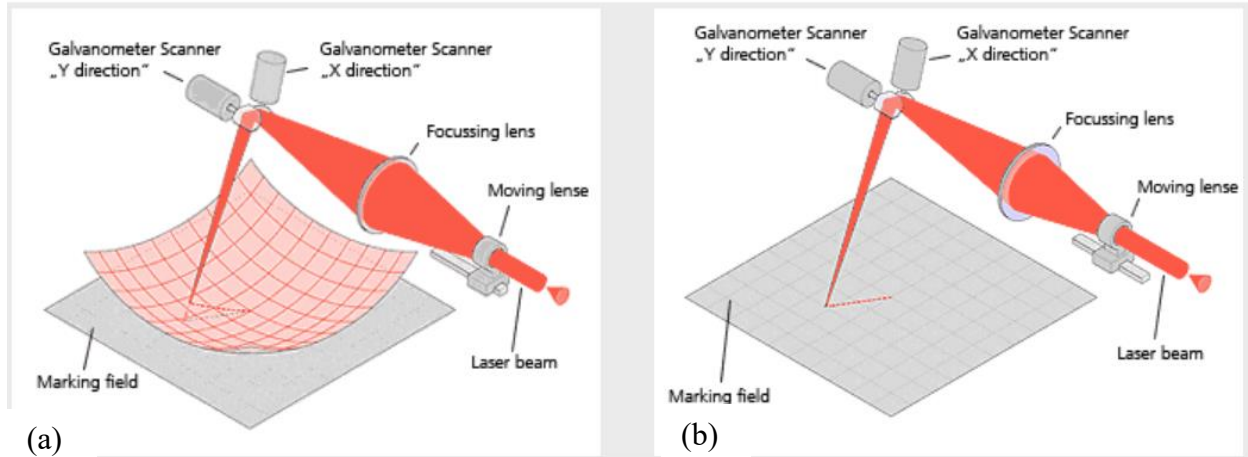


Figure 3.2 A uniform power density could be ensured by introducing a moving lens to consistently adjust the beam focus and hence spot diameter. (a) Moving lens is kept static to depict that the focal plane could curve out of build surface (b) Movement of the lens ensures dynamic focus change and therefore, uniform power distribution throughout the build area. [56]

varied between 80 μm to 500 μm . Figure 3.2 shows the advantage of maintaining desired focal plane using an adjustable lens [56].

The scan head also houses optics for an in-line monitoring set up consisting of a 5 kHz CMOS camera named EoSens® 3CXP (Mikrotron-GmbH, Unterschleissheim, Germany), and two Kleiber KG Series 740 – LO-100 kHz pyrometers (KLEIBER Infrared GmbH, Unterwellenborn, Germany). The CMOS camera is a maximum view field of 4 mm by 4 mm area and requires an illumination laser. An 808 nm wavelength diode laser system (model # dst11-t192, OsTech e. K., Berlin, Germany) of highest 50 W capacity at 40 mA is used to illuminate the melt pool for viewing using the camera. The two 100kHz pyrometers probe the thermal spectrum at the medium wavelength infrared range from 1580 to 1800 nm. Two pyrometers measuring at the same

wavelength could be used to obtain an instantaneous spatial thermal gradient when the pyrometers' measuring spots are set apart at a known distance. Usually one pyrometer is set at the laser spot,

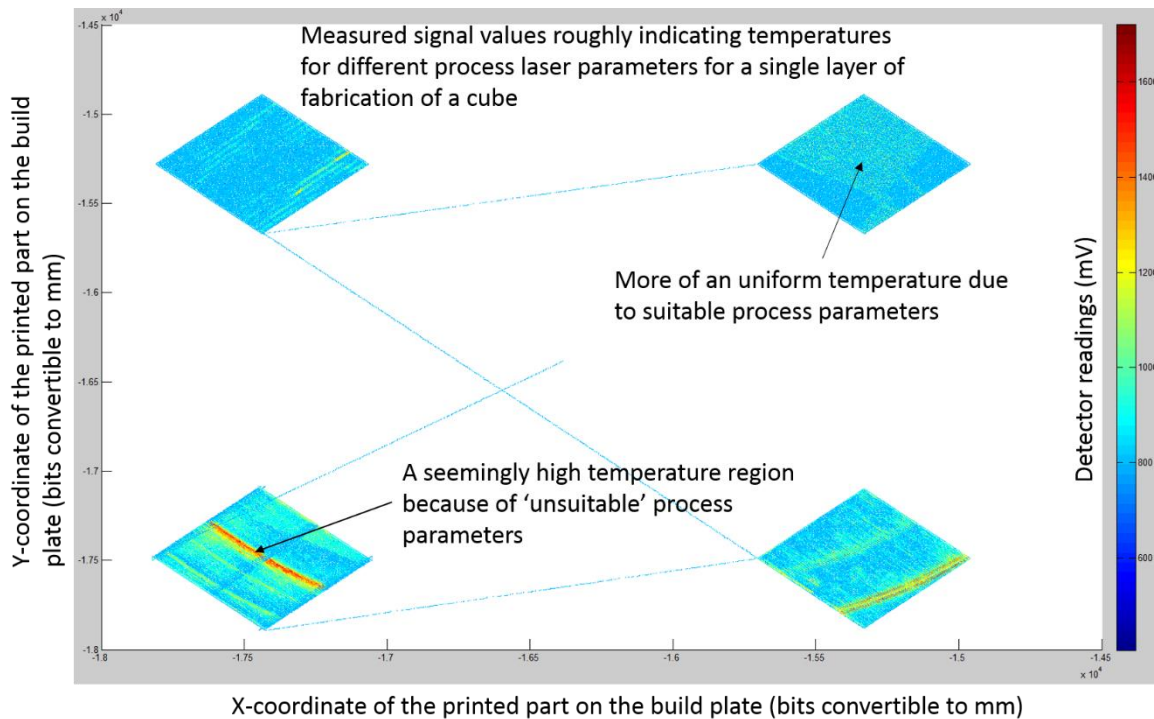


Figure 3.3 Image showing measurements made on a single layer scanning of four 10 x 10 x 10 mm cubes on the build platform using one of the 100 kHz pyrometers.

AlSi10Mg powder was used for the fabrication. The color-coded bar shows the mV readings from the thermocouple detector that was used to create the pseudo-temperature plots.

and the other one behind the laser spot for a qualitative measurement of the thermal gradient. A representative image showing the capability of the pyrometer measurements is presented in Figure 3.3. The colors in the plot are an indication of intensities of the infrared radiation within the measuring range of the Kleiber KG Series 740 – LO-100 kHz pyrometers i.e. 1580 to 1800 nm. To obtain the accurate absolute temperature, information of emissivity is necessary. Emissivity of the metal changes with wavelength and temperature due to their non-gray body radiation nature.

Emissivity could also vary with powder particle size and morphology. Application of multi-color and spectro-pyrometers could be a viable option for accurate surface temperature measurement in powder bed fusion additive manufacturing.

3.2 Description of Pyrometer Experiments

3.2.1 Materials

To study the emissivity variation of different metal powders, a Whipmix Pro 200 (Whip Mix Corp., Louisville, KY, USA) dental furnace was used to heat the sample powders contained in a quartz crucible (part # 319T050, Quartz Sci. Inc., OH, USA) under argon environment. Four different metal powders, namely copper (Cu), Ti6Al4V with two different size distributions and morphologies, AlSi10Mg, and aluminum 6061 alloy (AA6061) were tested. Table 3.2 shows the list of powder materials used for the experiments and their specifications. Information on size distribution is supplier provided and based on intended technology of application. Corresponding measured properties for size distribution and morphology will be shown later in the results section.

3.2.2 Whipmix Pro 200 furnace

Whipmix Pro 200 (Whip Mix Corp., Louisville, KY, USA) is a resistive heating furnace with a heating chamber with the following dimensions, 3 3/4 W x 2 1/2 H x 3 3/4 D in inches. The

Table 3.2 Supplier provided specification of the metal powders under study

Material	Supplier provided specifications		
	Morphology	Fabrication method	Size distribution (Technology grade)
AlSi10Mg	Spherical with satellites	Gas atomization	20-63 μm (LPBF grade)
Ti6Al4V	Spherical with satellites	Gas atomization	20-63 μm (LPBF grade)
Ti6Al4V	Spherical with satellites	Gas atomization	EBM grade
Ti6Al4V	Angular shape	Hydride dihydride (HDH)	Powder metallurgy and metal additive applications
Cu	Spherical and irregular with satellites	Gas atomized	EBM grade

heating element surrounds the cylindrical heating space while being wound by quartz tubing. The furnace is controlled by a factory installed E-type thermocouple E-type using a feedback control loop. In its unmodified form, the furnace would facilitate vacuum and argon environments in different settings. Single and two stage operation modes are available where in single stage mode, the heating chamber could be held in a single temperature before the cooldown step begins. In

two stage modes, two different hold temperatures could be availed. A graphic description of the available heating cycles are shown in the Figure 3.4.

3.2.3 Modified Whipmix Pro 200 furnace

Several modifications were performed on the original furnace to gain optical and other

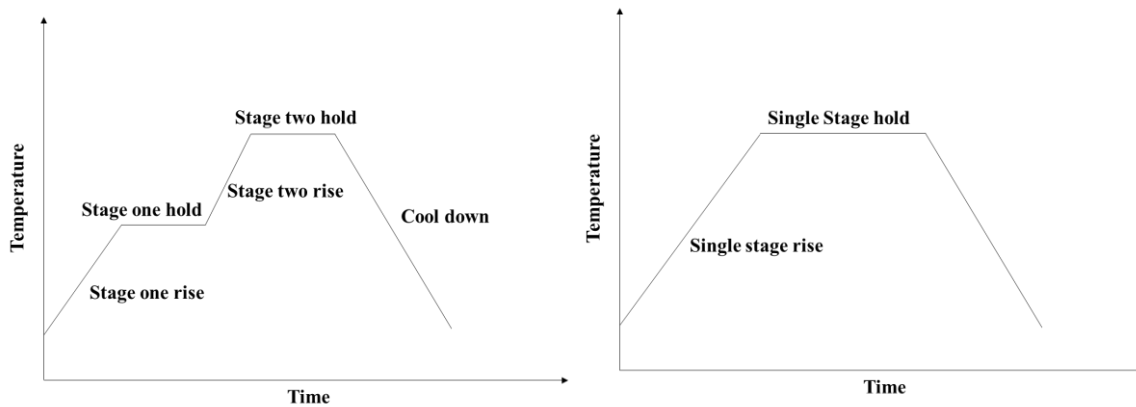
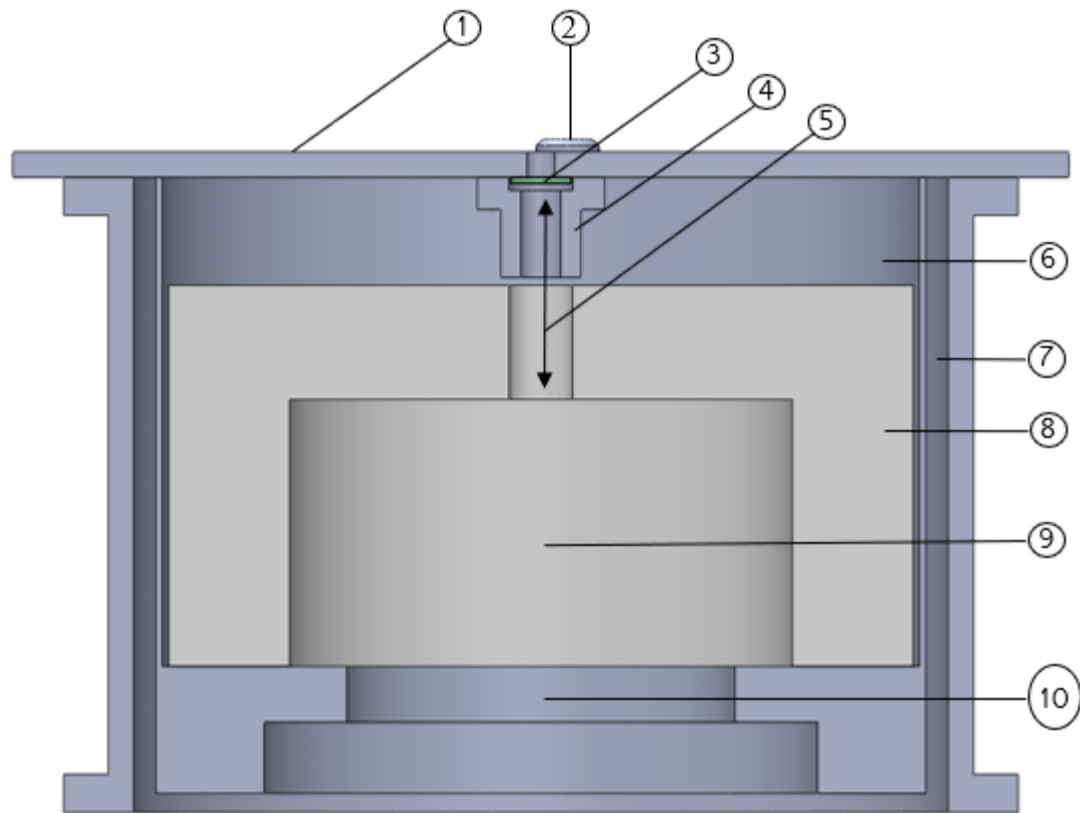


Figure 3.4 Single and dual stage operation of the Whipmix Pro 200 furnace temperature measuring access to the furnace's muffled chamber. Optical access was necessary for

measuring the radiation spectrum from the heated object using the SpectroPyrometer (FAR



- | | |
|---|-------------------------------------|
| 1. Metal lid | 6. Fiber insulation |
| 2. Thermocouple port | 7. Air gap |
| 3. Quartz window | 8. Ceramic foam insulation |
| 4. Metal flange for holding quartz window | 9. Heating chamber |
| 5. Viewing port | 10. Ceramic platform/ sample holder |

Figure 3.5 Cross section of the modified Whipmix Pro 200 furnace

Associates, OH, USA) MW pyrometer system. A cross section view of the CAD model of the modified furnace is depicted in Figure 3.5. The metal lid (item 1) of the furnace was machined to create a viewing window and hold a thermocouple. As shown in Figure 3.5, the cylindrical heating

space (item 9) of the furnace was immediately surrounded by factory installed ceramic foam insulation (item 8) held by a metal shell (not shown in CAD), an air gap, and an outer metal shell, respectively. The gap between the top lid (item 1) and ceramic foam insulation (item 8) was filled with ceramic blended fiber insulation (part # 23AR52, Grainger, USA). A metal flange with step was inserted after cutting a hole through the ceramic fiber and foam insulation. The flange was

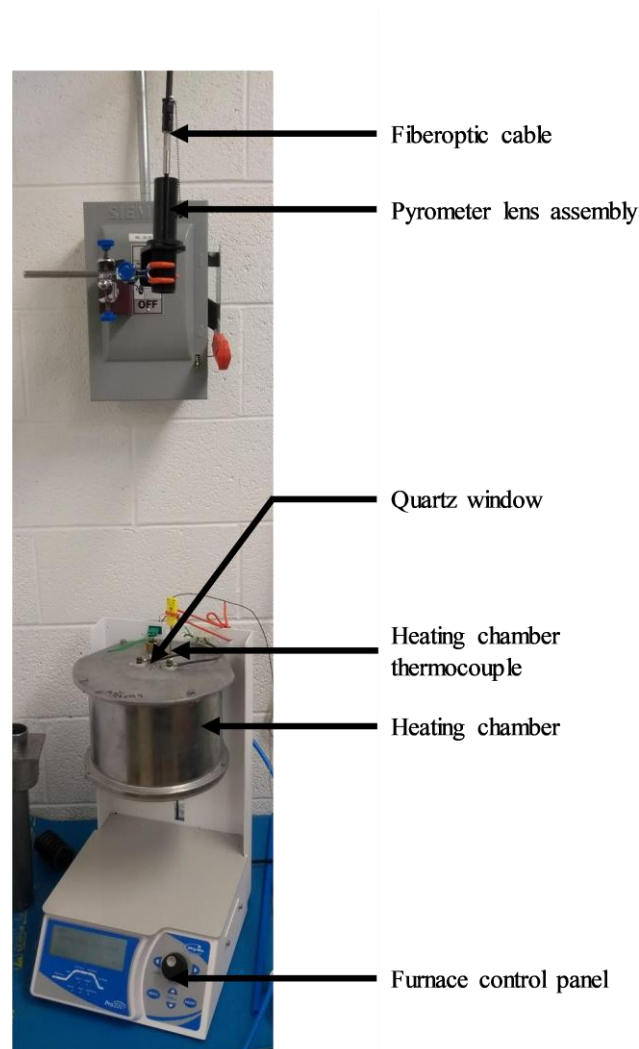


Figure 3.6 Modified Whipmix Pro 200 furnace with pyrometer assembly attached to the top lid by means of sealing socket head screws (part # 95198A415, McMaster-Carr, USA). The quartz glass (part # 210031, Quartz Sci. Inc., OH, USA) was placed in the stepped

space after being sandwiched by two high temperature silicone O-rings (part # 1283N53, McMaster-Carr, USA) for better sealing of the furnace chamber and protection of the glass. Picture of the set-up is shown in Figure 3.6. Some closer views of the modifications made to the furnace were given in Figure 3.7.

The unmodified furnace had an E-type thermocouple inserted in the chamber by the manufacturer for control purposes, such as maintaining temperature set points, heating and cooling rates, etc. However, the furnace firmware had no facility of recording the data from the furnace's thermocouple for analysis at a later time. To obtain temperature data from a measuring device other than the spectro-pyrometer, a second k-type thermocouple was inserted using a vented 1/8" NPT high temperature compatible gas tight pass-through. Location of the thermocouples can be

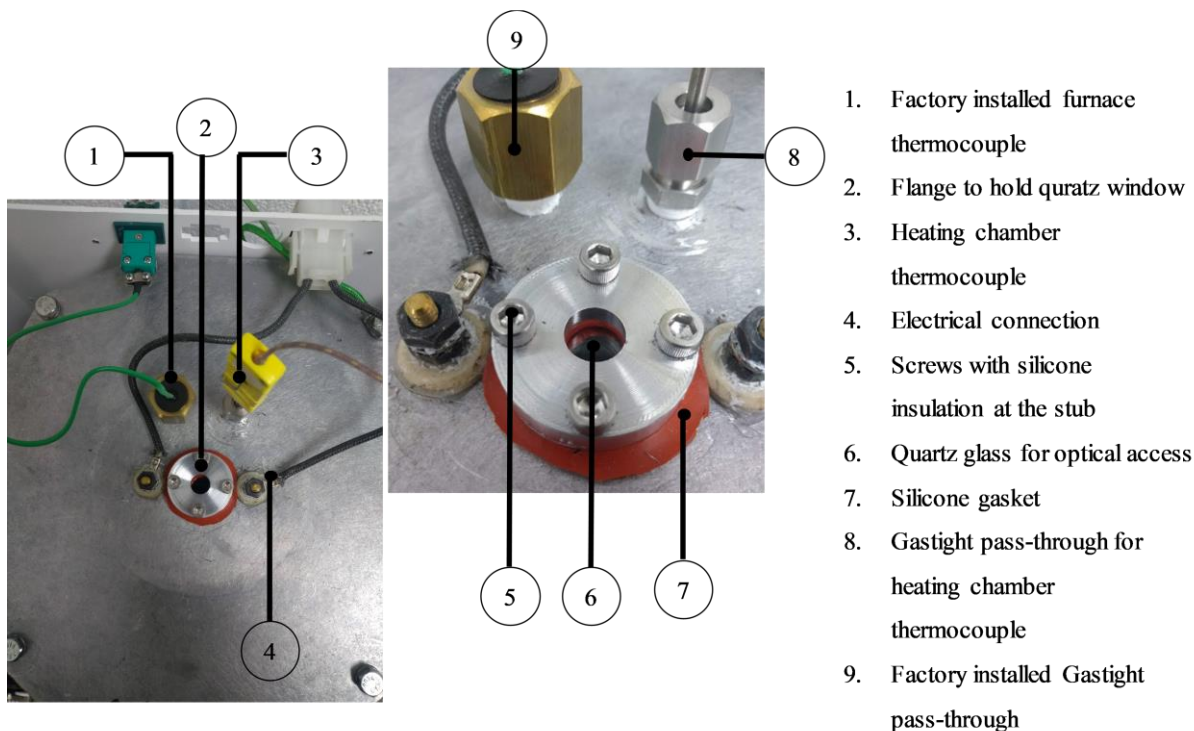


Figure 3.7 A top view of part of the modifications made to the Whipmix Pro 200 furnace.

The modified top window of the furnace is shown in the picture and a closer view is presented in the inset

observed from Figure 3.8. Part number and product identifier for the compression fitting are 311210-001 and MPG-125-A-G (Conax Technologies, Buffalo NY, USA), respectively. The thermocouple probe had a stainless-steel sheathing with 1/8" in diameter.

Inside views of the modified furnace are provided in Figure 3.8.

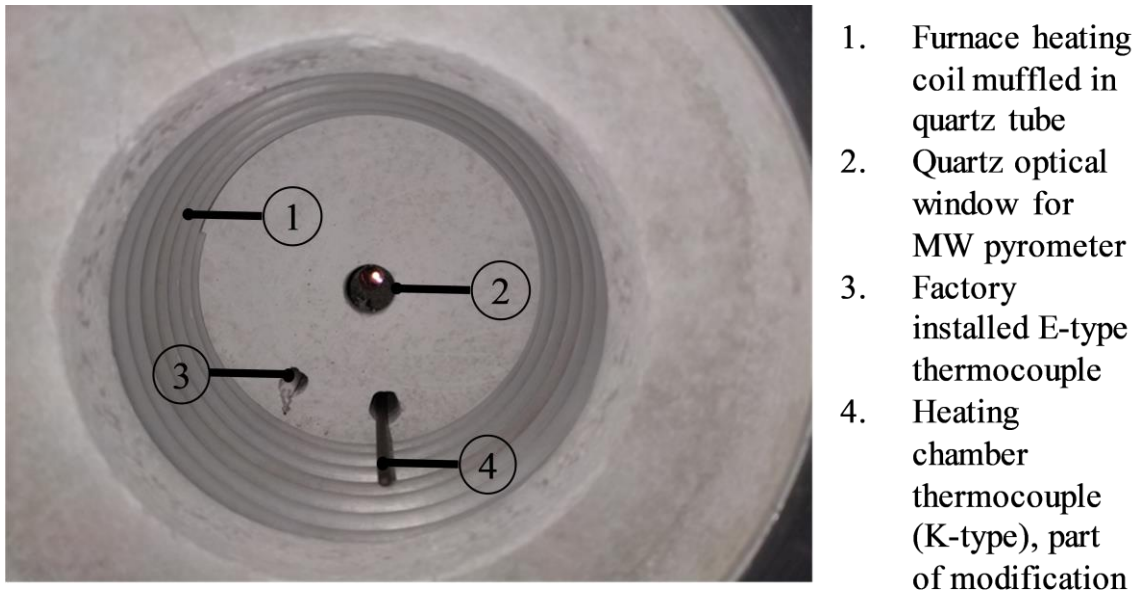
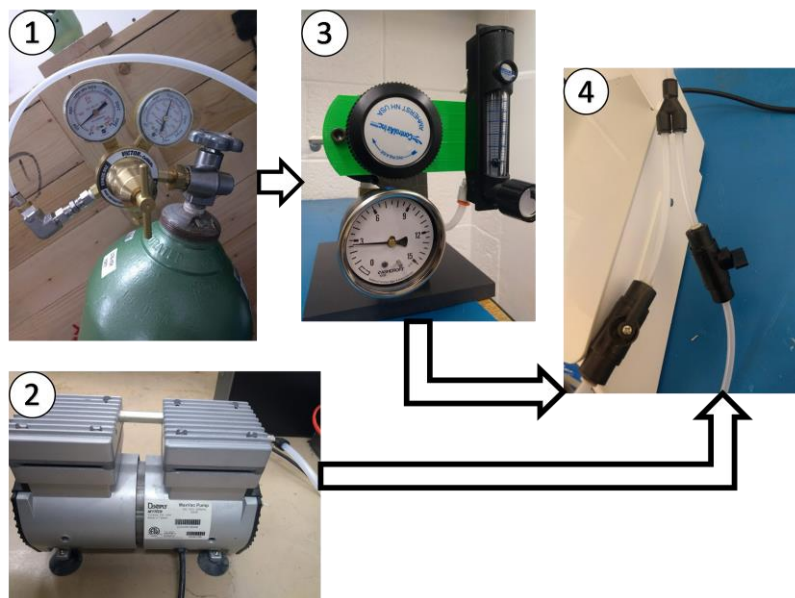


Figure 3.8 Picture of the interior of the modified furnace. Heating coil, the quartz viewing port for providing optical access to the MW pyrometer and the thermocouples are visible

Figure 3.9 shows the argon gas flow arrangements to maintain inert atmosphere



1. Argon supply tank with pressure gages 2. Vacuum pump 3. Argon pressure and flow controller for furnace 4. Argon flow and vacuum path

Figure 3.9 To maintain inert gas atmosphere inside the furnace argon was continuously

introduced inside the furnace chamber. Before purging with argon, the chamber would be vacuumed at 200 °C

inside the furnace. Ultra-high-purity (UHP) grade argon in T-type tank (Syoxsa, El Paso, TX, USA) was connected to the heating chamber of the furnace through a single scale pressure gauge (4003K71, McMaster-Carr, USA), impact-resistant panel-mount flowmeters for Air (5079K67, McMaster-Carr, USA), and high-flow precision compressed air regulator (1888K1, McMaster-Carr, USA). The flow was maintained at a pressure of 3 psi and a flow rate of 20 cubic feet per hour. The pressure was chosen to be 3 psi to maintain a positive pressure and remove oxygen from the chamber. Before continuously purging with argon, the heating chamber was vacuumed using a vacuum pump, 100-120 V MaxVac Pump (part # 9494198, model # DP-120H/120V, Dentsply

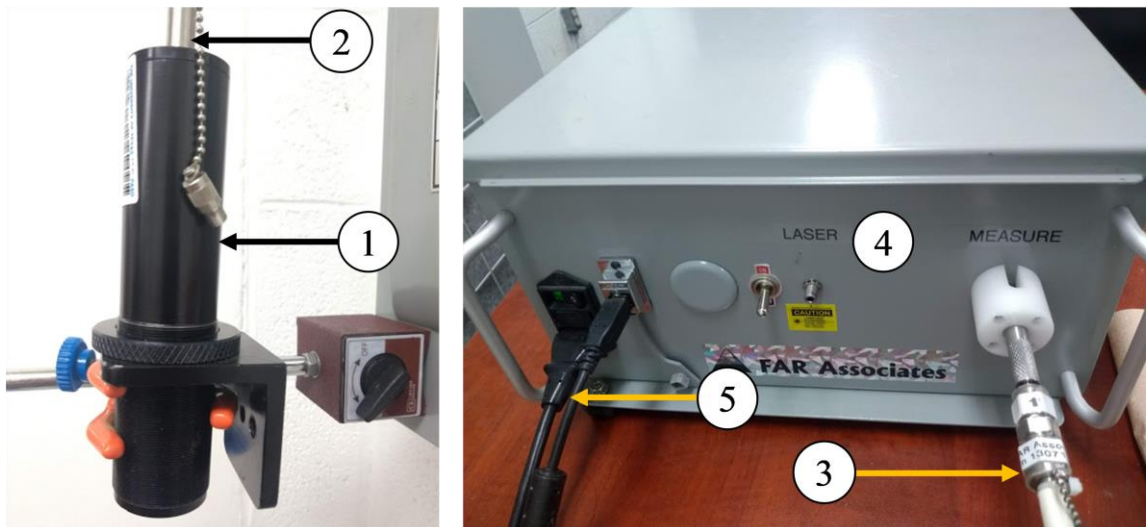
Neytech, CA, USA) and subsequently back filled with argon for three times in sessions of 20 minutes.

3.3 Measuring Devices

3.3.1 Multi-wavelength or Spectro-Pyrometer

A SpectroPyrometer (FAR Associates, Macedonia, OH, USA) multiwavelength (MW) pyrometer system was used for temperature measurement of the powder specimen heated inside the modified furnace. The SpectroPyrometer could measure the temperature of non-grey targets without requiring prior information of emissivity and provided emissivity information instead. Detailed description of the multi-wavelength or spectro-pyrometers is presented in Chapter 4 dedicated for pyrometry. Basic operational introduction specific to the instrument could be found in the operator's manual [57].

The pyrometer system consisted of an achromatic lens, a fiber optic cable, a spectroscope, and Windows 2000 operating system enhanced computer. Role of the achromatic lens was to limit the aberrations of the incoming radiation and focus the radiation of different wavelengths on the same focal plane to ensure minimum transmission loss through the fiber optic cable. The pyrometer had a green illumination laser that indicated the size of the measuring spot. Basically, the temperature output provided by the MW pyrometer was an average of the temperature within



1. MW pyrometer lens (2 and 3). Fiberoptic cable 4. Spectral analyzer of MW pyrometer 5. Electrical connections for power and data transfer to computer

Figure 3.10 Different components of the FMPI SpectroPyrometer (FAR Associate, OH, USA)

MW pyrometer system

the measuring spot. Therefore, if the target is smaller in size than the measuring spot, the temperature measurement would be wrong. The illumination laser was integrated in the spectroscopy's box and would be transmitted through the same fiber optic for aiming purpose.

3.3.2 Thermocouple Data Acquisition System

A stainless-steel sheathed k-type thermocouple probe with a diameter of 1/8'' was used for

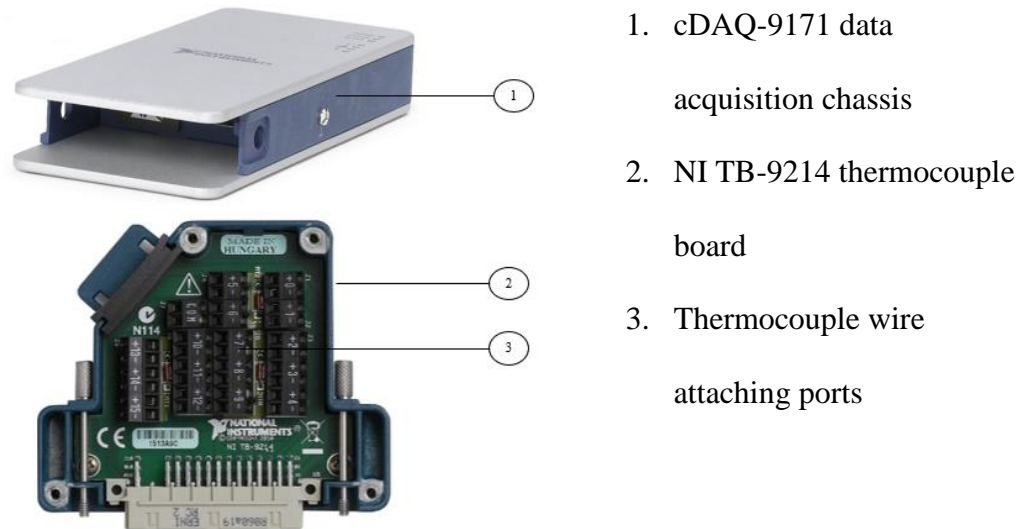


Figure 3.11 Different components of the thermocouple data acquisition system used in the current study

measuring and recoding the temperature inside the furnace. A data acquisition chassis, cDAQ-9171, Part Number: 781425-01 (National Instruments, Austin, TX, USA) was used in series with a NI TB-9214 (National Instruments, Austin, TX, USA) 16 channel thermocouple board. Role of the data acquisition chassis is to control the timing, synchronization and data transfer between the thermocouple input device and external host, in this case a computer. A software interface built using LabVIEW (National Instruments, Austin, TX, USA) and NI-DAQmx driver was used for data transfer from the cDAQ-9171 to the computer. Pictures of these parts are shown in Figure3.11.

3.4 In Situ Off Line Monitoring Windows

Two of the AconityONE windows, the top laser window and the side window were modified and fitted with quartz (Quartz Scientific Inc., OH, USA) and ZnSe (Edmund Optics, NJ, USA) windows. Images of the actual setup and CAD are shown in Figure 3.12 and Figure 3.13,

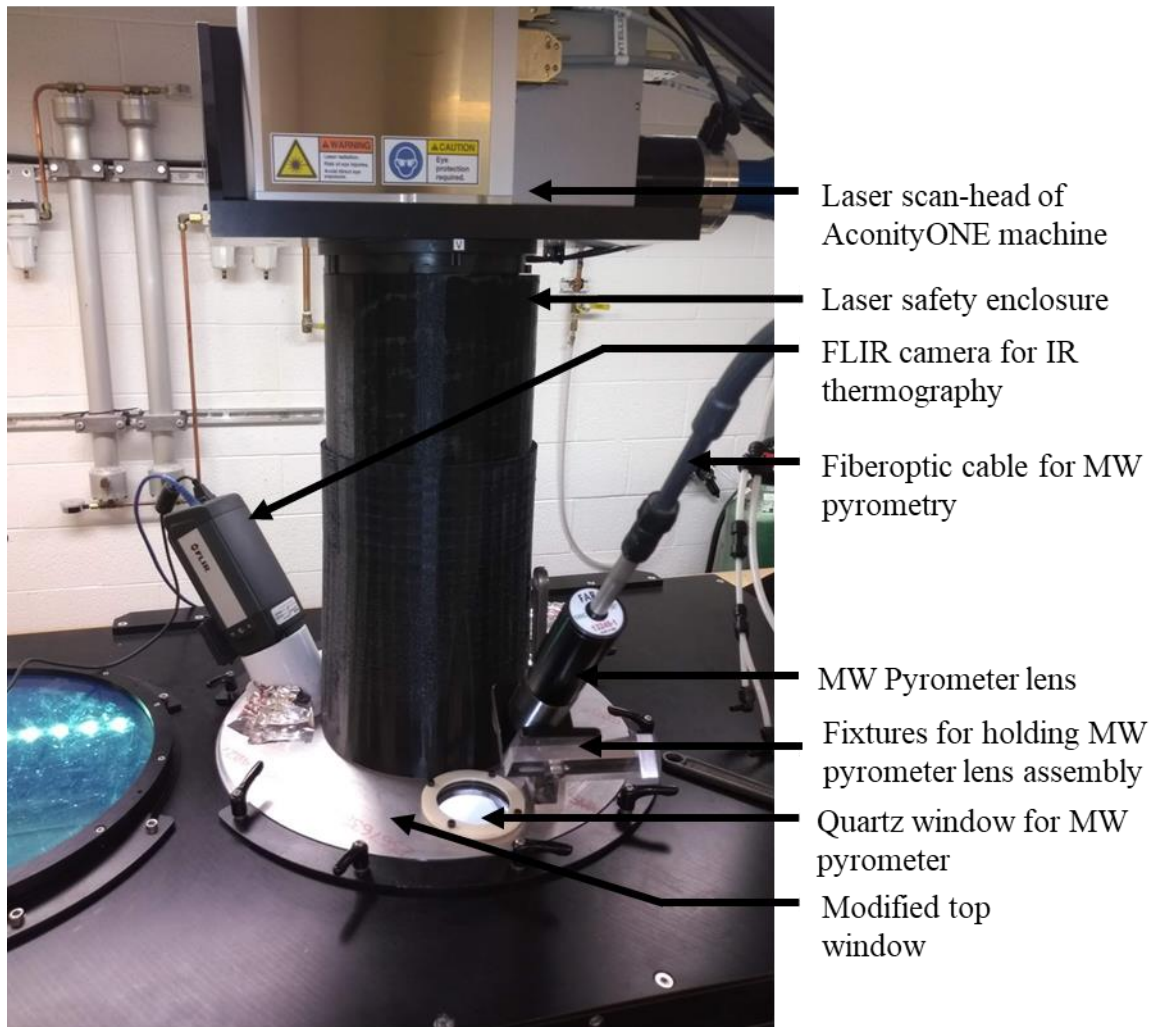


Figure 3.12 The top window of AconityONE after modification to incorporate MW pyrometer and an IR camera for in situ monitoring of the build. The original laser window of the AconityONE machine was replaced with this modified window respectively.

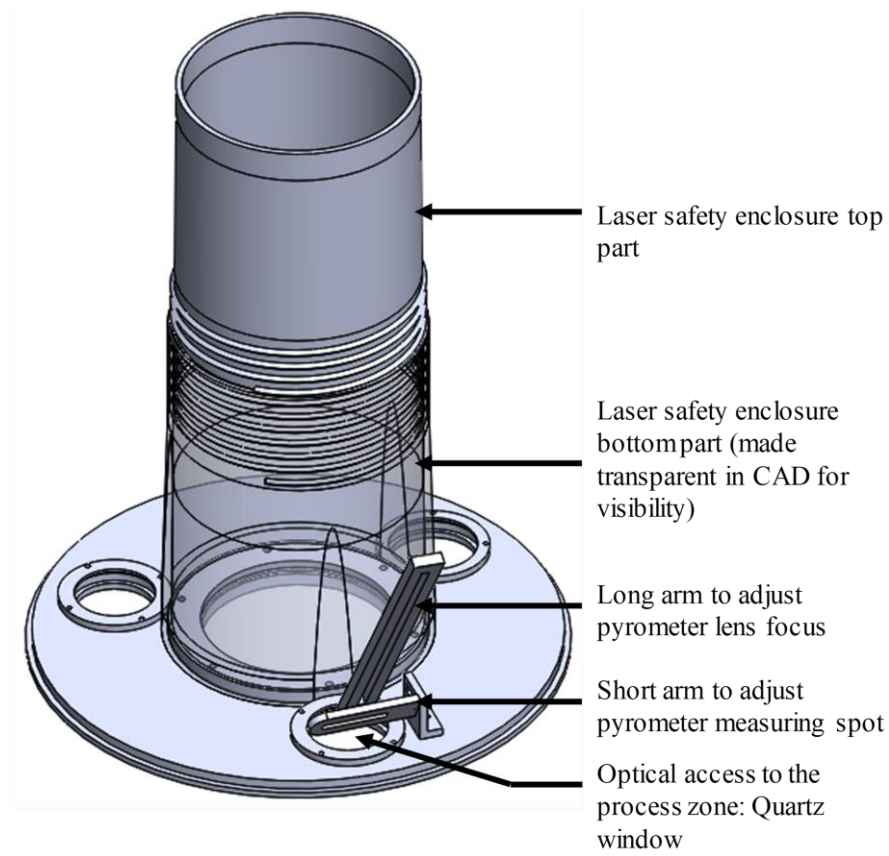


Figure 3.13 CAD model of the modified top window with the laser enclosure bottom part of which was made transparent (only in CAD model) for better visual. The transparent laser enclosure gives visual to the reduce size laser processing window

The side window of the AconityONE system was also modified for *in situ* monitoring using

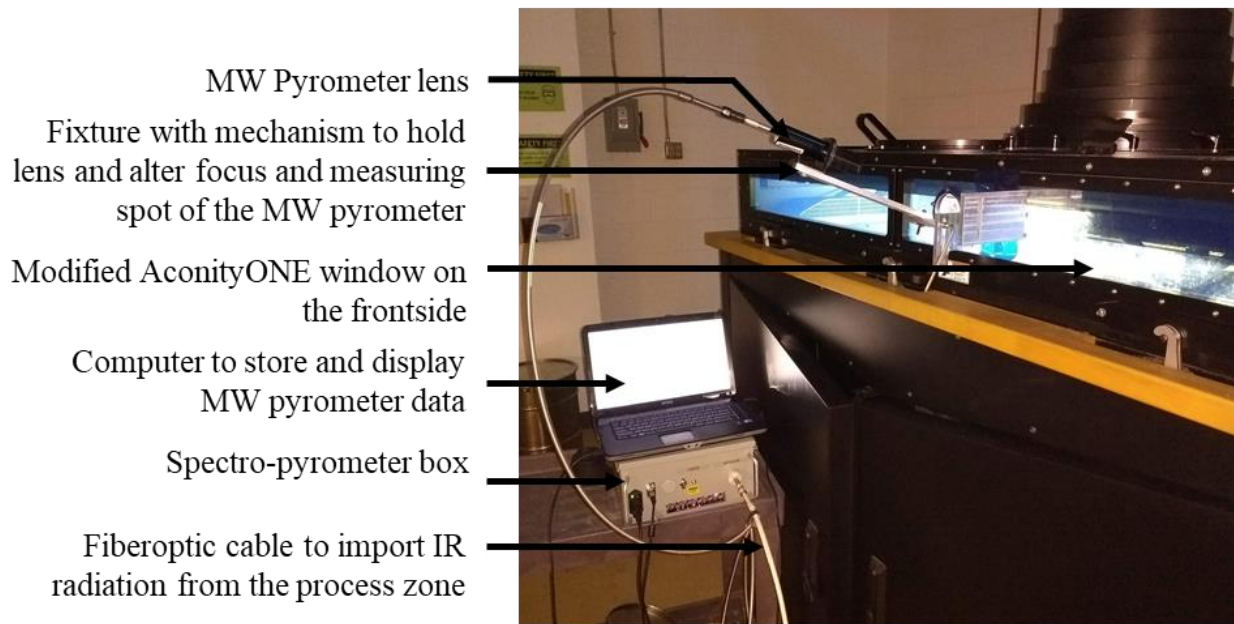


Figure 3.10 *In situ* monitoring setup including MW pyrometer mounted to the side window of AconityONE machine. The spectro-pyrometer box contains the means for dividing the incoming radiation in with a spectral resolution of close to 1 nm MW pyrometry. The actual setup and the CAD models are shown in Figure 3.14 and Figure 3.15, respectively. The CAD model in Figure 3.11 depicts the complete model when both the top and the front window would be in operation for the same build; however, this combination of set up was not experimented with for the current thesis.

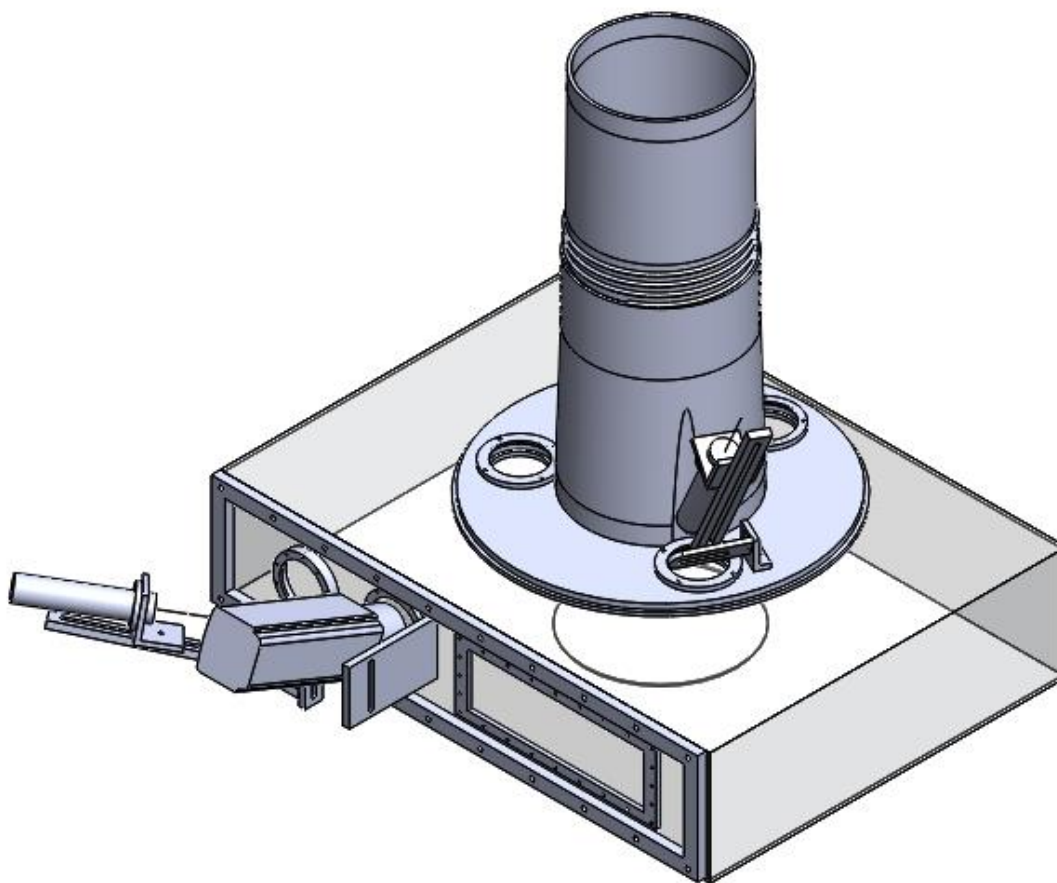


Figure 3.15 An inclusive CAD of *in situ* monitoring set up where both the front and top monitoring windows are shown. The components were identified in the previous Figures

3.5 Pyrometer Data Analysis

The MW pyrometer instrument used for the current research was developed by FAR Associates (Ohio, USA). The fundamentals of the MW pyrometer technology are presented in Chapter 4 along with brief description of some other type of pyrometers. According to the author, MW pyrometry, the one that is used in this study, is an extension of the spectroscopy/spectrophotometry technique that is widely used in fields such as physical chemistry

for elemental analysis of different chemical compounds, in food and drug industry for quality control, etc. Basically, the principle of unique radiation (emission or absorption of electromagnetic wave of different wavelengths) characteristics of any object at a temperature above absolute zero leaves a thermal signature which, if detected effectively, could be related to the absolute thermomechanical state of the target at the time of radiation.

The FMPI SpectroPyrometer (FAR Associates, OH, USA) would collect intensity data in arbitrary units according to factory calibration for the wavelength range of 850 nm to 1650 nm. The minimum data acquisition time of the instrument is 10 ms (i.e. 10^{-5} s). These data would then be processed using a patented algorithm [58] to output a temperature, tolerance, and emissivity value. An in-house methodology based on the ratio temperature calculation from several wavelengths was tested on the intensity - wavelength data stored in the instrument. The method adopted for calculating temperature from the raw data is explained below in steps along with the MATLAB[®] script used for calculation. A demonstration of the calculation using this algorithm is presented in Chapter 6. The potential use of this algorithm could be the development of an accurate surface temperature measurement equipment dedicated for metal AM machines.

The algorithm could be summed up in five steps; such as,

- i) importing the raw data files with .dat extensions from the local computer that was connected with the MW pyrometer
- ii) selecting the columns containing the wavelengths and intensities (these are columns 1 and 4 in the .dat files)
- iii) fitting a polynomial curve to the imported intensity data
- iv) calculating ratio temperatures for wavelength and intensity pairs from the fitted polynomial by applying Planck's law

- v) taking average of the ratio temperatures as consensus temperature

The MATLAB[®] scripts and functions used for the analysis is given in the appendix.

Chapter 4: Pyrometry

In the previous chapters of this thesis report, the importance of temperature measurement and associated difficulties in measuring accurate temperature as a state property were discussed from the viewpoint of application in laser powder bed fusion (LPBF) category of additive manufacturing (AM) processes. Due to the non-contact nature of pyrometric method of temperature measurement, this technique is well suited for AM processes where attaching any probe in the processing zone would be difficult and disruptive for the process itself. To fully realize the potential of using pyrometers in AM process monitoring, a fundamental understanding of this scientific technique and relevant instruments would be necessary. The current chapter starts with a brief introduction and classification of pyrometers and continues to describe different type of pyrometers, provides description of different pyrometer components and sensors, and discuss some of the issues in pyrometry of metals.

4.1 Necessity of Non-contact Temperature Measurement in Additive Manufacturing

Pyrometers are non-contact temperature measurement devices. Non-contact temperature measurement is of great importance to the processes that require very high purity of the process environment, and hence disallow any probe to be inserted in the location of measurement. Alteration of heat and mass transfer due to the presence of any measuring probe also calls for non-contact temperature measurement. In addition, the processes involving fast thermodynamic change, particularly phase change compounded with high heating and cooling rate [59] would require non-contact devices with a fast response time. Laser powder bed fusion technology (LPBF) resembles welding in many different aspects such as both have moving heat source for energy input, melting of metallic materials occur in both the cases in a continuous bead, etc. Weld pool temperature dictates the mass and heat transfer within the puddle, and accurate temperature measurement is essential to ensure the shape and integrity of the welding. With thermal gradients as high as 1000 K/cm [60] compounded with a moving heat source, the use of thermocouples and

other contact based temperature measuring devices would not be suitable in welding. Like welding processes, in LPBF very fast thermodynamic changes occur, and the challenges encountered in welding regarding temperature measurements persist with a more complex nature as described earlier in section 2.3. Therefore, a LPBF technology would benefit from the development and application of non-contact temperature techniques, devices, and algorithms for measuring the true surface temperature of the part being fabricated for quality assurance.

4.2 Introduction to Pyrometry

The word pyrometer is derived from the combination of Greek words, such as *pyro* - meaning fire, and *meter*- meaning to measure. The remote sensing nature of the instrument makes it suitable for measuring temperature of objects that are not easily or safely accessible or the process, the temperature of which is being measured, is vulnerable to interaction with external entities meant for temperature measurements such as, thermocouples, RTDs, etc. Pyrometers are also known as “radiation thermometers” since, in principle, pyrometers operate using the electromagnetic radiation of wavelengths within 0.4 to 20 μm that includes visible and infrared (IR) radiation as shown in Figure 4.1 [61]

Pyrometers are a broad class of instruments that could be distinguished by spectral sensitivity and method of operation as depicted in Figure 4.2 [62]. Manually operated pyrometers involve human operator where human eyes function as detectors. The automatic pyrometers provide temperature reading based on the calibration and algorithm programmed in the device. A more detailed discussion of how different pyrometers work follows.

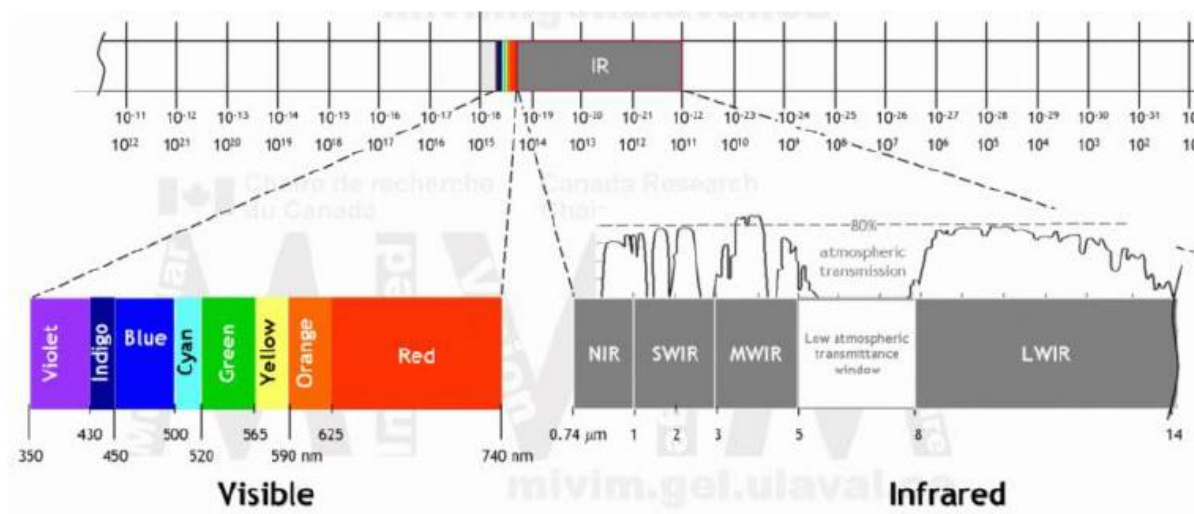


Figure 4.1 Electromagnetic spectrum showing the visible and IR radiation ranges that are usually utilized in pyrometry [61]

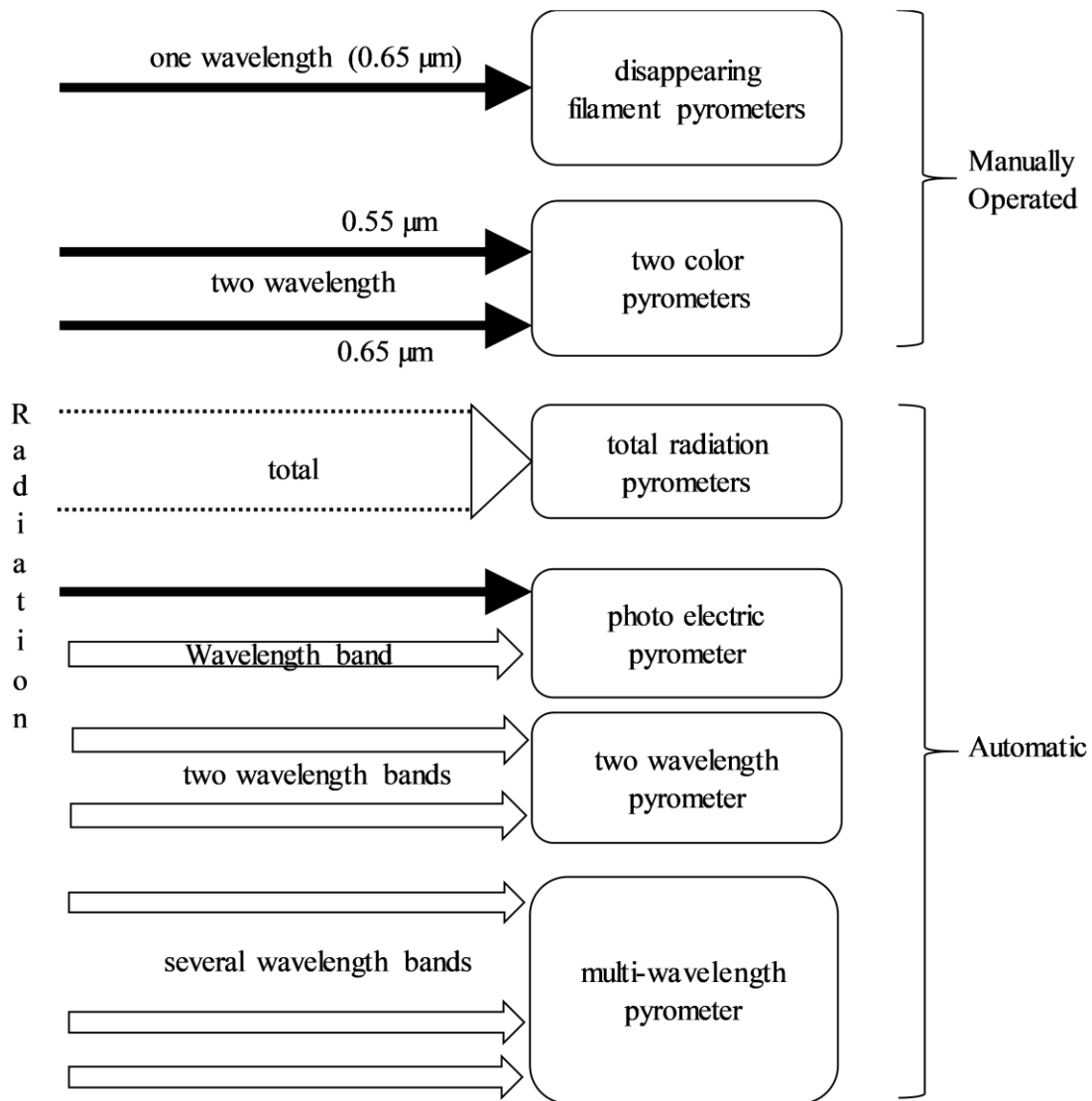


Figure 4.2 Classification of pyrometers based on spectral response and method of operation [62]

4.3 Manually Operated Pyrometers

4.3.1 Disappearing Filament Pyrometer

In disappearing filament pyrometers, the radiance of the target object is compared to that of a known object, usually a tungsten filament calibrated against the radiance of a blackbody. Current through the filament is constantly adjusted to achieve such radiance of the filament that it disappears from the view point when observed through a red filter. The red filter enables the pyrometer to work with a wavelength of $0.65\ \mu\text{m}$ and corresponding color which is visible to the human eye and yields a favorable spectral radiant intensity. Disappearing pyrometers have a lower detection limit of $700\ ^\circ\text{C}$ which is imposed by the limitation of human eye that could only detect comparatively long wavelengths in the visible range.

The mathematics of disappearing filament pyrometer is founded on Planck's equation [63] and Wien's approximation of the Planck's equation [64]. Before the derivation of the scaling equation for disappearing filament pyrometers, understanding of some of the fundamental radiometric terms is necessary.

Any given object that has a temperature beyond absolute zero, radiates energy in the form of infrared (IR) electromagnetic radiation. Such electromagnetic energy (E) radiated per unit time is known as 'radiant flux (Φ)' and measured using watts, W. Radiant flux in any given direction per unit of solid angle (θ) is known as 'radiant intensity (W)' measured using the unit W/sr . Spectral radiance L_λ is defined as the radiant flux density emanating from a surface per unit solid angle per unit wavelength and has the unit $\frac{\text{W}}{\text{m}^2\text{sr}^{-1}\mu\text{m}^{-1}}$. Spectral radiant intensity, W_λ is defined as the radiant flux emanating from a surface per unit solid angle per unit of wavelength.

Spectral radiance is given by Planck's equation in the following manner,

$$\text{Original Planck's equation, } W_{o,\lambda} = c_1 \varepsilon_\lambda \lambda^{-5} \left(\frac{1}{e^{\frac{c_2}{\lambda T_t}} - 1} \right) \quad (4.1.a)$$

Following Wien's approximation of Planck's equation,

$$W_{o,\lambda} = c_1 \varepsilon_\lambda \lambda^{-5} e^{-\frac{c_2}{\lambda T_t}} \quad (4.1.b)$$

$$L_{o,\lambda} = C c_1 \varepsilon_\lambda \lambda^{-5} e^{-\frac{c_2}{\lambda T_t}} \quad (4.2)$$

For a blackbody, given that a red filter has the spectral transmissivity of τ_λ , and operator's eye has a spectral sensitivity of V_λ , then the brightness felt by the operator's eye will be given by,

$$L'_{o,\lambda} = C c_1 V_\lambda \tau_\lambda \varepsilon_\lambda \lambda^{-5} e^{-\frac{c_2}{\lambda T_t}} \quad (4.3)$$

Similarly, for the filament, with a spectral emissivity of $\varepsilon_{f\lambda}$, the brightness experienced by the operator will be given by,

$$L''_{o,\lambda} = C c_1 V_\lambda \tau_\lambda \varepsilon_{f\lambda} \lambda^{-5} e^{-\frac{c_2}{\lambda T_t}} \quad (4.4)$$

The filament will disappear when the radiance of both the target and the filament are matched and therefore,

$$L'_{o,\lambda} = L''_{o,\lambda} \quad (4.5)$$

Despite the use of a red monochromatic filter, in practice the light that passes through the filter is not of a single wavelength, but a band of spectrum however narrow it might be. Therefore, all practical uses wavelength, λ is replaced with λ_e which is known as the equivalent wavelength. Replacing λ with λ_e , in the expressions for $L'_{o,\lambda}$ and $L''_{o,\lambda}$, the following is obtained,

$$\begin{aligned} e^{-\frac{c_2}{\lambda_e T_t}} &= \varepsilon_{f\lambda} \lambda^{-5} e^{-\frac{c_2}{\lambda_e T_t}} \\ \Rightarrow -\frac{c_2}{\lambda_e T_t} &= -\frac{c_2}{\lambda_e T_t} + \ln \varepsilon_{f\lambda_e} \end{aligned}$$

$$\Rightarrow \frac{1}{T_f} = \frac{1}{T_t} + \frac{\lambda_e}{c_2} \ln \varepsilon_{f\lambda_e} \quad (4.6)$$

that defines the basic equation for disappearing filament pyrometers where, T_f is the filament temperature, T_t is the target temperature, λ_e is the wavelength at which the pyrometer operates (usually $0.65 \pm 0.003 \mu\text{m}$ when red filters are used), c_2 is the second radiation constant with a value of $14.3 \times 10^3 \mu\text{m K}$, and $\varepsilon_{f\lambda_e}$ is the spectral emissivity of the filament at the wavelength λ_e .

To measure the temperature of a real object which is a non-black body for all practical purposes, the following modified equation is used that incorporates the emissivity of the target.

$$T_t = \frac{1}{\frac{1}{T_i} + \frac{\lambda_e}{c_2} \ln \varepsilon_{\lambda_e}} \quad (4.7)$$

where, ε_{λ_e} is the emissivity of the target at the wavelength λ_e .

Using a tungsten filament, temperature only up to 1400°C could be measured since tungsten would evaporate beyond this temperature. To extend the capacity of optical pyrometers to measure temperatures up to 3500°C grey filters are used that would incorporate a grey correction factor. An example of commercially available instrument such as the one mentioned above could be found here [65].

The current discussion intended to outline the basic principle of pyrometry. Such earlier techniques of pyrometry was intended for measuring steady state temperatures with setup that required human intervention and interpretation of the result. Clearly, single color and manually operated pyrometer would not be suitable for measuring temperature in a dynamic process such as LPBF. The following sections are dedicated to the discussion on improved

pyrometry techniques and identification of a technology that would serve the purpose of accurate temperature measurement in LPBF AM process.

4.3.2 Two-color Pyrometers

Two color pyrometry is founded on the incandescence phenomenon of materials. Incandescence is defined as the glowing of any solid or liquid body after heating beyond approximately 528 °C [66]. Two color pyrometry is independent of the requirement of an emissivity input to measure temperatures of black and grey bodies, since in black and grey bodies, emissivity is wavelength independent. However, in case of non-black and non-grey bodies the emissivity is wavelength dependent and therefore, would not be able to output a thermodynamic temperature directly.

In two color pyrometers, temperature is measured from the ratio of spectral radiant intensities as proposed by Forsythe [67]. A two-color pyrometer employs a pair of red (0.66 μm) and blue (0.47 μm), or red (0.66 μm) and green (0.55 μm) filters to observe the target. The filters are so adjusted that the target turns grey in the operator's eye. Then the temperature is directly read in the output according to calibration. To give an example, one of the early two-color pyrometers that used a two-color wedged filter could be mentioned. The wedge filter would give off a fixed amount of red when the amount of green could be varied. When looked at an object at thermal equilibrium, the operator would find a whitish-yellow point by adjusting the filter. Once the source temperature changed, the location of that point would also change and give a direct indication of temperature change [68].

The scale is established in two-color pyrometers by using the spectral radiant intensity of the target at the wavelengths of the filter, as given by Wien's approximation of Planck's equation.

$$W_{\lambda} = c_1 \varepsilon_{\lambda} \lambda^{-5} e^{-\frac{c_2}{\lambda T}} \quad (4.8)$$

Where, W_λ is the spectral radiant intensity at the wavelength λ . Since, emissivity is independent of wavelength for black and grey bodies, W_λ is related to thermodynamic temperature T , using the following equation,

$$\frac{W_{\lambda_1}}{W_{\lambda_2}} = Ae^{\frac{B}{T_i}} \quad (4.9)$$

where, $A = \left(\frac{\lambda_2}{\lambda_1}\right)^5$ and $B = c_2 \left(\frac{1}{\lambda_2} - \frac{1}{\lambda_1}\right)$ and could be considered constant for a given pair of filters.

When the temperature of non-grey body temperature is measured by two-color pyrometer, it would be called a color temperature (T_c), as defined by Ribaud [69], instead of accurate thermodynamic temperature (T_t) since emissivity changes with wavelengths in case of a non-grey body and the assumption that $\varepsilon_{\lambda_1} = \varepsilon_{\lambda_2}$ does not hold. After considering differences in emissivity for grey bodies, (T_c) and (T_t) were related in the following equation,

$$T_c = \left(\frac{1}{T_t} - \frac{\ln\left(\frac{\varepsilon_{\lambda_1}}{\varepsilon_{\lambda_2}}\right)}{c_2\left[\left(\frac{1}{\lambda_2} - \frac{1}{\lambda_1}\right)\right]} \right)^{-1} \quad (4.10)$$

Like manually operated single color pyrometers, the two-color pyrometers also require human intervention. Such shortcoming rendered this technology unsuitable for LPBF AM processes. In further discussion on the topic of pyrometry, automatic algorithm driven, and sensor dependent pyrometers will be considered for AM processes.

4.4 Automatic Pyrometers

Unlike manual pyrometers, automatic pyrometers do not require a human operator, instead a photo detector replaces human eye. An automatic pyrometer system consists of a

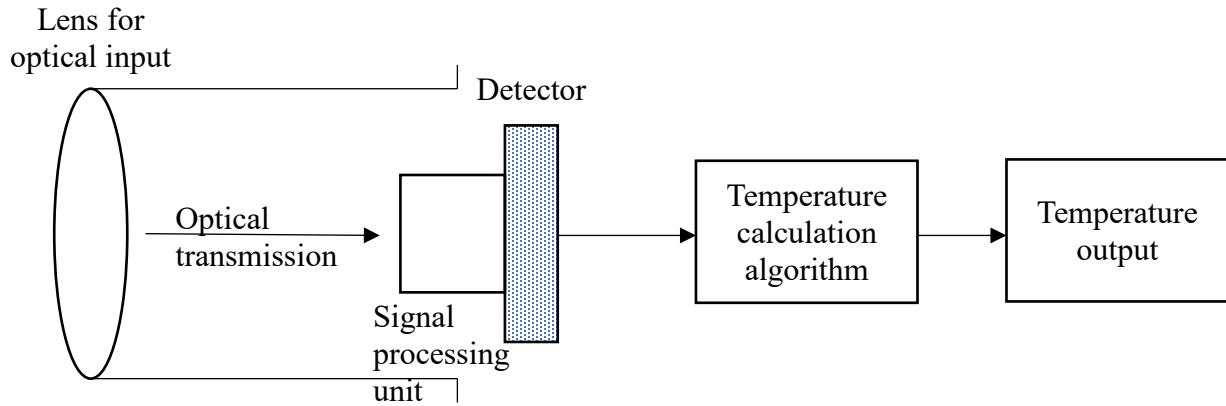


Figure 4.3 Main components of an automatic pyrometer

means of receiving optical or thermal radiation from the source, transmission optics, signal processing and detector unit, temperature calculation algorithm and a display unit as shown in the schematic in Figure 4.3.

4.4.1 Single Wavelength Pyrometers

Single wavelength pyrometers follow the general schematic of automatic pyrometers as shown in Figure 4.3 except with a much simpler calculation step. In single wavelength pyrometers filters are used in front of the detector that would allow only a selected energy wavelength be incident on the detectors. Single wavelength pyrometers are suitable for targets for which the emissivity does not vary with temperature, wavelength, surface morphology, etc. These pyrometers work based on equation (4.2.b) which is Wien's approximation of Planck's equation,

$$L_{o,\lambda} = Cc_1\varepsilon_\lambda\lambda^{-5}e^{-\frac{c_2}{\lambda T_t}}$$

where the left side of the equation is measured quantity (i.e. radiance of the target), C is an instrument constant, c_1 and c_2 are first and second Planck's constant, λ is the operating wavelength of the pyrometer, ε_λ is the emissivity of the target at the operating wavelength, and T_t is the temperature of the target in K. When all the other quantities are known, T_t could be calculated using equation (4.2).

4.4.2 Dual Wavelength Pyrometers

Two or dual wavelength pyrometers are sometimes referred to as automatic two-color

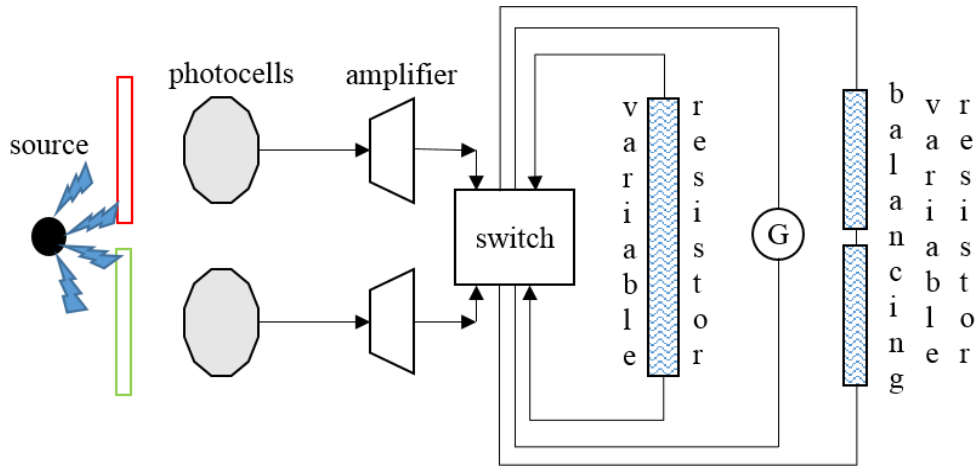


Figure 4.4 Schematic of a two-wavelength pyrometer circuit [68]

pyrometers because of the way the incident radiation is analyzed by means of photoelectric detectors instead of human eye. Operating principles and scale defining equations for two wavelength pyrometers follow from the two-color pyrometers. One of the earliest two wavelength pyrometers was described by H.W. Russel as shown in Figure 4.4 [68] where photocells were used as detectors, and vacuum tubes were used for amplification of the photoelectric current. Incident radiation would pass through red and green filters essentially at two monochromatic wavelengths

that could be detected in the photocells. Corresponding electrical circuit would then indicate and record the response to yield a ratio of the intensities of two different wavelengths. Temperature is indicated by using the value of such a ratio. More sophisticated electronics such as photodiodes instead of photocells are used nowadays [70].

Bach *et al.*[71] developed a pyrometer with 100 Hz frequency, 250 μm resolution for temperature measurement of particulate matters in captive fuel cells. The lower limit of temperature measurement was 300 °C. Two narrow band pass filters of wavelengths 3.1 and 4.5 μm were used. It was one of the earlier works with two-color pyrometers and photocells were used as photodetectors. A liquid nitrogen cooled indium antimonide cell was used as detector along with a mechanical amplifier contemporary to the era.

Muller et al. [72] developed a dual wavelength pyrometer that could measure temperature down to 300 °C with object's emissivity as low as 0.2. The pyrometer had an operating wavelength of 1.7 and 2.0 μm . Speed of the pyrometer was limited by speed of the amplifiers and data acquisition allowing a maximum resolution of a few microseconds. A spatial resolution of approximately 0.5 mm^2 was achieved. The pyrometer was intended for use in temperature measurements of metal chips during turning operation that continually varied in emissivity and had obstructed view by dirt due to the operational environment.

Dual wavelength pyrometers are often used with the argument that it provides accurate temperature of the target regardless of emissivity based on the underlying assumption that at the considered wavelengths, such as λ_1 and λ_2 the corresponding emissivity values, such as ε_{λ_1} and ε_{λ_2} follow the rule of $\frac{\varepsilon_{\lambda_1}}{\varepsilon_{\lambda_2}} - 1 = 0$ or *constant*. However, in practice, emissivity, ε is not a dependent on wavelength, λ only but it also depends strongly on surface morphology, target's material phase, temperature itself, etc. [73]. As discussed earlier, LPBF is a highly dynamic process where the

target is initially in powder form, then undergoes melting with laser interaction and solidifies back to bulk solid at the cooling rate of 10^{-5} °C/sec. Such dynamics could potentially upset the underlying assumption of dual wavelength pyrometry during *in situ* measurement in LPBF processes. Therefore, to accurately measure *in situ* temperature a in LPBF process, a pyrometry technique that employs radiance measurement at multiple energy wavelength and applies algorithm that not only provide a temperature output but also assess the correctness of the measurement would be required. In the following section, multiwavelength (MW) pyrometers, devices that potentially meets such requirement is described.

4.4.3. Multi Wavelength Pyrometers

As the name suggests, multiwavelength (MW) pyrometers acquire spectral intensity data at multiple wavelengths. Khan *et al.* extensively reviewed different MW pyrometer algorithm identifying them in two broad categories, such as interpolation based techniques, [60] and least square based techniques [74]. The errors associated with MW pyrometry was reviewed in detail by P.B. Coates [75]. A practical MW pyrometer was built and commercialized by R. Felice [76]. The SpectroPyrometer FMPI (FAR Associates, OH, USA) was the MW pyrometer used for the current study. The algorithm used in the instrument acquires spectral intensity data in arbitrary units according to factory calibration at a minimum of 250 different wavelengths in the range of 850 nm to 1650 nm. The data is then analyzed using a patented algorithm that provide a temperature output, a tolerance value that signifies the accuracy of the measurement and a real-time emissivity value of the target surface. As well as using the instrument's temperature measurements as coming out of a patented algorithm [77], a similar approach was adopted for calculating accurate surface temperature using spectral intensity data by the author of this thesis and the steps of calculation was described in the experimental section 3.5, a demonstration of the

calculation is given in section 6.3 and the corresponding MATLAB[®] scripts are given in the appendix B. The SpectroPyrometer (FAR Associates, OH, USA) MW pyrometer was used in different setups regarding the current research within the scope of this thesis and the results on metal powder emissivity measurements and *in situ* measurements are presented in Chapter 6: Results and Discussions.

4.4.4 Time Resolution of Different Ratio Pyrometers

Time resolution of pyrometer devices are limited by the speed and efficiency of the available detectors, signal amplifiers, and data acquisition systems. In Table 4.1, a summary of the time resolution reported for different type of ratio pyrometers was given. Works from the

Table 4.1 Time resolution of different ratio pyrometers

Type	Authors and year of publication	Time resolution
Radiation pyrometer	Giuseppe Ruffino, 1976	10^{-3} sec or less
Two-color pyrometer	Jorgensen <i>et al.</i> , 1985	10^{-4} sec
Six-color pyrometer	Hiernaut <i>et al.</i> , 1986	$< 10^{-3}$ sec
Single wavelength-spatial scanning pyrometer with array of detectors	Cezairliyan <i>et al.</i> , 1993	10^{-6} sec
Spectro-Pyrometer (250 wavelengths between 850 nm to 1650 nm)	Ralph Felice, 2002	10^{-5} sec minimum

following researchers were cited: G. Ruffino [78], Jorgensen *et al.* [79], Hiernaut *et al.* [80], Cezairliyan *et al.* [81], and Ralph Felice [76]. This comparison is not exhaustive but indicates that the capability of pyrometers in terms of response time had been increasing with the availability of

faster sensors and more computational power. Successful use of SpectroPyrometer [76] was shown in electron powder bed fusion (EPBF) technology by Cordero *et al.*[82] where the melt pool temperature following a high speed scanning using an electron beam was captured. EPBF process has similarity with LPBF process; therefore, use of the SpectroPyrometer in the current study was deemed viable and as mentioned above, measurements obtained by the instrument is shown in Chapter 5.

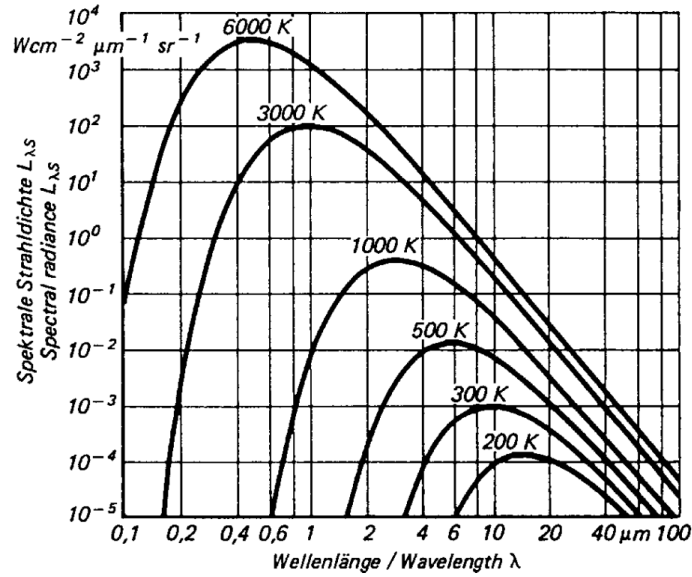
For the interested readers, background information on different types of transmission optics, detectors, and wavelength splitting techniques is included in section 4.5 and 4.6. If the reader is familiar with these topics, then sections 4.5 and 4.6 could be skipped. Section 4.7 discusses some of the issues with pyrometric measurement on metals.

4.5 Automatic Pyrometers Components

4.5.1 Transmission Optics

Optical path to the detector is a vital component of any pyrometer since the quality of received radiation would determine the accuracy of the measurement. Also, temperature limits of the measuring device depend heavily on the type of glass material used for making the lens. Usually, materials that have a distinguished opaqueness (transmissivity, $\tau = 0$) at beyond a specific wavelength range are used as transmission lenses and windows in pyrometers. It is evident from Planck's curves for blackbody radiation shown in Figure 4.5 (a) that longer wavelengths correspond to lower temperatures, and therefore pyrometers that work with low temperatures use the windows that allows the transmission of longer wavelengths. For example, KRS-5 is transparent to radiation within the wavelength of 0.5 to 36 μm enabling the material to be used in

(a)



(b)

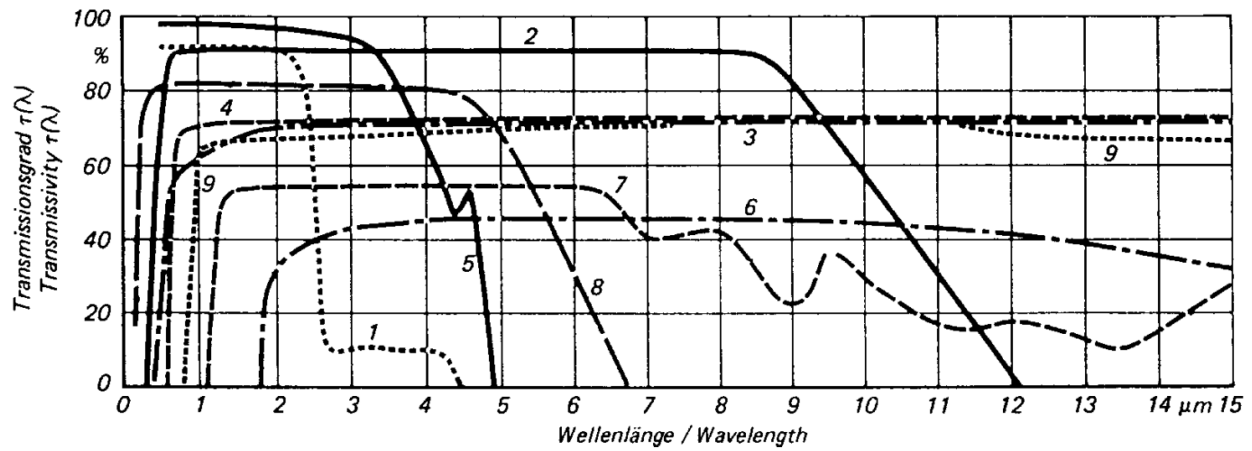


Figure 4.5 (a) Blackbody radiation characteristics based on temperature. (b) Transmittance of typical IR window [62]

- | | | |
|---------------------------|-----------------|--------------------------|
| 1- Optical glass | 4- KRS-5 | 7- Silicon |
| 2- Calcium fluoride (CaF) | 5- Quartz glass | 8- Lithium fluoride |
| 3- Zinc selenide (ZnSe) | 6- Germanium | 9- Chalcogenide glass IG |

pyrometers that could read temperature as low as -50°C . Transmissivity values of some of the typically used IR windows are shown in Figure 4.5 (b) along with the Planck's curve for blackbody

radiation [9]. For the setup used in the current study as described in Chapter 3, quartz and ZnSe windows were used for SpectroPyrometer and FLIR IR thermal camera, respectively.

The lenses used in pyrometers have well defined measuring spot at certain distances from

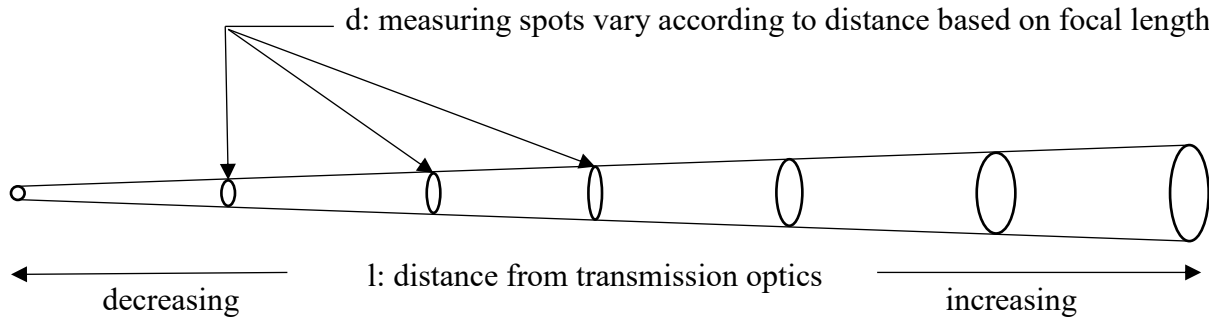


Figure 4.6 l/d designation of lenses used in pyrometry

the target as shown in Figure 4.6. Finding out and setting up the pyrometer at the correct distance to ensure the right measuring spot size could be critical to the accuracy of temperature measurement for targets that are small and highly transient in nature. The lenses are designated in the format $d \text{ (mm)}/l \text{ (m)}$ where 'd' is the measuring spot diameter at a measuring distance i.e. the distance between the lens and the target of 'l' m as illustrated in Figure 4.6.

4.5.2 Infrared Radiation (IR) Detectors

IR detectors are essentially sensors that receive the thermal radiation emitted from the

Table 4.2 Comparison of IR detector types (Rogalski *et al* [85].)

Detector type	Advantages	Disadvantages
Thermal	Light, rugged, reliable, and low cost Room temperature operation	Low detectivity at high frequency Slow response (ms order)
Photon		
Intrinsic IV–VI	Available low-gap materials Well studied	Poor mechanical Large permittivity
II–VI	Easy band-gap tailoring Well-developed theory and exp.	Non-uniformity over large area High cost in growth and
processing		
III–V mismatch	Multicolour detectors Good material and dopants	Heteroepitaxy with large lattice
	Advanced technology Possible monolithic integration	
Extrinsic operation	Very long wavelength operation Relatively simple technology	Extremely low temperature
Free carriers	Low-cost, high yields Large and close packed 2D arrays	Low quantum efficiency Low temperature operation
Quantum wells		
Type I	Matured material growth Good uniformity over large area Multicolour detectors	Low quantum efficiency Complicated design and growth
Type II growth	Low Auger recombination rate Easy wavelength control	Complicated design and Sensitive to the interfaces

source or target to be measured and converts it to an electrical signal. After calibration against a blackbody those electrical signals are assigned a temperature. A comparison of different types of

IR detectors is shown in Table 4.2 adopted from Rogalski *et al.*[85]. Based on operating principle, IR detectors could be categorized in two groups, namely,

- i) Thermal detectors
- ii) Photon sensitive quantum detectors/photodetectors/photodiodes

4.5.2 (i) Thermal Detectors

Thermal detectors actively heat up upon irradiation from the target. Such heating could indicate the target's temperature by change of electromotive force in case of thermopiles, resistance in case of bolometers, dielectric surface charge in case of pyroelectric detectors, etc. Since a thermal detector requires time to heat up actively to give off thermal electrons and hence a temperature reading, the response time is slower (in the scale of ms i.e 10^{-3} s instead of μ s i.e. 10^{-6} s for the case of photodetectors). From pyrometry point of view, the advantage of thermal detectors is in the fact that they are spectrally independent. The spectral independence removes some barriers in pyrometry such as the limitation in choosing optical transmission lines with specific wavelength window, low temperature cut-off imposed by the wavelength specific windows and detectors in case of photodetectors, etc. With widespread use of photon detectors, research and development of thermal detectors experienced a decline during nineties; but recent developments in use of thermal detectors in array configuration came with the promise of high quality images at a rate of 60 Hz in uncooled configuration [85].

Different types of thermal detectors are in use for applications in pyrometry such as, thermopiles, thermistors and metal bolometers, and pyroelectric detectors. Thermopiles are essentially an array of thermocouples that can have different configurations such as wire type, ribbon type, thin film, etc.

Bolometers are another type of thermal detector widely used in thermal imaging applications that use IR radiation for temperature measurement. Invention of bolometers is attributed to Samuel Langley [86], and the basic construction of a bolometer comprises of a thermal absorber and a thermal reservoir. The impinging IR radiation heats up the absorber which initially remains in equilibrium with the isothermal reservoir by means of conduction. Heating of the absorber raises the temperature and change in temperature is read out by a resistive thermometer.

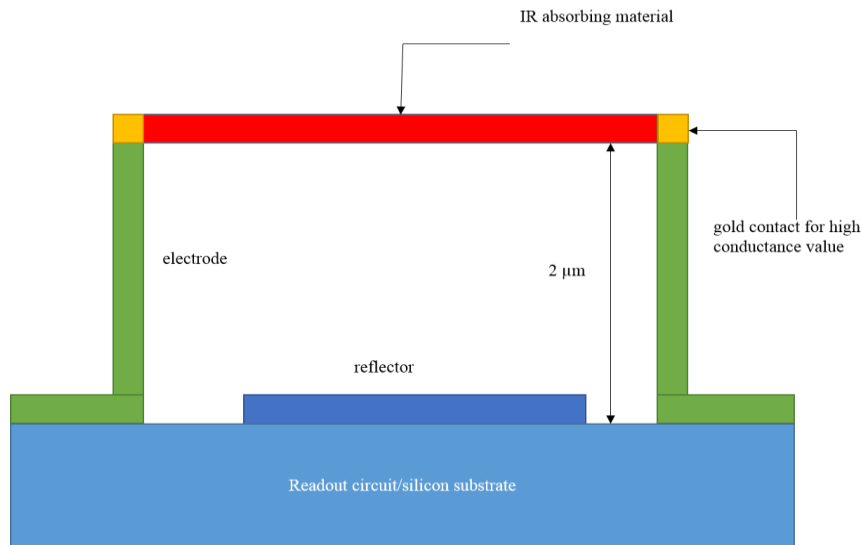


Figure 4.7 Basic construction of a micro-bolometer (Wikipedia)

Time constant of the bolometer is a function of the ratio between heat capacity of the absorber and the thermal conductance between the absorber and reservoir [87]. Microbolometer is a bolometer where the detectors are mostly constructed using amorphous silicon or vanadium oxide because of the ease of fabrication, and stability in application for a long time. Such attributes allow them to be used in thermal cameras. A schematic of microbolometer is shown in Figure 4.7.

Pyroelectric thermal detectors are a class of crystalline materials that are sensitive to temperature as manifested in a change of crystal structure. When the thermodynamic equilibrium of such material is disturbed by exposing them to IR radiation, surface charge is produced as a

result of spontaneous polarization and creates dipole moments, and hence, crystal structure change [88]. Despite their high sensitivity, such detectors are not commonly used because of the complexity in construction.

4.5.2 (ii) Photon Sensitive Quantum Detectors/Photodetectors/Photodiodes

Photo electric detectors are based on quantum photoelectric effect hypothesized by Max Planck when explaining the radiation from a blackbody [63]. The effect was later further explained by Albert Einstein using a mathematical model to address the particular phenomena of gas ionization due to ultraviolet radiation [89]. Einstein's explanation was corroborated by an earlier experiment conducted by Robert Millikan [90] that determined the minimum or quantized charge of an electron.

In photoelectric detectors, the incident radiation with a frequency beyond a threshold value would discharge electrons that could be amplified and related to the intensity of incident radiation at that frequency or wavelength. Figure shows a pulse-type detection system schematics and a

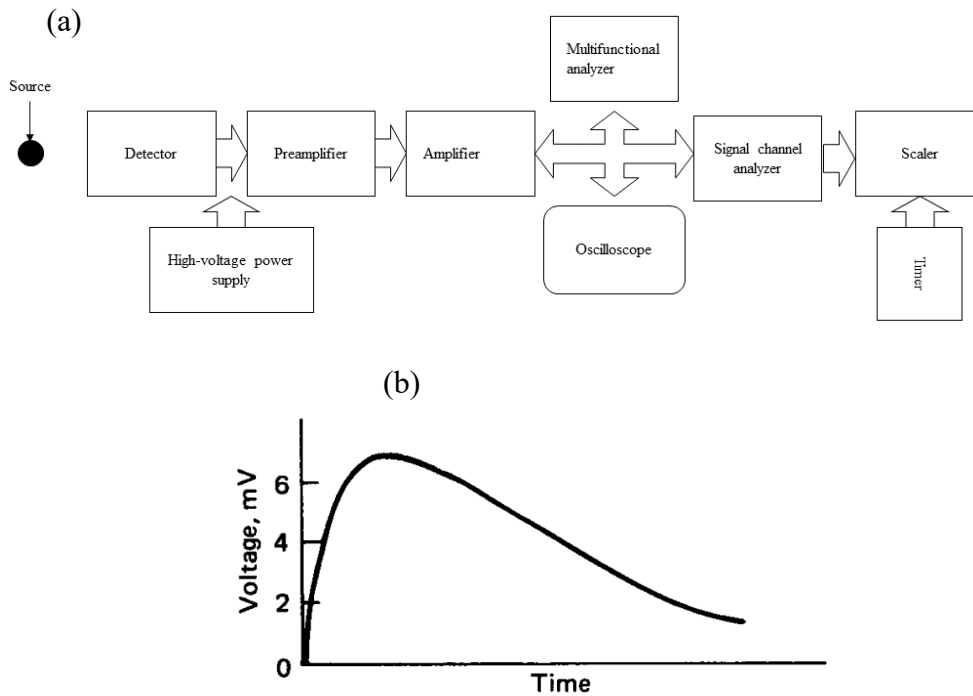


Figure 4.8 (a) Pulse type detection system schematic (b) a typical signal as detected in a pulse-based system [91]

typical pulse-type detector signal [91]. Later using the intensity signals and corresponding wavelengths in Planck's equation, temperature is determined.

Photoconductivity refers to the photoelectric phenomena where the electrical conductivity of a semiconductor material increases upon irradiation. With impinging radiation of sufficient frequency, an added stream of photo electrons supports conduction, and hence the improved conductivity [92].

Photodiodes is another type of photodetector that functions as a regular semiconductor diode but with the added capacity of receiving electromagnetic radiation at the sensitive portion i.e. the junction of the diode. They could consist of a single photovoltaic detector or photovoltaic multiple junction detectors. Upon irradiation, photons of sufficient frequency are absorbed in the depletion region, and electron-hole pairs are created. Amount of photocurrent generation is proportional to the number of electron-hole pairs created in the depletion zone. Therefore, an increased depletion zone translates into a more efficient photodiode because of the capacity to use more of the incident radiation for electron-hole pair generation. To facilitate an increased depletion zone, photodiodes are operated in reverse bias [93]. Photodiodes for IR detection are made of germanium semiconductor materials because of the favorable spectral response of band from 0.4 to 1.7 μm .

Other types of photodetectors in use are photovoltaic cells, vacuum photocells, etc. Photovoltaic cells are constructed by means of thin film deposition method on metal substrate, and they are the unit component of a solar array used to generate electricity from sunlight. A lower sensitivity of the photovoltaic cells renders them suitable for high temperature application only. In vacuum photocells, an anode is kept inside a glass bulb under vacuum condition. At any given potential difference between the anode and cathode, electric current in the circuit is a measure of the intensity of the incident radiation. The quantum well concept is utilized in charged couple devices (CCD) where a silicon substrate works as a photoactive region unto which the incoming radiation impinges and creates a charged spot. The produced charges are then transferred for post processing by means of metal oxide semiconductor field effect transistor (MOSFET) [94]. By post processing, it is meant that the collected charges could be digitized for storage or could be transformed into a movie by continuous feeding of the analog data as in the case of a camera.

4.5.3 Detectivity of Photodetectors

Detectivity of photodetectors are gaged by the signal to noise ration (SNR) at a detector output. Use of a normalized detectivity value is standard practice in the industry. SNR at the detector output is normalized to unit radiant power in watts (W), unit detector optical area in cm^2 and unit bandwidth in Hz to yield the normalized detectivity expressed as D^* for a photodetector. A higher D^* indicates a better detector. D^* is given by equation (4.11) [95],

$$D^* = \frac{\sqrt{A\Delta f}}{NEP}, NEP = \frac{I_N}{S} \quad (4.11)$$

where I_N is the noise current generating from thermal agitation of the electrons, Δf is the electrical bandwidth of the detector, A is the detector area, and S is the responsivity. ‘NEP’ stands for noise equivalent power.

Photovoltaic (PV) and photoconductor (PC) are the two types of photodetectors that are used with pyrometers and scanners because of their high detectivity and variation of wavelength that could be detected [96]. Mercury(Hg)-cadmium(Cd)-telluride(Te), commonly known as MCT is an alloy of CdTe and HgTe with the generic composition $Hg_{1-x}Cd_xTe$. Ratio of the constituting elements could be shifted to achieve detection of different wavelength bands. For example, one supplier [96] used graded gap MCT structures to achieve MWIR (3-6 μm) and LWIR (8-14 μm) detection. Thermoelectric cooling achieved according to Peltier effect [97] help reduce detector noise, increases responsivity, and improves high frequency response. DC biased two, three, and four stage thermoelectric cooling are available with heat sinks at 200 to 300 K depending upon the number of cooling stages used. Figure 4.9 shows how the thermoelectric cooling affect the

performance of detectors [96]. It could be observed that cooling not only improves detectivity but also extends the wavelength range that could be detected.

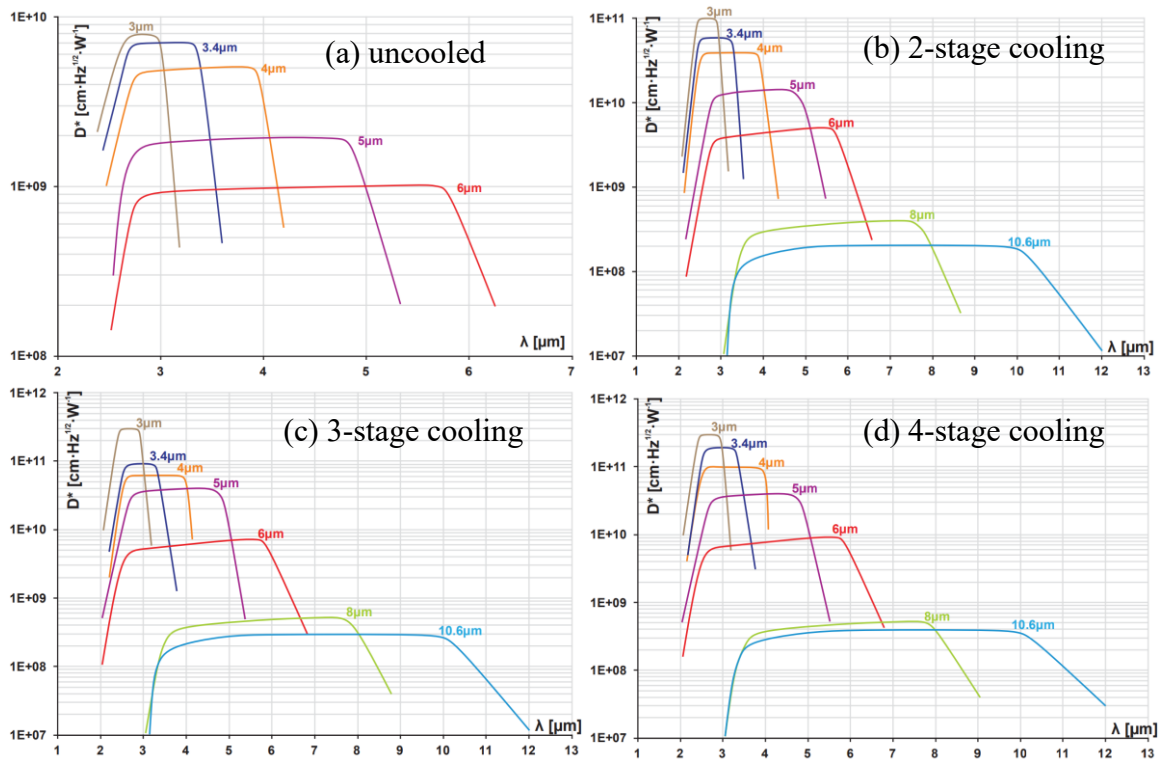


Figure 4.9 Spectral response of photovoltaic (PV) detectors made of MCT structures with and without cooling [96]

Other ternary alloy systems such as InAsSbm HgZnTe and HgMnTe have been used as intrinsic detectors. In addition, GaAs/AlGaAs based quantum well infrared photodetectors (QWIPs) technology is also being considered because of ease of fabrication and application in large focal plane array application with comparable performance with MCT. Figure 4.10 shows a comparison of detectivity between MCT and QWIPs [98].

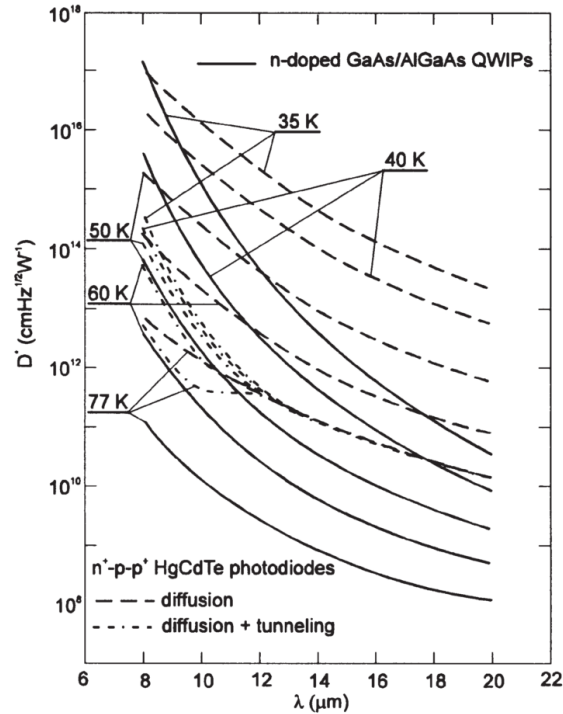


Figure 4.10 Comparison of directivity between HgCdTe or MCT and GaAs/AlGaAs based QWIPs photodetectors [998]

4.6 Wavelength Splitting/ Multiplexing

One of the major technical considerations in the fabrication of automatic radiation pyrometers working based on ratio pyrometry principle is the splitting of the incoming radiation

into the pyrometer's operating wavelength. More specifically, any hot object radiates at a wide range of IR radiation starting approximately at 700 nm and ending at 1 mm. Depending upon the

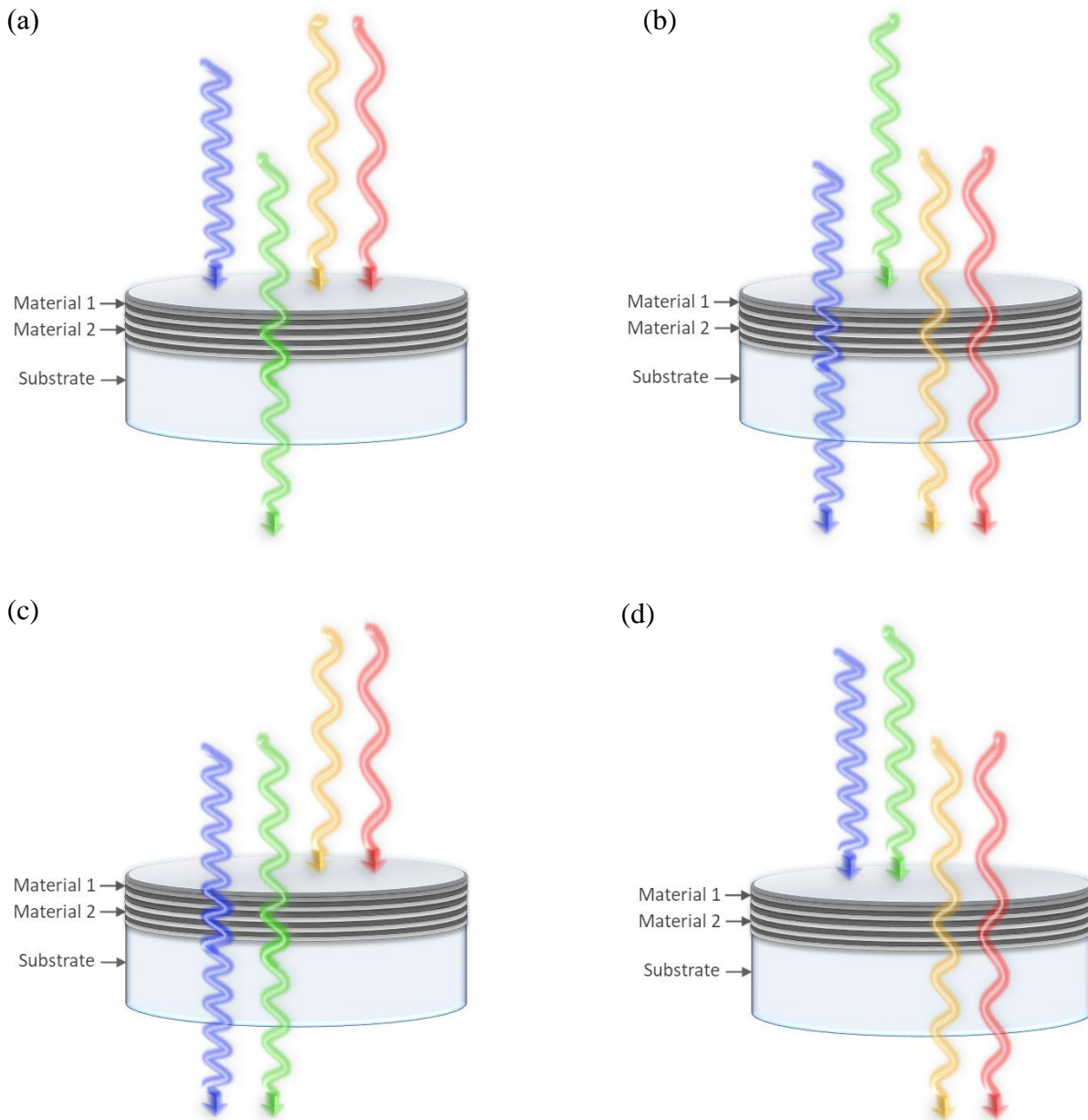


Figure 4.11 (a) bandpass filters (b) notch filters (c) short-pass filters (d) long-pass filters [100]

intended range of temperature a pyrometer is supposed to measure, a wavelength band in case of single wavelength pyrometers, two wavelength bands in case of dual wavelength pyrometers, and

multiple wavelength bands for multiwavelength pyrometers need to be fed to the detectors. Such separation of the wavelengths from the spectral radiation is achieved by means of wavelength division multiplexer (WDM) devices. Wavelength multiplexing or splitting of spectral radiation in multiple sub wavelength bands could be realized by dichroic mirrors, thin-film filters (TFF), fused fiber coupler devices, arrayed waveguide grating (AWG) technology, interleaver based technology, etc. Following is explanation of some of these techniques. Wavelength multiplexing

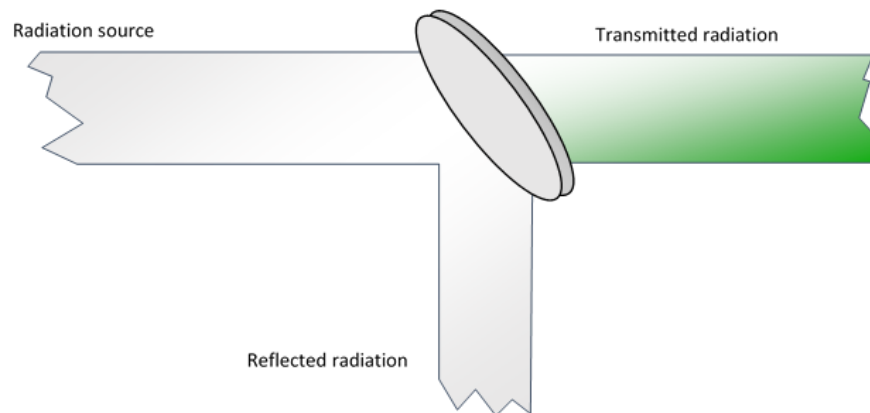


Figure 4.12 Schematic representation of a dichroic mirror placed at 45° with the incoming radiation [100]

systems consist of filters that may allow the transmission of wavelengths above a cut on wavelength (long pass filters), below a cut off wavelength (short pass filter), wavelengths in a narrow range around a specified wavelength (band pass filters), etc. There could be a neutral density (ND) filtering system that only reduces the intensity of the incoming radiation instead of dividing them in multiple wavelength bands. Such ND filters are used for beam attenuation for application in beam diagnostic studies to prevent over exposure of the detectors [99]. A graphical representation of different types of TFFs are shown in Figure 4.11 [100]

Dichroic mirrors or filters use the principle of interference to separate radiation of different wavelengths. Such mirrors are placed at an angle of 45° in the optical path and allows certain

wavelength to pass through and reflect back certain wavelength; thus the splitting occurs. When electromagnetic radiation is incident upon the interface of two mediums with different refractive indexes, the reflected radiation would change phase by $\frac{1}{2}$ wavelength if the refractive index of the second medium is greater than the first one [101]. When multiple thin films coated with different refractive index materials are stacked on a glass substrate, a dichroic mirror is created that enables positive interference of certain wavelengths that are reflected at right angles from the path of the radiation. Figure 4.12 shows a schematic representation of a dichroic filter.

Thin film filters (TFF) is another means of splitting the incoming radiation into selected wavelengths bands based on the same differential refractive index principle as in the case of dichroic mirror. In this case, multiple material coating is applied on a glass substrate. These material coatings allow for internal interference of radiation with different wavelengths when it passes through the filter. Based on the chemistry of deposition and the size of thin films, radiation is reflected, transmitted, and/or absorbed to render specific filtering effects as shown in Figure 4.12 [100].

Arrayed waveguide grating (AWG) consists of input and output waveguides arranged on a plane and coupled by two star couplers. Function of the star couplers is to take the input signal

from one waveguide and split it into several output signals [102] when the AWG is used as

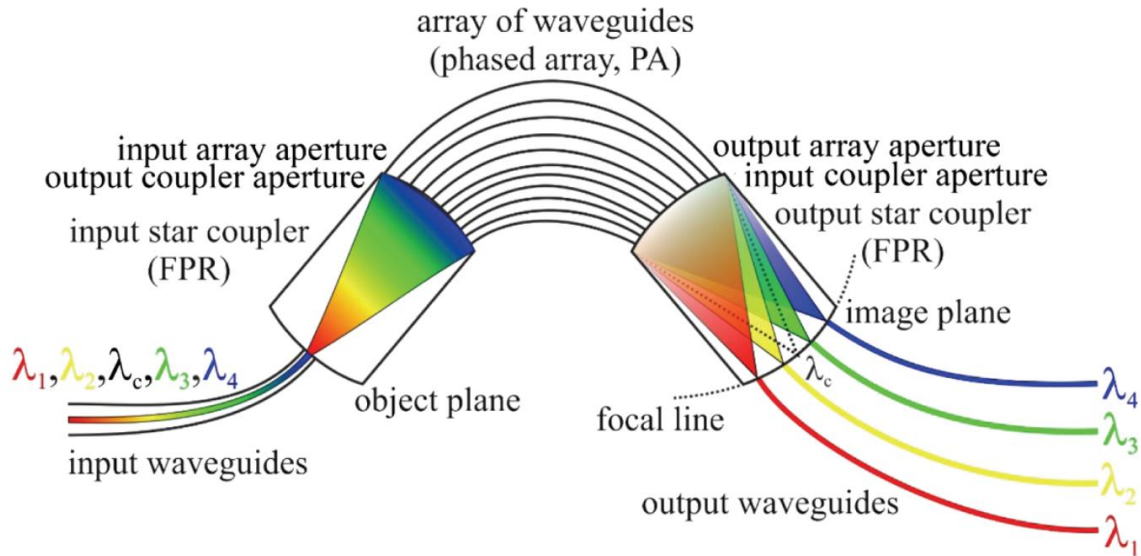


Figure 4.13 Schematic of an arrayed waveguide grating in demultiplexing (splitting a spectral signal into discrete bands) [103]

demultiplexer. A schematic representation of the device is given Figure 4.13 [103]. A detailed description of such a device was given by [104]. In general, AWGs work on the principle of phasing an array of input radiation by means of free expansion and subsequent passing through a set of coplanar and parallel waveguides of different lengths. An waveguide centrally positioned at the input star coupler carries an optical signal with multiple wavelengths such as $\lambda_1, \lambda_2, \lambda_3$, etc. Once the input optical signal reaches the coupler, it propagates freely in a diverging manner until getting captured the input array apertures of the output star coupler. The length of the parallelly placed array of waveguides differ from each other by a fixed amount ΔL related to the central wavelength, λ_c of the incoming optical signal. Such a change in phase forces the the different wavelengths within the input signal to be focused on different positions of the image plane. When

output waveguides are placed at these locations of the image plane, the distinctly splitted wavelengths i.e. $\lambda_1, \lambda_2, \lambda_3$, etc. are obtained.

4.7 Challenges in Pyrometric Measurements of Metals

4.7.1 Challenge with Changing Emissivity

For a single wavelength pyrometer, when measuring a the surface temperature of a real non-gray object with changing emissivity, measurement errors could be estimated using the following equation [72],

$$E_T = (T_m - T_t) * \frac{100}{T_t} \% \quad (4.12)$$

where, T_m and T_t are measured and real temperatures respectively. It was shown that for a 20% change in emissivity an error of 4.8% was observed in temperature measurement; i.e. for a true surface temperature of 1500 °C, the pyrometer would measure 1573 °C,

Emissivity can change based on surface conditions, such as oxidized and unoxidized surface, surface roughness, etc. and temperature. A pyrometer calibrated for polished Ti-6Al-4V alloy would yield an error of 23% in case of a Ti-6Al-4V surface with oxide. The problem is more pronounced in case of metals with lower emissivity such as aluminum [105].

4.7.2 Dependence of Emissivity on Angle of View

Pyrometers employ Planck's equation or any modified version of it to determine the temperature of a surface. However, the requirement of emissivity input to determine temperatures using a single wavelength pyrometer is a difficult proposition since emissivity changes with factors such as surface roughness, target temperature, and viewing angle to name a few.

Radiant intensity of a black body as function of radiation direction is given by Lambert's law to be,

$$W_{o\phi} = W_{o\perp} \cos\phi \quad (4.13)$$

where, $W_{o\phi}$ is the total radiant intensity of an area under the solid angle between the radiation direction and the direction perpendicular to the surface of the heat source, and $W_{o\perp}$ is the radiation intensity of black body in the direction normal to the surface which is approximated as

$$W_{o\perp} = \frac{W_o}{\pi} \quad (4.14)$$

Lambert's equation is affected by the value of observation angle and yields large errors beyond $\phi > 45^\circ$ for non-black bodies. Such errors are attributed to the dependence of emissivity of non-black bodies on the observation angle.

In case of a disappearing filament pyrometer, however, radiance is considered to establish temperature scale instead of radiant intensity. Like radiant intensity, radiance is not critically dependent on angle of view for black and non-black bodies. Therefore, disappearing filament pyrometer or any other pyrometer that employs radiance instead of radiant intensity for temperature measurement, low angle of view would not be a limiting factor.

4.7.3 Error Associated with Longer Wavelength

The relationship between wavelength and frequency of any electromagnetic radiation is given by the following equation,

$$\lambda = \frac{c}{\nu} \quad (4.15)$$

Here, λ and ν are the wavelength and frequency of the incident radiation, respectively, and c is the speed of light. From the above equation, wavelength and frequency are inversely proportional. In case of long wavelength radiation received by the photoelectric

detector of a pyrometer, the intensity reading could be ‘bad’ as discussed in reference [91] and

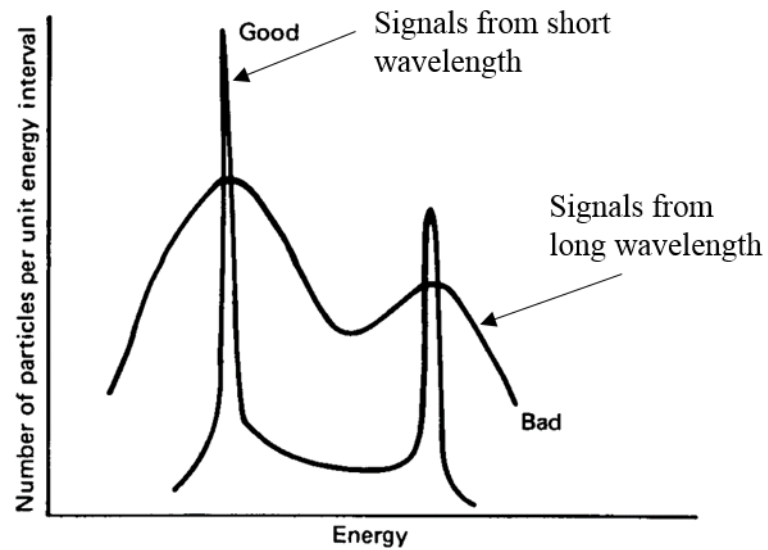


Figure 4.14 Long wavelength could result in peak broadening and subsequent inaccurate output of temperature [91]

shown in Figure (4.14). A ‘bad’ signal could be the one that would not have a definite peak and therefore would result in a higher noise level leading to an erroneous temperature reading.

4.7.4 Selecting the Right Fiber Optic

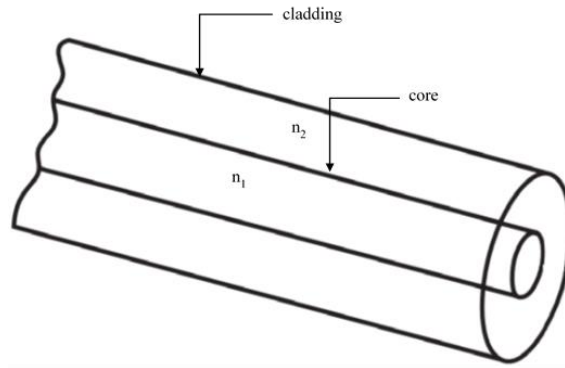


Figure 4.15 Basic construction of a fiber optic cable with cladding to provide total internal reflection of the light signal that falls within angle of acceptance [106]

An optical fiber has the following construction as shown in Figure (4.15) [106]. It consists of a transparent core and a cladding also of transparent material. Refractive index of the core is slightly greater than that of the cladding ensuring total internal reflection of the optical signal and subsequent transmission. Selection of an optical fiber depends on the parameters such as, acceptance angle and numerical aperture

Chapter 5: Published Work – Crack-Free Aluminum 6061 Fabrication

Demonstration

This chapter includes the original work by the author of this thesis published in a journal article. Copyright permissions was obtained from Elsevier and correspondence with the publisher is included in appendix C.

5.1 Title, Authors, and Affiliations

Processing and Characterization of Crack-Free Aluminum 6061 Using High-Temperature Heating in Laser Powder Bed Fusion Additive Manufacturing [11]

Authors: Syed Z. Uddin^{a,b}, Lawrence E. Murr^{a,c}, Cesar A. Terrazas^{a,b}, Philip Morton^{a,b}, David A. Roberson^{a,c}, Ryan B. Wicker^{a,b}

Affiliations:

a. W.M. Keck Center for 3D Innovation, The University of Texas at El Paso, El Paso, TX, USA

b. Mechanical Engineering Department, The University of Texas at El Paso, El Paso, TX, USA

c. Metallurgical, Materials and Biomedical Engineering Department, The University of Texas at El Paso, El Paso, TX, USA

5.2 Abstract

During solidification of many so-called high-performance engineering alloys, such as 6000 and 7000 series aluminum alloys, which are also unweldable autogenously, volumetric solidification shrinkage and thermal contraction produces voids and cracks. During additive manufacturing processing, these defects can span the length of columnar grains, as well as intergranular regions. In this research, laser powder bed fusion (LPBF) of aluminum alloy (AA)

6061 used powder bed heating at 500 °C in combination with other experimentally determined processing parameters to produce crack-free components. In addition, melt-pool banding, which is a normal solidification feature in LPBF, was eliminated, illustrating solidification process modification as a consequence of powder bed heating. Corresponding microindentation hardness and tensile testing of the as-fabricated AA6061 components indicated an average Vickers hardness of HV 54, and tensile yield, ultimate strength, and elongation values of 60 MPa, 130 MPa, and 15%, respectively. These mechanical properties and those of heat treated parts showed values comparable to annealed and T6 heat treated wrought products, respectively. X-ray diffraction and optical microscopy revealed columnar grain growth in the build direction with the as-fabricated, powder-bed heated product microstructure characterized by [100] textured, elongated grains (~ 25 µm wide by 400 µm in length), and both intragranular and intergranular, noncoherent Al-Si-O precipitates which did not contribute significantly to the mechanical properties. The results of this study are indicative that powder bed heating may be used to assist with successful fabrication of AA6061 and other alloy systems susceptible to additive manufacturing solidification cracking.

Key Words: aluminum 6061, laser powder bed fusion additive manufacturing, powder bed induction heating, crack-free fabrication

5.3 Methodology

5.3.1 Materials

The precursor AA6061 powder used in this study was acquired from LPW Technologies (LPW-6061-AAGX, LPW Technologies, Pittsburgh, PA). The powder was manufactured from pre-alloyed AA6061 stock by gas atomization. To minimize oxidation and moisture pickup, the powders were shipped in vacuum sealed containers containing silica gel pouches. After each

experiment using LPBF, the powder was stored in stainless steel jars under atmospheric pressure and covered with the silica gel pouches. During each build, the build chamber was continuously purged with class 2.2, UN1006 argon (Ar) supplied in a T-type cylinder (SYOXSA®, El Paso, TX).

Samples of the AA6061 powder were collected and characterized using a variable pressure tabletop microscope from Hitachi (TM1000, Hitachi, Ltd., Tokyo, Japan). The powder morphology consisted of spherical and semi-spherical particles with satellites as shown in Figure 5.1 (a). Some irregular shaped or flake powder was also observed. As shown in the histogram of Figure 5.1 (b), the batch of powder used for this study had a slightly skewed normal distribution with mean powder size of 27 μm . Powder distribution was skewed towards the finer particles. The apparent density AD_H and Hall flow rate (FR_H) of the precursor powder were measured using a Hall flowmeter (Part#2896, Acupowder International LLC, NJ, USA) according to ASTM B212 and ASTM B213 standards, respectively [107,108]. The AD_H and FR_H were measured to be 1.4 g/cc and 77.4 s/50 g, respectively. Besides the standards already mentioned, the powder characterization in this work adhered to the definitions in ASTM F3049-14.

A cylindrical build plate was made of T6 treated AA6061 and used as the substrate for fabrication. The plate had a thickness of 12.5 mm and a diameter of 200 mm (6061-T651 ALUMINUM, Aarmor Metal & Supply Co.,El Paso, TX).

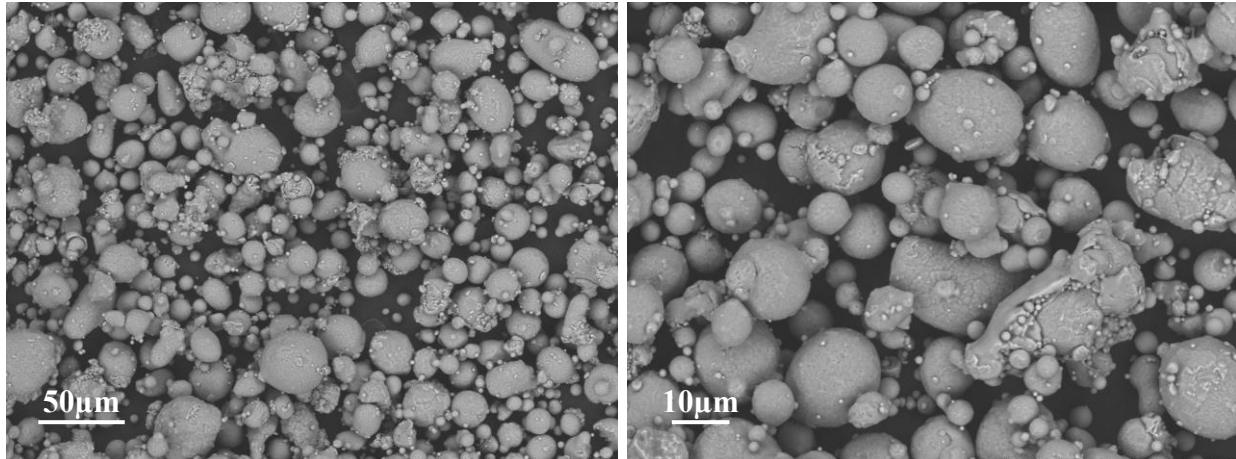


Figure 5.1 (a) SEM images of AA6061 gas atomized powder. Powder particles were spherical, and semi-spherical with satellites. Some irregular shaped powder was also observed

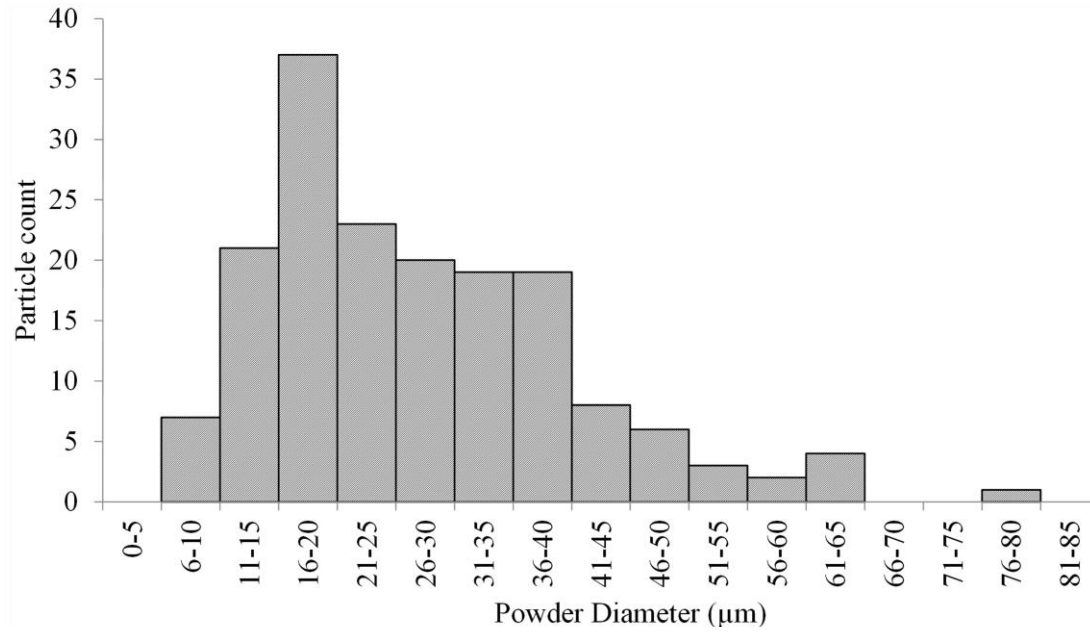


Figure 5.1 (b) Histogram of AA6061 powder size distribution

5.3.2 LPBF Fabrication Process

An open architecture AconityONE LPBF system manufactured by Aconity3D (Aachen, Germany) was used in this study. The AconityONE incorporates a laser system from IPG Laser GmbH (YLR-1000-WC, IPG Laser GmbH, Burbach, Germany) consisting of an Nd-YAG 1 kW class 4 laser operating in the near infrared spectrum ($\lambda = 1030$ nm). The laser was guided using a 3D scan-head from SCANLAB (varioSCAN_{de}40i, SCANLAB AG, Puchheim, Germany). The overall focal length of the system was continuously adjusted through dynamically positioned diverging optics. Such adjustment of focal length enabled the laser beam focus to remain constant on the build plane. Figure 5.2 (a) shows the flat focal plane represented by the solid line (item 6 in the legend) that results from adjustable optics. Figure 5.2 (a) also shows the curved plane as

represented by dotted curvilinear (item 5 in the legend) that would result if the optics were

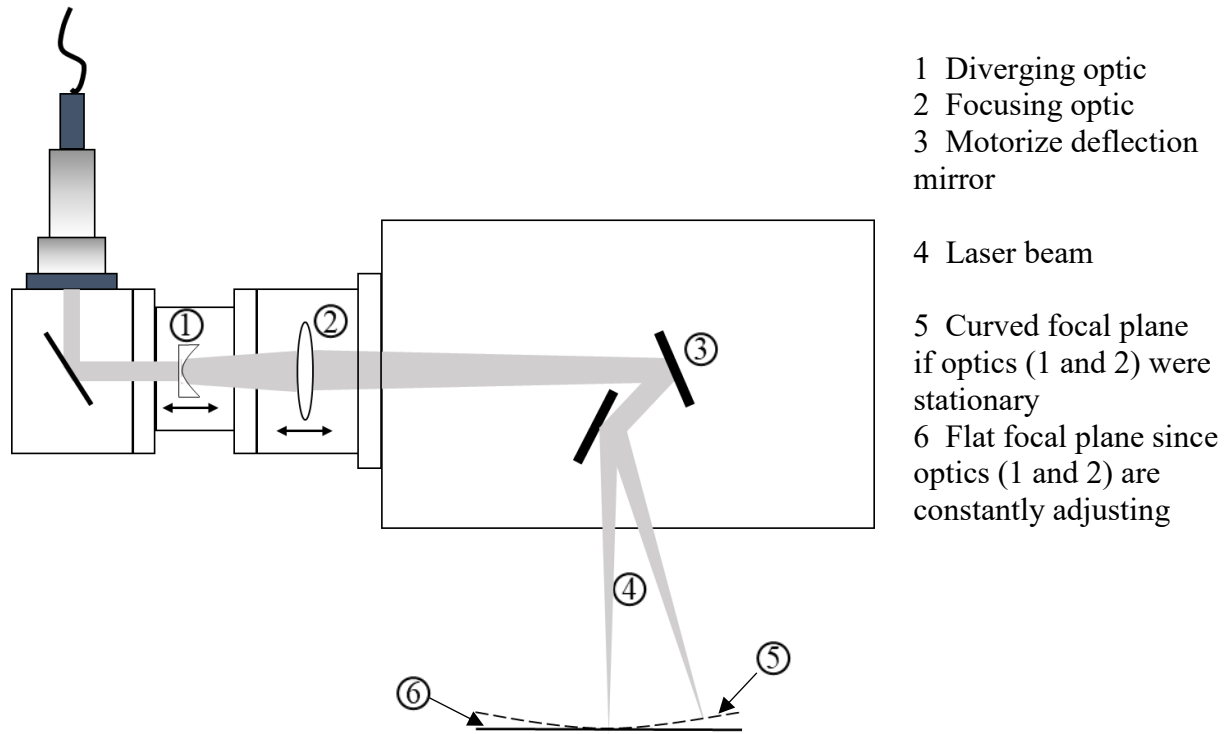


Figure 5. 2 (a) Scan-head of the AconityONE system consisting of the Galvo mirrors and f- θ lens. The optical fiber receives the 1030 nm wavelength, near infrared laser from the laser module where Nd:YAG crystals were used for solid state amplification. The scan-head is capable of rastering over an area of 400 mm in diameter. However, during heated bed configuration a reduced scan area with 200 mm in diameter is covered.

Table 5.1 Range of LPBF parameters explored to find the crack-free parameter combination

Powder bed temperature ($^{\circ}\text{C}$)	Layer thickness (μm)	Hatch Spacing (μm)	Power (W)	Scan speed (mm/s)
350 - 500	30 - 100	80 - 140	150 - 500	500 - 2800

stationary.

Another important characteristic of the AconityONE system was the ability to heat the powder bed. This was achieved with the use of an induction heating system (TruHeat HF Series 3010, TRUMPF Inc., Freiburg, Germany). This induction setup enabled heating of the powder bed to a maximum of ~ 1000 °C, although the heated powder bed configuration reduced the available build area from 400 mm to 200 mm in diameter. The laser module, induction generator, and transformer required water cooling employing a chiller with 4.9 kW cooling capacity (WKS 151.2M5LE.I, RIEDEL[®], Glen Dimplex Deutschland GmbH, Kulmbach, Germany). The laser could also be air cooled when operated at or below 400 W of power.

In the current study, the AconityONE system was used to produce AA6061 test coupons with and without the use of powder bed heating. Build orientation of the coupons are reported according to ISO/ASTM52921-13 [8]. The cube coupons had dimensions of 10 mm x 10 mm x 10 mm. Also, four cylindrical coupons with 16 mm diameter and 76 mm height were fabricated

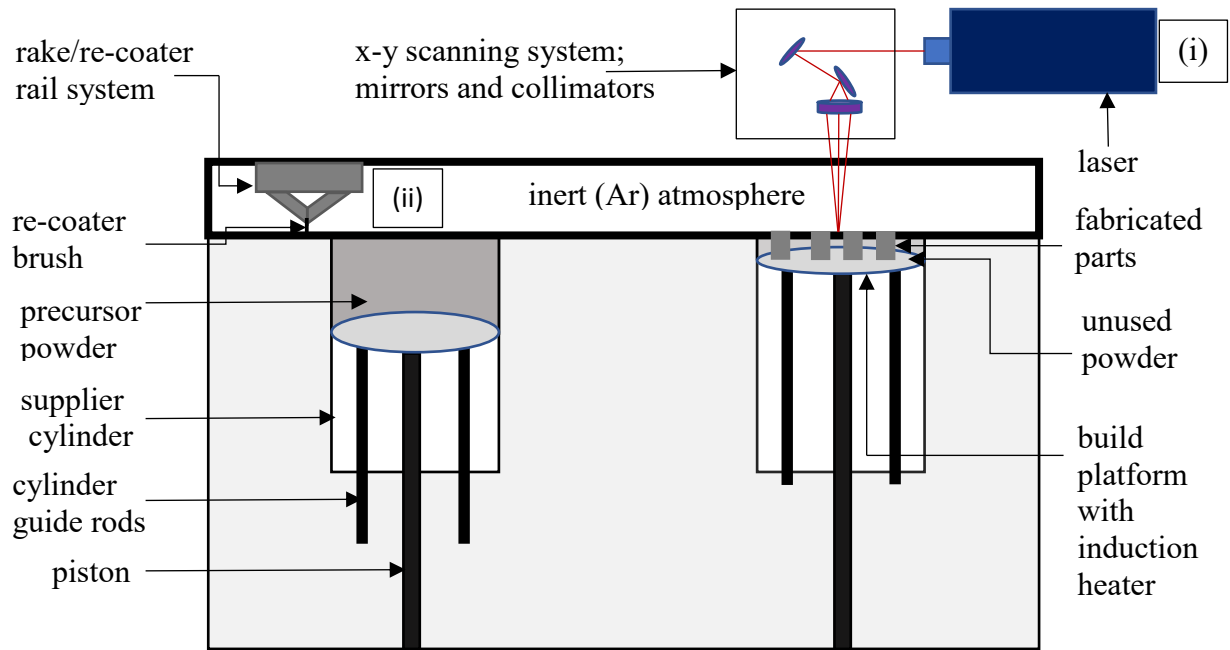


Figure 5.2 (b) A schematic representation of the AconityONE LPBF system used for the study. (i) Solid state Nd:YAG laser of 1030nm wavelength and 1kW capacity and an induction heater (not shown in figure) underneath the build platform that can raise the powder bed temperature to 1000°C are featured. (ii) The re-coater brush is made of carbon fiber to impart flexibility and high heat resistance. in the X direction that were machined afterwards as tensile specimens. The range of scanning parameters used for the fabrication of the cubic coupons is shown in Table 1. The combination of 500 °C preheating, 400 W laser power, 1400 mm/s scanning speed, 100 μm layer thickness and 140 μm hatch spacing resulted in crack-free fabrication of cubic coupons. It was hypothesized that larger layer thicknesses increased molten mass and facilitated liquid metal flow at later stages

of solidification, and thus, increasing layer thickness was explored. However, larger layer thicknesses have been shown to facilitate porosity formation [109] with porosity being overcome in some cases by adjusting other parameters such as scanning speed, laser power [110], and laser hatch spacing, resulting in the parameters explored in the current study. Laser spot diameter [111] has also been shown to impact porosity, but not studied here. In the current work, the parameters that resulted in crack-free AA6061 coupons were also used to fabricate the AA6061 tensile specimens. The crack-free processing parameters were determined empirically by experimentation where the absence of cracks, as measured from micrographs, was the acceptance criteria.

To begin fabrication, the build platform was lowered by a distance equal to that of the layer thickness, and the supplier powder bed was raised by a height multiple of the layer thickness depending upon the supply factor to ensure enough supply of the powder. For the current study, a supply factor of three was used. Powder spreading was carried out by back and forth movement of a rake tipped with carbon fiber brushes to withstand the high temperature of the build platform when the induction heater was used. A schematic representation of the AconityONE setup is shown in Figure 5.2 (b). During the fabrication process, an O₂ sensor (ZR5-1.1A, ZIROX GmbH, Greifswald, Germany) continuously monitored the O₂ level of the process chamber in parts per million (ppm). The O₂ level was maintained below 200 ppm throughout the fabrication process to reduce the oxide formation.

5.3.3 Material Characterization

Density of the fabricated cube coupons with and without powder bed heating was measured following ASTM standard B311–17 [112] using Archimedes principle. A weighing scale of 0.001g precision (Sartorius M-prove AY303, IL, USA) was used for measuring the weights of the

coupons, first in air, and then when submerged in water. Three measurements were made per specimen for each condition (i.e. in air and submerged in water), and the values entered in the following equation to obtain the density:

$$D = \frac{A * E}{A - F}$$

where A and F are the measured weights of the specimen in air and in water, respectively, and E is distilled water density at the working temperature obtained from the tabulated values provided in the standard [112]. Percent relative density values were calculated by dividing the LPBF fabricated AA6061 density by the nominal density of AA6061 which is 2.7 g/cm³.

For microstructure analysis, the fabricated specimens were cut and analyzed in the ZX and XY planes to expose the build direction and the cross-section microstructures, respectively. Definitions of the planes were determined based on ASTM F2971-13 [113]. Sectioning of the specimens along the above-mentioned planes was performed using a precision cutter (TECHCUT 5TM Allied High-Tech Products, Inc., Compton, CA, USA). The sections were mounted in 31.8 mm molds using Koldmount liquid and powder mixed in 1:2 ratio. After the resin mixture was set, the mounted specimens were taken out of the mold, and ground using silicon carbide (SiC) grinding paper of increasing grit size from #320 to #1200. Grinding was followed by polishing using a slurry consisting of soap water, ethyl alcohol, and alumina (Al₂O₃) dispersed on a polishing cloth. Fine Al₂O₃ powders with sizes of 0.3 μm, 0.1 μm, and 0.05 μm were used in a final polishing step. To reveal the microstructure, the samples were exposed to an etchant containing 25 ml methanol (CH₃OH), 25 ml hydrochloric acid (HCl), 25 ml nitric acid (HNO₃), and 1 ml hydrofluoric acid (HF). The specimens were submerged in the etchant for 25 seconds at a time, followed by rinsing with deionized water. The microstructures were studied using an inverted optical microscope (Reichert MEF4 A/M, Reichert Inc., New York, USA).

Texturing and phases precipitated in the AA6061 specimens produced by LPBF were investigated through X-Ray diffraction (XRD) using a PANalytical EMPYREAN diffractometer (Malvern Panalytical B.V., Netherlands) equipped with an Anton Paar sample stage XRK 900 (Anton Paar USA, Ashland, VA, USA) operating with 1.54 Å Cu k- α radiation. Scanning electron microscopy was carried out using a scanning electron microscope (SEM) from Hitachi (SU3500, Hitachi America, Ltd, New York, USA) operating with an acceleration voltage of 30 kV and equipped with a Deben (Deben UK, Ltd, London, England) scanning transmission electron microscope (STEM) detector. Prior to STEM imaging, samples were ground to a thickness of ~200 μ m and then electro-jet polished with an electropolisher (Model 110 Automatic Twin-Jet Electropolisher, Fischione Instruments, Pittsburgh, PA, USA) using a solution of 20% by volume of nitric acid in methanol at -20 °C.

5.3.4 Mechanical Properties

5.3.4 (i) Microhardness

Microhardness measurements of the specimens were recorded using a Struers hardness testing machine (Duramin-A300, Struers Inc., Ohio, USA) in the Vickers (HV) hardness scale. Microhardness testing specimens were prepared from three different conditions; such as, a cube coupon fabricated without powder bed heating, a cube coupon fabricated with powder bed heating, and a circular section from the threaded grip area of a T6 heat treated tensile testing specimen after the tensile testing was performed. Starting just above the support structure, a total of 10 indentations were made along the build direction of the cube specimens using a load of 100 gf and spaced in intervals of 1 mm. Microhardness corresponding to the condition of fabrication with powder bed heating and subsequent T6 heat treatment was obtained by making measurements on

a specimen prepared from the tensile bar that had undergone tensile testing. A circular cross section of the threaded grip area of the tensile specimen was mounted in a 31.8 mm mold and polished before making 15 indentations at different locations of the cross section.

5.3.4 (ii) Tensile Properties

Four tensile testing specimens were machined from AA6061 cylinders fabricated on heated powder bed in the X direction. Out of those four specimens, two specimens were tested as fabricated, and the other two were tested after heat treatment to T6 conditions. Since demonstration of crack-free fabrication of AA6061 and microstructural characterization were the focus of the current study, only four specimens were tensile tested. A complete statistical study of mechanical performance is ongoing using specimens produced in the X, Y, Z , XY+45° and X+45° orientations as per ASTM F2971-13[113]. The cylinders were built with a diameter of 16 mm and height of 76 mm. Small size specimens with dimensions adhering to the ASTM E8M –16a standard [114] were machined from the cylinders with a gage length of 30 ± 0.1 mm, and diameter of 6 ± 0.1 mm at the gage or reduced section. Tension testing of the specimens was performed using an MTS Landmark Servo-hydraulic test system (Model: 39-075103, MTS Systems Corporation, USA) using closed-loop control with a set strain rate of 0.015 ± 0.006 mm/mm/min to find the 0.2% yield strength (YS), ultimate tensile strength (UTS), and elongation at break

5.4 Results and Discussion

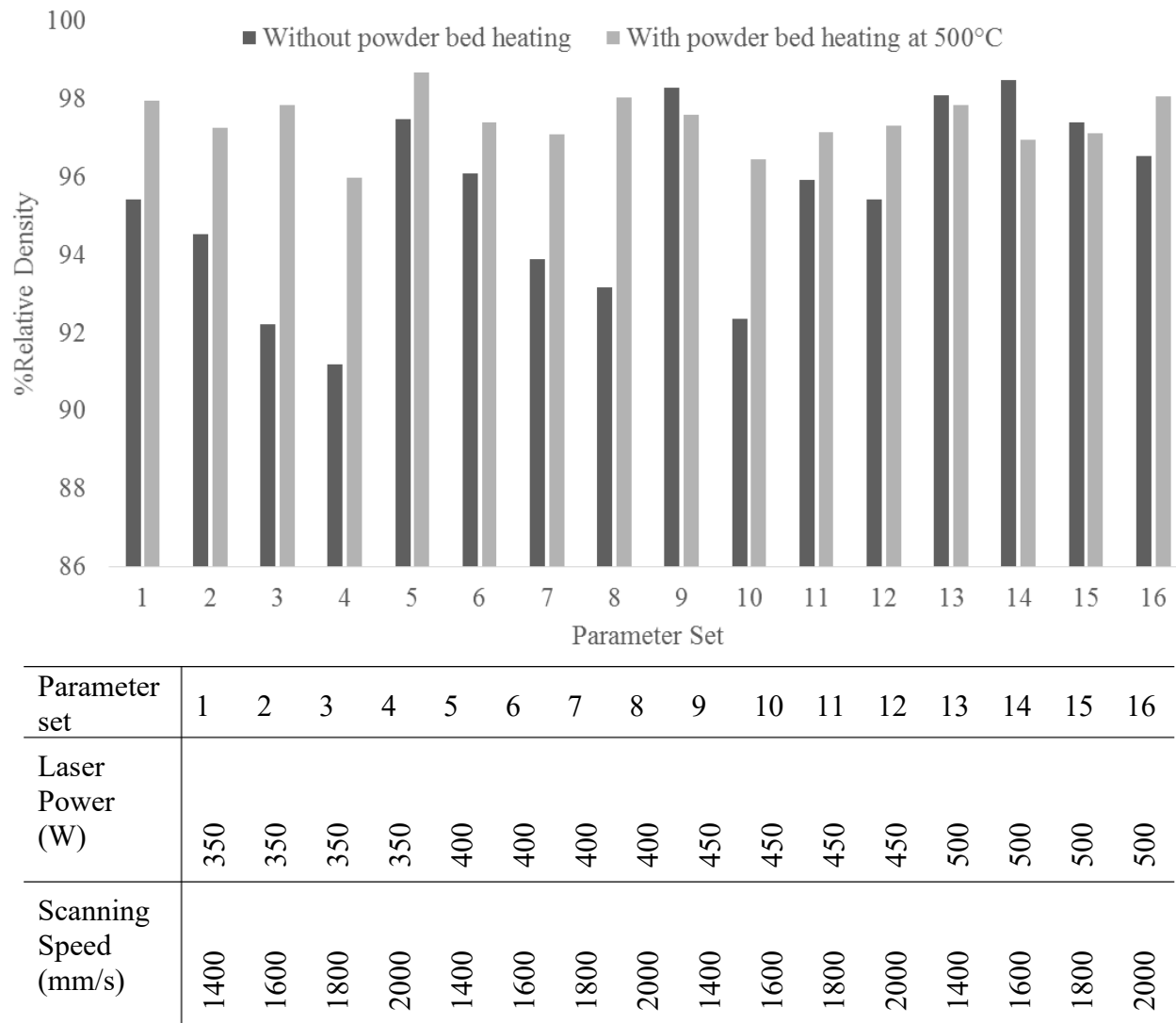


Figure 5.3 Relative density of AA6061 cube coupons fabricated using different laser power and scanning speed with and without heating of the powder bed

5.4.1 Density

Relative density of AA6061 cube coupons fabricated with different scan speeds and laser power was measured as part of the process parameter development study [115]. Density measurements of 32 specimens, 16 of which were fabricated with powder bed heating and the remaining 16 without powder bed heating, are shown in Figure 5.3. In general, relative density of

the cubes fabricated with induction heating was greater than that of the cubes fabricated without induction heating. A maximum relative density of 98.7% was measured for cube coupons produced with induction heating. In some parameter sets, the relative densities for the cube specimens produced with and without powder bed heating were comparable; however, the presence of cracks in the cube coupons fabricated without induction heating, rendered the comparison insignificant.

5.4.2 Mechanical Properties

5.4.2 (i) Microhardness

Average Vickers microhardness of the AA6061 specimens fabricated without powder bed heating was measured to be 90 HV with a standard deviation of 6 HV. For the specimens fabricated with powder bed heating, the average and standard deviation of Vickers hardness were 54 HV and 2.5 HV, respectively. Microhardness values for the without powder-bed heating specimens were within the range of 70 – 107 HV which is typical for T6 treated AA6061; whereas, microhardness for the with powder-bed heating specimens was within the range 52 – 70 HV reported by Murr *et al.* [116] for AA6061 produced by friction-stir welding. Average

Table 5. 2 Microhardness values of LPBF fabricated AA6061 components under different conditions

Condition	Microhardness
As built without powder bed heating	90±6 HV
As built with powder bed heating at 500 °C	54±2.5 HV
T6 Heat treated sample after fabrication with powder bed heating at 500 °C	119±6 HV

microhardness for the tensile specimen fabricated with powder bed heating, and subsequently T6 heat treated, was measured to be 119 HV with a standard deviation of 6 HV. A summary of Microhardness values for the three

5.4.2 (ii) Tensile Properties

Upon testing of four tensile specimens, resulting YS, UTS, and percent elongation at breakpoint of LPBF fabricated AA6061 are presented in Table 3 (As mentioned above, printing of more samples for statistically relevant measurements is ongoing). Mechanical properties of AA6061 published by ASM International (Ohio, US) were also tabulated for reference [117]. Comparing with AA6061 in annealed condition, an improvement in YS and UTS could be observed whereas ductility was reduced for the LPBF fabricated parts.

Table 5.3 Comparison of mechanical properties of LPBF fabricated AA6061 and wrought annealed AA6061 for both annealed and T6 heat treated conditions

		YS (MPa)	UTS (MPa)	Percent Elongation at Breakpoint
Heated Powder Bed- LPBF Fabricated AA6061	Specimen 1	66	133	11
	Specimen 2	75	141	15
Heated Powder Bed- LPBF Fabricated AA6061 after T6 Treatment	Specimen 1	282	308	3.5
	Specimen 2	290	318	5.4
Wrought AA6061-O		55	124	30
Wrought T6 treated AA-6061		276	310	12

5.4.3 Microstructure

5.4.3 (i) Optical Microscopy

Optical micrographs were obtained and analyzed for two AA6061 coupons fabricated with the AconityONE, one fabricated with unheated powder bed, and the other fabricated with the powder bed heating at 500 °C. The micrographs in Figure 5.4 correspond to the microstructure for AA6061 produced without powder bed heating. Figure 5.4 (a) and (b) correspond to the ZX plane, whereas Figure 5.4 (c) and (d) correspond to the XY plane. The micrographs shown in Figure 5.4 reveal large cracks in the microstructure in both planes. Along with a high occurrence of cracks, a high degree of porosity can be appreciated. Similar cracks and porosity have been reported in other studies that involved LPBF of AA6061 [3,5,15] where the cracks were attributed to the large solidification range of the alloy. The spherical shape of the porosity is indicative of gas porosity [110] that could be formed by entrapped process gas, degassing of the metal powder, or porosity inherent in the metal powder during atomization. The presence of crescent shaped melt pools and banding of melt tracks are apparent in these micrographs. These melt-pool and melt

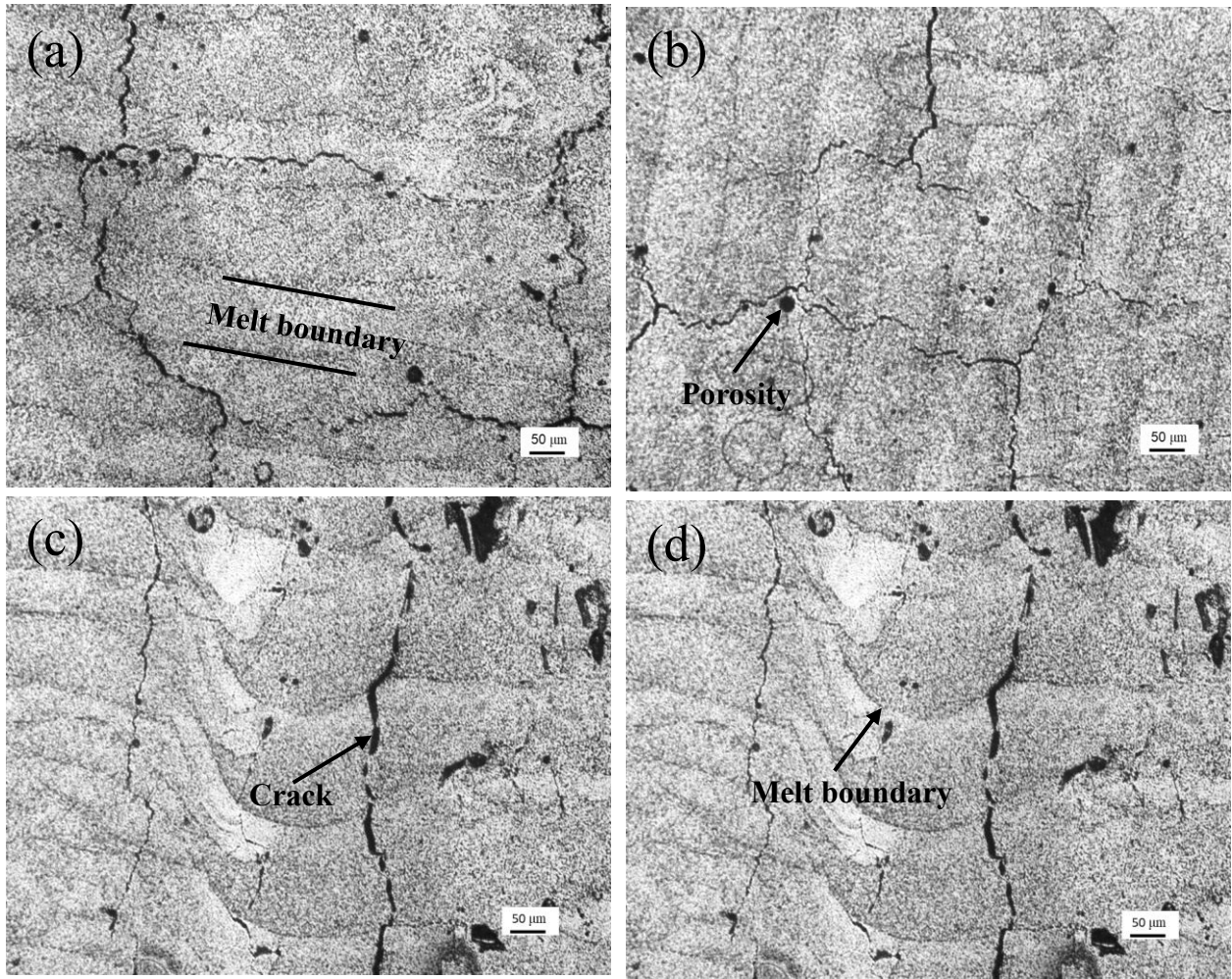


Figure 5.4 Microstructure of AA6061 specimens fabricated on unheated powder bed. Figure 5.4 (a) and (b) illustrate the XY plane (perpendicular to build direction). Figure 5.4 (c) and (d) show the ZX plane (build direction). Cracks, porosity, melt-pool, and melt-track banding are evident in the microstructure tracks features are typical of LPBF fabricated microstructures in various material systems [118].

The micrographs in Figure 5.5 illustrate the microstructure of a coupon built with a heated powder bed. Figure 5.5 (a) and (b) show the microstructure corresponding to the ZX plane, while Figure 5.5 (c) and (d) correspond to the XY plane. By contrast with the observations in Figure 5.4, these micrographs show no cracks and greatly reduced porosity overall. It is also significant

to note in Figure 5.5 (c) and (d) that the characteristic melt-pool banding shown in Figure 5.4 (c) and (d), and a normal solidification feature of LPBF, has been eliminated. This is indicative of

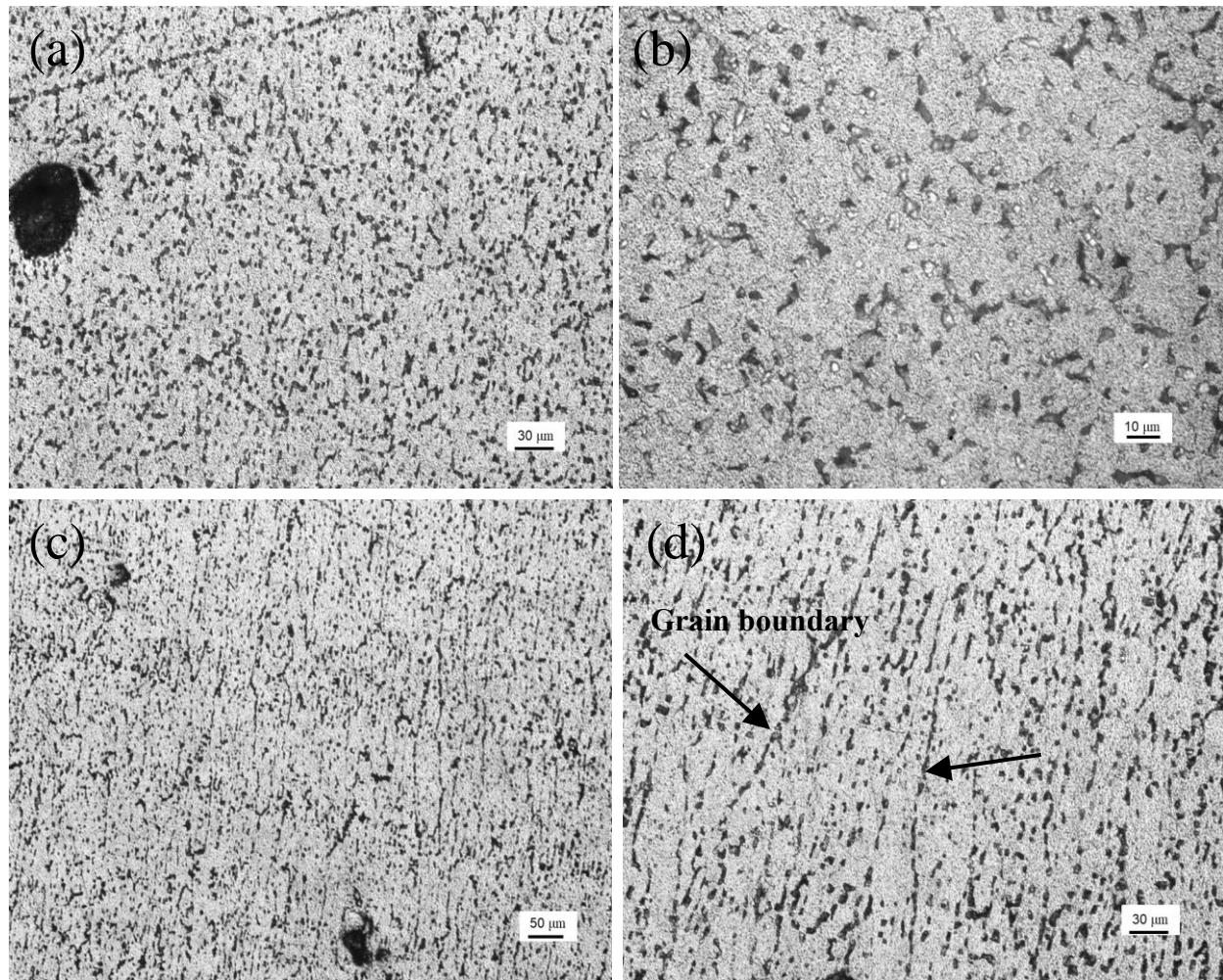


Figure 5.5 Microstructure of AA6061 specimens fabricated on powder bed heated to 500 °C.

Figure 5.5 (a) and (b) illustrate the XY plane (perpendicular to build direction).

Figure 5.5 (c) and (d) show the ZX plane (build direction). Cracks, porosity, melt pool, and melt-track banding removed from the microstructure, and a columnar grain growth is observed in the build direction

significant solidification process modification resulting from the powder bed heating.

In addition to somewhat traditional, elongated (and ellipsoidal) grains observed in the build

direction as shown in Figure 5.5 (c) and (d), having average lengths of roughly 0.4 mm and widths of $\sim 40\text{ }\mu\text{m}$ (a 10/1 ratio of length to width), there is a propensity of precipitates within the grain boundaries that appear somewhat homogeneously distributed throughout the matrix. The columnar grain boundaries decorated with precipitates are indicated with arrows in Figure 5.5 (d). As shown in Figure 6, these precipitates appear to be noncoherent dispersoids, having sizes ranging from $\sim 200\text{ nm}$ to as large as $5\text{ }\mu\text{m}$, with interparticle spacings averaging $\sim 1\text{--}3\text{ }\mu\text{m}$. Energy dispersive x-ray spectrometry (EDS) analysis of numerous particles indicated primarily Al-Si-O, often with high oxygen concentrations. These particles are not the usual strengthening particulate compositions in tempered AA6061 alloy [119,120], and do not appear to have a significant role in strengthening the as-fabricated LPBF product where the average Vickers micro-indentation hardness was HV 54 (540 MPa); and with corresponding ranges for mechanical properties of 60 to 75 MPa for yield strength, 130 to 140 MPa for ultimate tensile strength, and 11% to 15% for elongation. These as-fabricated mechanical properties correspond to annealed, wrought (or zero temper) AA6061 products where the Vickers microindentation hardness can range from HV 40 to HV 70 (400 to 700 MPa); while the corresponding yield strength, ultimate tensile strength, and elongation can range from 50 MPa – 110 MPa, 110 MPa – 150 MPa, and 14% – 25%, respectively.

This pre

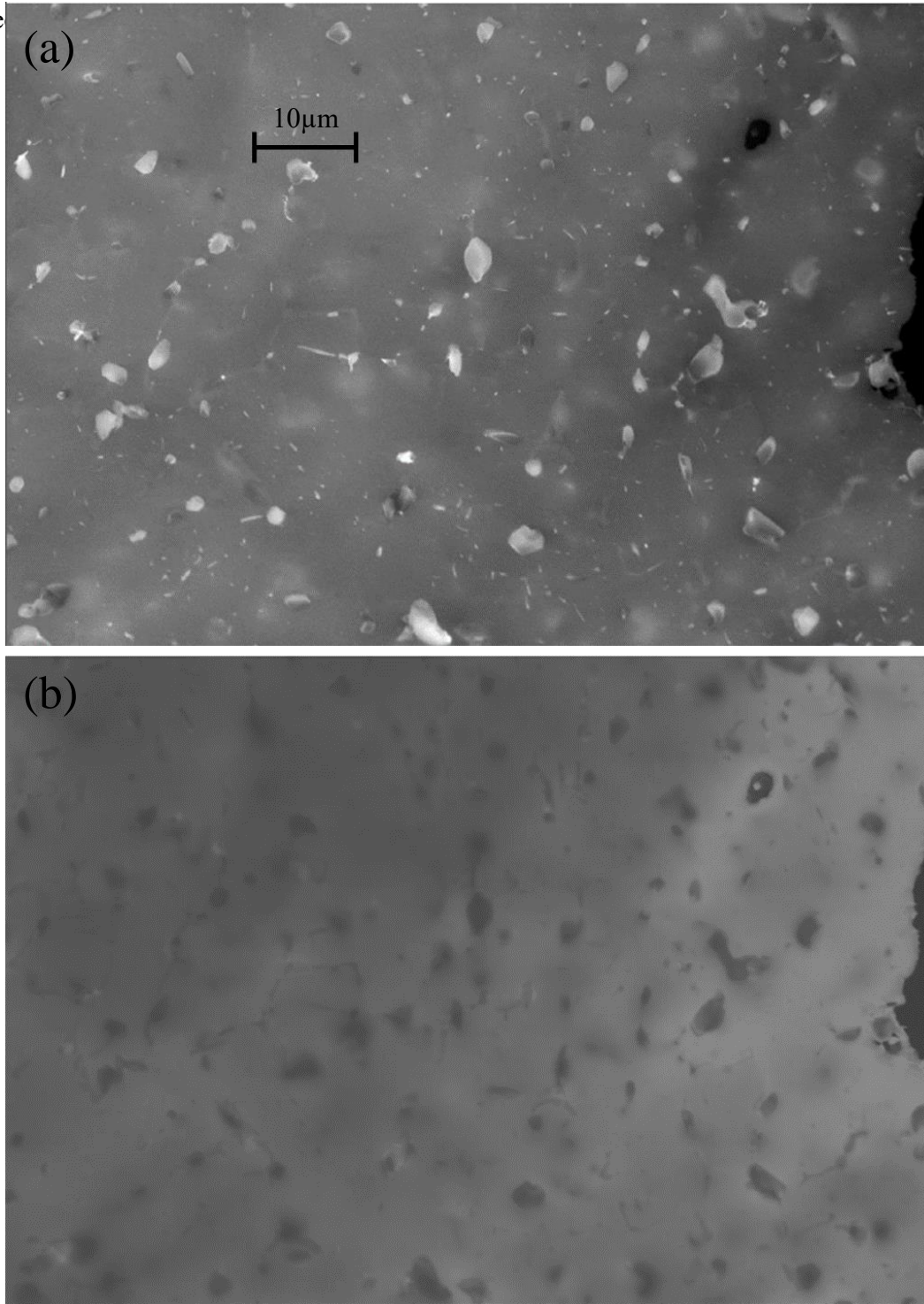


Figure 5.6 SEM (a) and STEM (b) images of primarily Al-Si-O noncoherent precipitates shown in Figure 5.5. The same area is imaged in (a) and (b) and the magnification for both is given in (a).

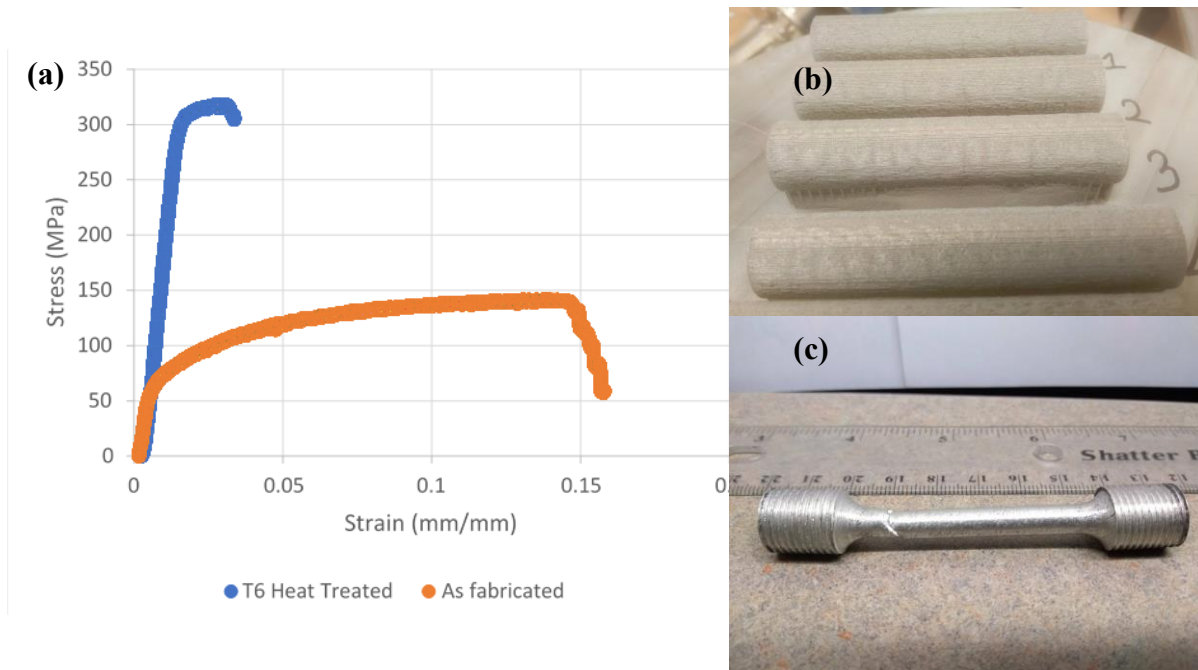


Figure 5.7 Representative stress-strain diagram of LPBF fabricated AA6061 specimens as fabricated and T6 heat treated. Figure 5.7(b) Solid cylinders built in X direction and still on build plate; tensile specimens were machined out of these cylinders. Figure 5.7(c) LPBF fabricated AA6061 tensile testing specimen after fractured

The as-fabricated, inductively-heated powder bed components were also subsequently heat treated to produce a T6 temper by solutionizing heat treatment at 520 °C for 50 min., water quenching, and aging at 210 °C for 50 min.; and cooling to room temperature (25 °C) at 3 C/min. This treatment produced a yield strength ~ 280 MPa, ultimate tensile strength of ~ 310 MPa, and an elongation of 3.5%. While the yield and ultimate tensile strength values were at the upper end of the T6 temper, the elongation was below the normal low of around 5% for this temper. Resulting tensile properties of the LPBF fabricated AA6061 are compared with that of wrought AA6061 in Table 3. Representative stress-strain diagrams for one tensile specimen of each type are shown in Figure 5.7(a). Figure 5.7(b) depicts solid cylinders built in the X direction that were machined as tensile specimens for monotonic tensile testing, and Figure 5.7(c) shows one of the tested

specimens after fracture. The yield strength and ultimate tensile strength of LPBF fabricated specimens were comparable to the corresponding properties of the wrought products. However, loss of ductility was noted in the LPBF fabricated specimens, which is expected to improve with further parameter optimization and process improvement.

As pointed out by Coniglio and Cross [121] and Rappaz, *et al.* [122], during solidification of aluminum alloys such as 6061, volumetric shrinkage and thermal conduction along columnar grains, especially, produces voids and associated hot cracking which spans the entire grain length as well as adjoining grain boundaries as shown typically in Figure 5.4. Martin, *et al.* [25] have recently demonstrated that cracking can be avoided in aluminum alloys by introducing nanoparticle nucleants to control solidification through grain refinement during LPBF fabrication. Here (Figure 5.5) we have demonstrated that by heating the powder bed during LPBF fabrication of AA6061 to reduce solidification undercooling, cracking is eliminated even for elongated grains in the build direction as well as a corresponding and essentially equiaxed grain structure in the plane perpendicular to the build direction (Figure 5.5); having a preferred [100] texture parallel and perpendicular to the build (solidification) direction (Figure 5.8). The large thermal conductivity as well as the high heats of fusion for aluminum alloys such as 6061 also contribute to the difficulty in achieving substantial undercooling, and powder bed heating significantly reduces these thermal barriers as well.

5.4.3 (ii) XRD

The XRD spectrum (Figure 5.8) as noted above, revealed a preferred grain texturization in (200) orientation in both the builds, with and without induction heating of the powder bed. The (200) direction was also dominant regardless of the build direction (vertical section) or the perpendicular to build direction (horizontal section). Although (200) was the preferred texture for

crystallographic orientation, a difference was observed in its texturing intensity between the builds with heated and unheated powder bed. In the unheated powder bed, the intensity of the peaks was

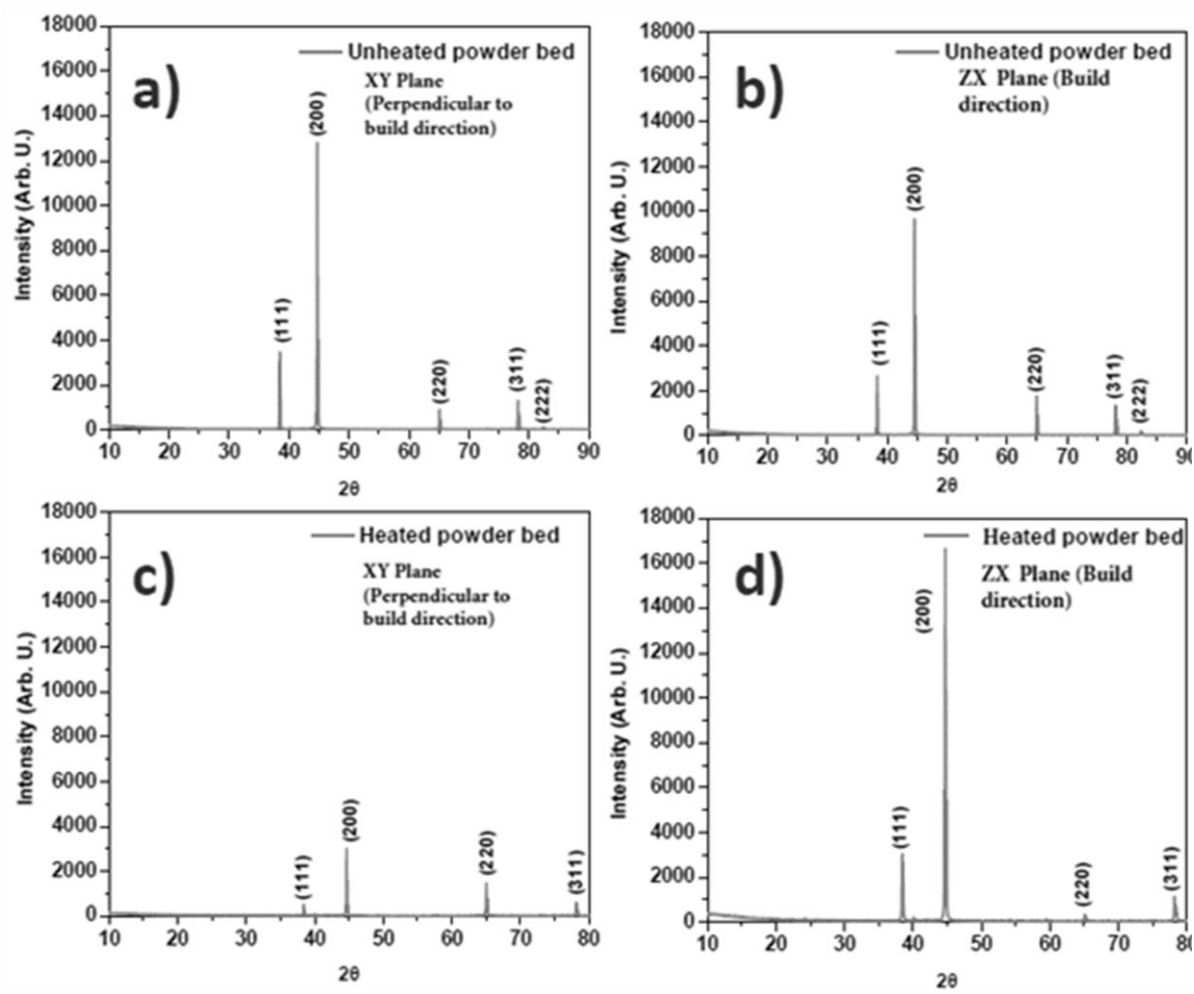


Figure 5.8 XRD spectra for AA6061 fabricated with and without heating of the powder

bed (a) and (b) show XRD spectra in unheated XY and ZX reference planes.

(c) and (d) show XRD spectra in heated XY and ZX reference plane.

similar in direction and intensity in the build direction and the perpendicular to build direction except for a slight suppression of the (220) plane in the build direction. Meanwhile a notable difference in texturing was observed between the horizontal and vertical section of the specimens built with powder bed heating. With the heated powder bed, the vertical section was strongly

textured with (200) planes whereas those planes were somewhat suppressed in the horizontal section. Such a texturing is attributed to the columnar grain growth in the build direction as shown in Figure 5.5., and characteristic of many other laser and electron beam fabricated metals and alloys [123].

5.5 Conclusion

In this study, AA6061 test coupons were fabricated using LPBF technology assisted with powder bed heating resulting in crack-free components. Crack-free fabrication of AA6061 has been a challenge for the AM community for some time. The use of powder bed heating during the fabrication process altered the thermodynamics such that cracking was prevented. Instead, columnar grain growth and large noncoherent precipitates (Al-Si-O) were observed in the microstructure while typical melt-pools and melt-track features characteristic of LPBF fabrication were eliminated. In addition, crack-free tensile specimens fabricated in the current study showed yield strength and ultimate tensile strength comparable to wrought AA6061 both in annealed and T6 heat treated conditions although with a reduced ductility. Unlike the prior work by Martin, *et al.* [15] where Zr nanoparticle nucleants were added to precursor AA6061 and other aluminum alloy powders, the present study eliminated solidification-associated cracking by high temperature heating of the powder bed. This may be a simpler and much more direct approach to reduce solidification undercooling in powder bed AM. With better understanding of the role of powder bed heating in combination with other processing parameters such as laser power, scanning speed, layer thickness and hatch spacing that dictate the size and shape of melt-pool, the current approach could be employed in LPBF fabrication of other crack susceptible alloys.

In summary, the contributions of this work include:

- Fabrication of crack-free and pure AA6061 using LPBF was demonstrated using high

temperature powder bed heating. The approach did not require nucleation or other alloy modifying aids but was solely achieved using powder bed preheating by means of an induction heater that enabled elevating the temperature of the bed during fabrication up to 1000 °C with a set point of 500 °C used for the crack-free AA6061 demonstration.

- The high temperature preheating of the powder bed resulted in removal of melt-pool banding that is traditionally associated with LPBF fabrication, and the nucleation of large noncoherent precipitates that were evident in the columnar grain boundaries of the produced material.
- The mechanical properties obtained for the AA6061 produced with this method were comparable to those of wrought AA6061, except for elongation at breakpoint.

In closing, the current study indicates that high temperature powder bed heating with modified processing conditions (i.e., laser power, scan speed, hatch spacing, layer thickness) can be influential in deterring crack formation in alloys with large solidification range such as AA6061. Research is ongoing to more completely understand the processing parameters that are responsible for crack formation during LPBF fabrication of highly crack susceptible alloys such as AA6061, leading to successful LPBF processing of these commonly used alloys for practical products.

Chapter 6: Results

This chapter includes the results from the study of metal powder emissivity inside a dental furnace modified for optical access when the temperature measurement was performed using a MW pyrometer and a thermocouple. The results of the research regarding difficult to process metallic materials using LPBF AM technology was presented in Chapter 5 under the title: Published Work - Crack-Free Aluminum 6061 Fabrication Demonstration.

Metal powders undergo different material states during laser powder bed fusion (LPBF) additive manufacturing (AM) process. These different material states could be identified as solid powder, liquid melt pool, and bulk metal after solidification. Emissivity of the metals at all these states vary from each other and therefore, poses a challenge in temperature measurement using pyrometers in which emissivity values are needed as input for accurate measurements. However, multiwavelength (MW) pyrometers would not require any prior information about the emissivity of the target and provide accurate temperature measurement along with a real-time emissivity value [76]. Such capability of MW pyrometers was explored in the current research to evaluate metal powder emissivity at different high temperatures with a view to establishing infrared (IR) thermography for LPBF processes monitoring in future. This development would help process control, process qualification and standardization by providing information about the thermal environment of the build. As well as using a commercially available MW pyrometer named FMPI SpectroPyrometer (FAR Associates, OH, USA), an in-house algorithm was also applied to calculate temperatures using the raw data stored in the instrument. Such development would open possibilities to design and fabricate MW pyrometers for dedicated application in LPBF process and subsequent use in IR thermography. The following sections describe the materials that were used for the study, measurements made using the setup and interpretation of results.

6.1 Materials Under Study

Four different metal powders, such as Ti-6Al-4V, AlSi10Mg, aluminum 6061 alloy (AA6061) and unalloyed copper (Cu) were used for the study. To determine the size distribution of these powders scanning electron microscopy (SEM) images were taken using a variable pressure tabletop microscope from Hitachi (TM1000, Hitachi, Ltd., Tokyo, Japan). A histogram of powder particle diameters as determined from those images revealed the particle size distribution of the materials. At least three different images were evaluated for each material. The SEM images also depicted the morphology of the powder materials.

Particle size distribution and SEM images of the Cu powder used for the study using are presented in Figure 6.1 (a) and Figure 6.1 (b), respectively. EPBF grade powders usually have a larger particle size distribution when compared to LPBF process. The EPBF grade Cu powder had a mean powder diameter of 70 μm with a slightly skewed normal distribution to the left of mean

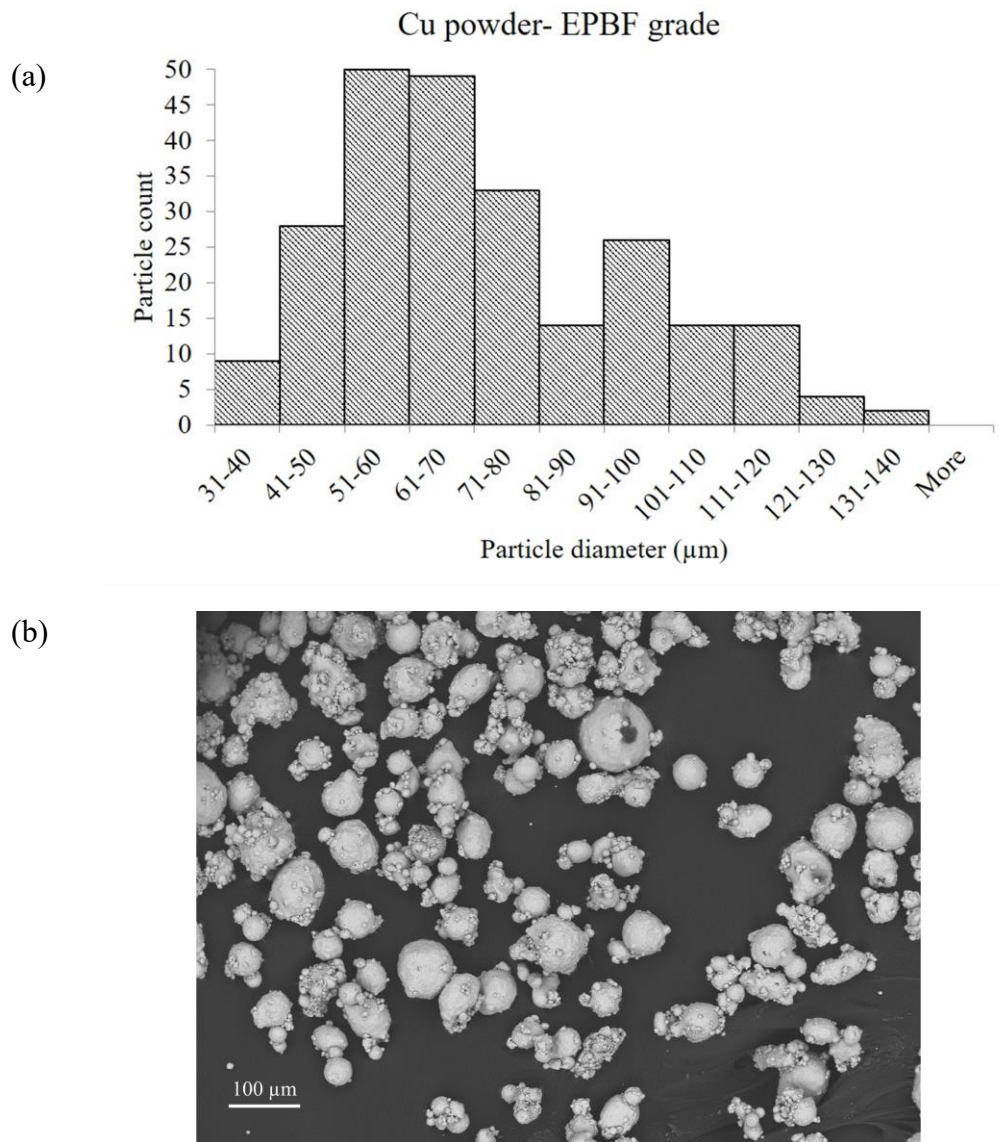


Figure 6.1 (a) Particle size distribution of Cu powder (b) SEM image of the Cu powder used for the current study showing spherical powder with a lot of satellites and

value. Frigola *et al.* [124] reported similar particle size distribution and morphology of Cu powder particles size intended for EPBF fabrication. According to Frigola *et al.* [124] it could be inferred that the abundance of satellites in Cu powder indicated gas atomization during fabrication of the batch. Powder particle size and morphology has strong implication in powder bed fusion AM processes since this property would dictate flowability of the powder, thermal conductivity and liquid metal flow in the melt pool [124]. Perhaps more important aspect of particle size distribution within the scope of this thesis is the effect of particle size distribution on temperature measurement that will be discussed in following sections. The current section will keep discussing the particle size distribution and morphology of Ti-6Al-4V powders.

Ti-6Al-4V powders with two different particle size distributions were used in the current study. The size distribution histogram and SEM images of the EPBF grade Ti-6Al-4V powder are shown in Figure 6.2 (a) and (b), respectively. This powder had a mean particle size of 53 μm and

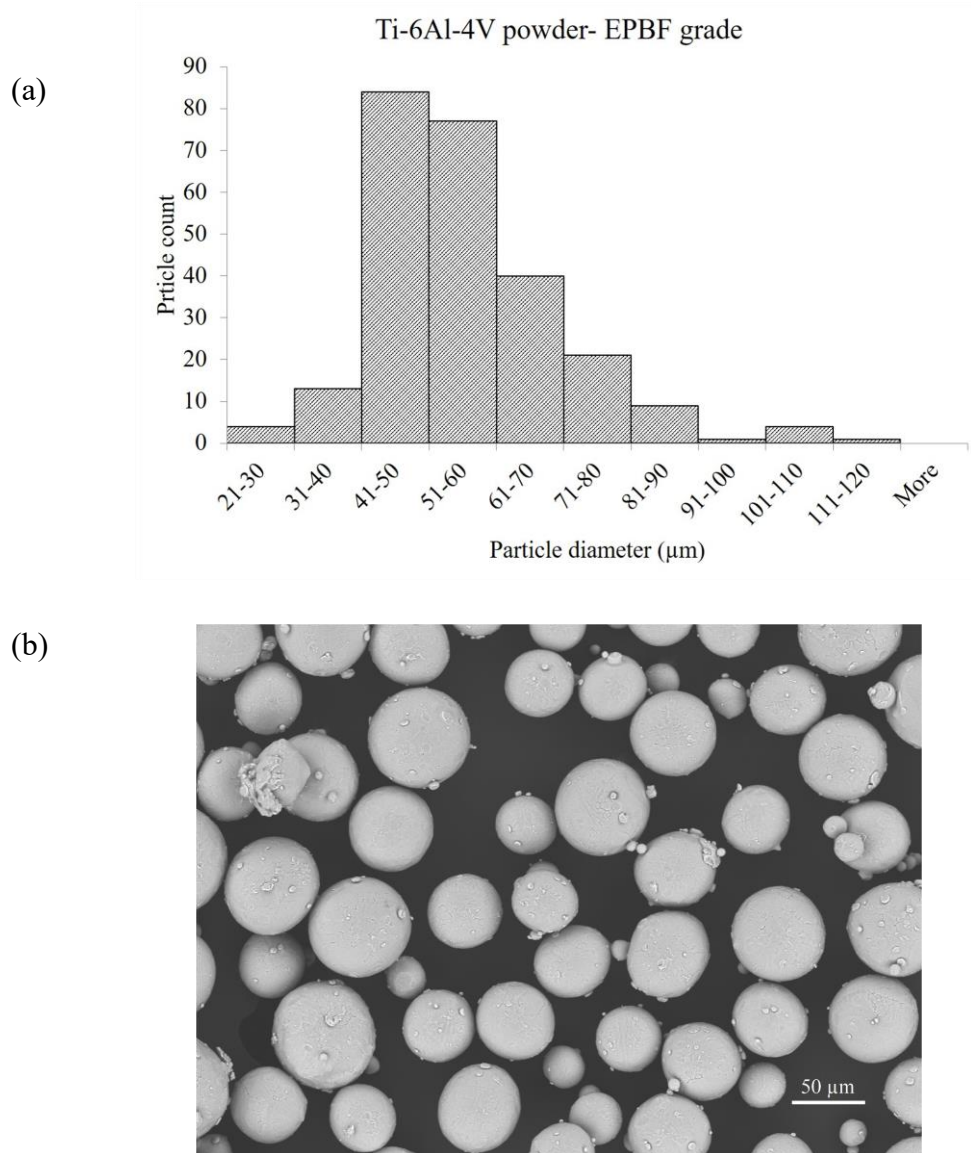


Figure 6.2 (a) Particle size distribution of Ti-6Al-4V powder of EBM grade (b) SEM image of the Ti-6Al-4V powder of EBM grade used for the current study showing spherical powder

a normal distribution around mean. Compared to the EPBF grade Cu powder, Ti-6Al-4V had a

smaller size distribution. Also, comparing SEM images of similar magnification it was observed that the Ti-6Al-4V powders had a lower number of satellites compared to the Cu powder. This

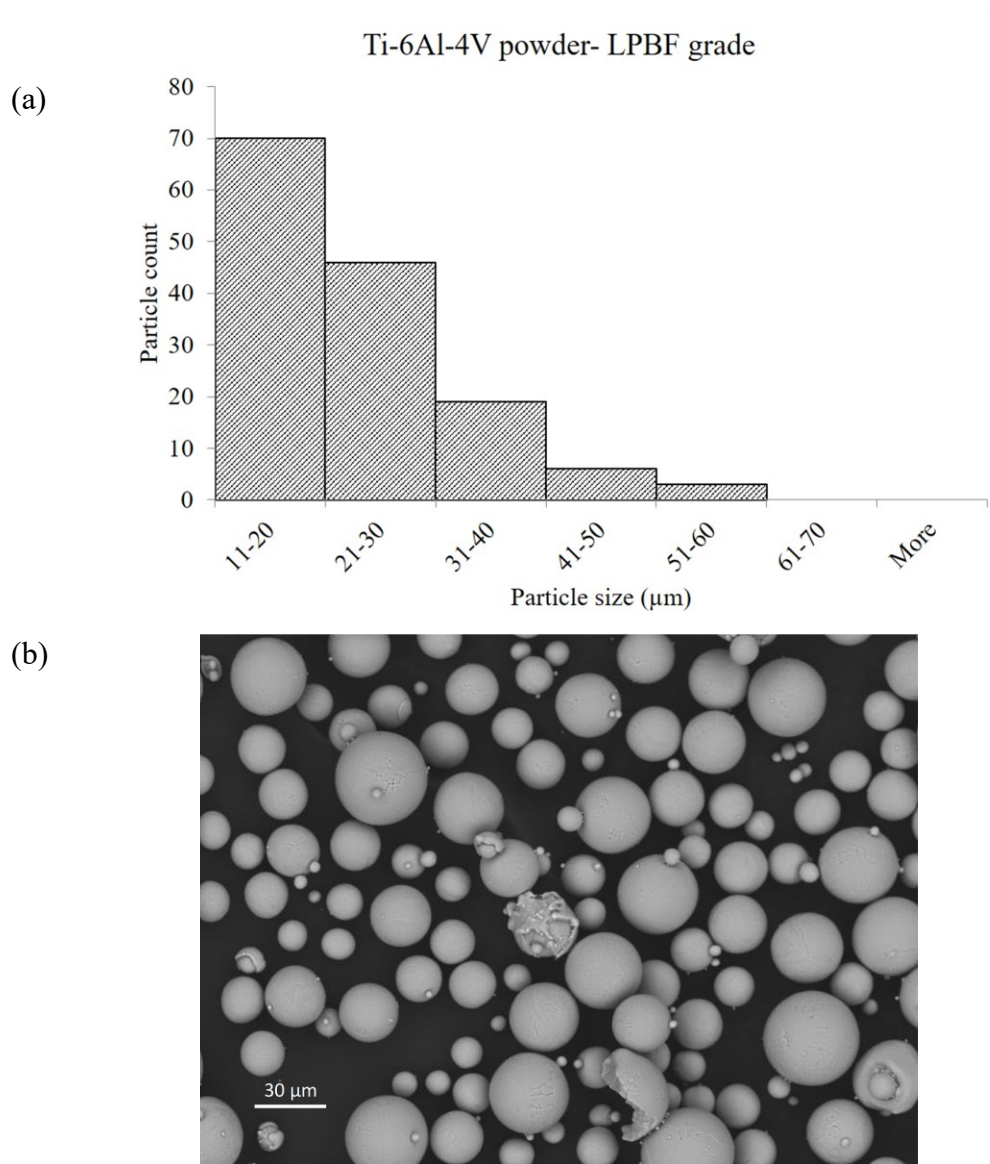


Figure 6.3 (a) Particle size distribution of Ti-6Al-4V powder of LPBF grade (b) SEM image of the Ti-6Al-4V powder of LPBF grade used for the current study showing mostly spherical powder with occasional satellite different in morphology will later be useful when the comparison of between emissivity is drawn.

The LPBF grade Ti-6Al-4V powder had a left-skewed powder particle distribution with a mean particle diameter of 20 μm . The particles were mostly spherical with occasional satellites as shown in Figure 6.3 (a) and (b).

6.2 Comparison of Measured Temperatures

Ti-6Al-4V powders with two different particle size distributions, EPBF grade Cu powder, AlSi10Mg of LPBF grade and AA6061 of LPBF grade were heated according to cycles presented in Table 6.1. All the materials were heated to the corresponding maximum temperature at a rate

Table 6.1 Material and operating condition. A ramp of 10 $^{\circ}\text{C}/\text{min}$ was used in all cases to heat up the material to the maximum temperature

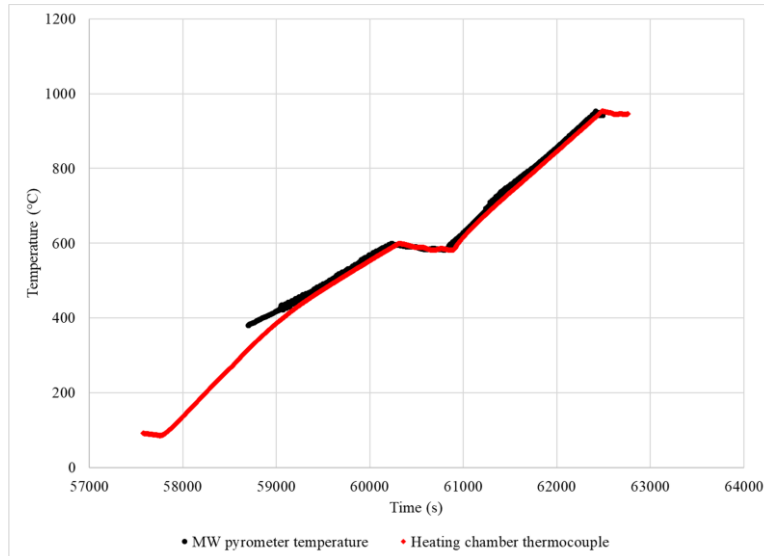
Material	Grade	Maximum temperature ($^{\circ}\text{C}$)	Environment
Ti-6Al-4V	EPBF	950	Argon
Ti-6Al-4V	LPBF	950	Argon
Cu	EPBF	950	Argon
AlSi10Mg	LPBF	600	Argon
AA6061	LPBF	600	Argon

of 10 $^{\circ}\text{C}/\text{min}$ and cooled back to room temperature in argon environment.

These temperatures were measured simultaneously using the pyrometer and chamber thermocouple. The MW pyrometer measured temperature on exposed surface of the powder held in the crucible and the thermocouple measured temperature amid air approximately half way down the height of the heating chamber. Location of measurements were shown in the pictures included in the description of the experimental section. The heating chamber inside the modified Whipmix Pro 200 furnace had the following dimensions, such as 3 3/4 W x 2 1/2 H x 3 3/4 D inches.

Figure 6.4 (a) and (b) shows a comparison between the temperature measurement obtained

(a)



(b)

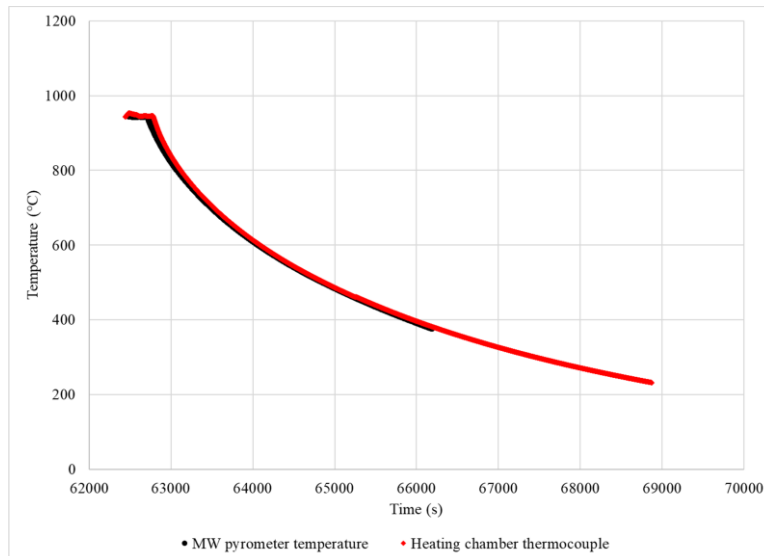


Figure 6.4 Comparison of temperature measured by the pyrometer and the thermocouple

when EBM grade Ti-6Al-4V was heated up to 950 °C Figure 6.4 (a) and (b)

demonstrates the comparison during heating up and cooling down, respectively

by the MW pyrometer and the heating chamber thermocouple. Data plotted in Figure 6.4 was obtained during experimentation with EBM grade Ti-6Al-4V powders in the furnace where the material was heated to approximately 950 °C and subsequently cooled down to room temperature

in argon environment. The superposition of the two curves during the heating, holding and cooling down stages as shown in Figure 6.4 (a) and (b) confirmed the following,

- i) thermal equilibrium was achieved inside the heating chamber for the maximum heating ramp of 10 °C/minute used for the experiments

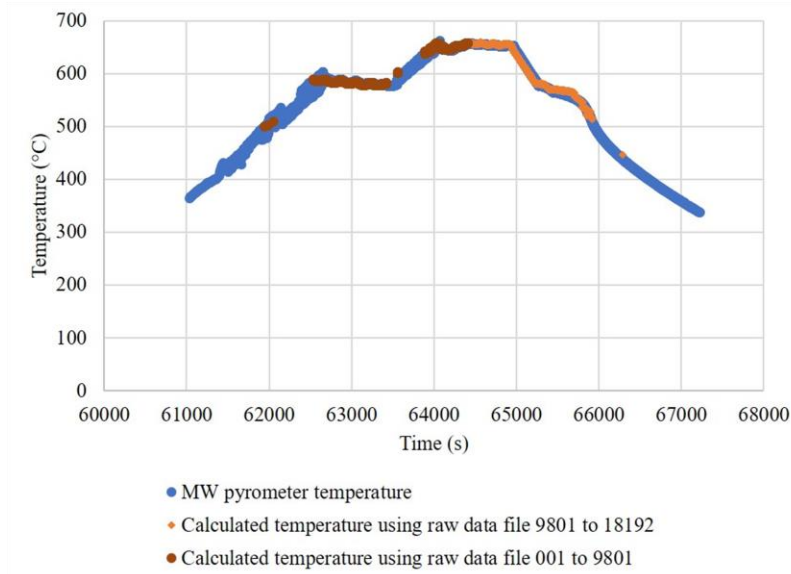


Figure 6.5 Comparison of measured temperature, that was obtained as an output from the MW pyrometer, with the temperature calculated by algorithm applied by the author

- ii) accuracy of the temperature measurements by MW pyrometer was maintained as the measured temperature was found to be within ± 3 °C of the heating chamber thermocouple

6.3 Demonstration of Temperature Calculation Using Intensity Data

The reliability of the data obtained using FMPI MW SpectroPyrometer was confirmed in the results shown in section 6.2 where the reading of the temperature matched within ± 3 °C of that of a K-type thermocouple, identified as ‘heating chamber thermocouple’. However, the MW

pyrometer only provided the output temperature and the emissivity without any demonstration of the methodology used for the calculating the temperature. For a better understanding of the measurement process and underlying principles of MW pyrometry, an in-house algorithm was applied to the intensity data stored by the instrument. Such endeavor could facilitate the design and fabrication of accurate temperature measurement instrument dedicated for the LPBF process. Following is a step by step demonstration of the calculation of temperature using a set of raw intensity data during the heating of AlSi10Mg in the modified furnace.

6.3.1 Understanding the .dat File

Every time an instance of measurement is made, the SpectroPyrometer creates a .dat file in the user designated folder; for the current case, the location of the .dat files were in the C drive of the computer connected to the pyrometer. For each temperature output, a unique data file is created. For example, given that during a measurement session of one minute, the instrument is set to log temperature output every one second, then 60 data points are expected out of that session of measurements. For each of these temperatures output a unique dat file, such as 001.dat, 002.dat, etc. up to 060.dat are created. Each of these data files contains the intensity values with corresponding wavelengths. The intensity values are in arbitrary units according to the factory calibration of the instrument. The .dat files contain no header. These files start with a single row of numbers and contain numerical values in nine columns. Starting with the second row, the data

is more structured in such a way that it has five columns in each row. According to the manual,

Table 6.2 Raw intensity data file i.e. .dat file obtained from the MW pyrometer after annotations

Unspecified first row	878.438	2875.55	2949.73	-611.05	- 2940335264 .083	2.056960	15.15000	30.25000	28.47353
Labels applied according to the manual	Wavelength (nm)		Uncorrected intensity		Background intensity		Corrected intensity		Exposure time (s)
	887.813		2018.52		2003.15		654.213		3.66E+08
	889.375		2000.8		1975.57		630.703		3.46E+08

these columns were identified with the labels mentioned in the following Table 6.2. These data files store intensity data for wavelengths values up to approximately 1650 nm in 2 nm resolution. For the calculation of temperature, wavelength data and the corrected intensity data from the above table are used.

6.3.2 Calculation of Temperature

To calculate the temperature, intensity values corresponding to wavelengths at 50 nm interval would be gathered together. For example, a data file named Temp6188.dat that was obtained during the heating of AlSi10Mg could be considered. During that session of measurements, a total of 18192 data files were created. Out of these data files, Temp6188.dat was chosen here for demonstration. According to the algorithm, the data file would be sub-divided in segments with wavelengths in the 50 nm interval, such as 850 nm, 900 nm, up to 1650 nm. Then ratio temperatures of these wavelength-intensity pair would be calculated using the formula given in equation 6.1.

$$T_{12} = \frac{C' \left(\frac{1}{\lambda_1} - \frac{1}{\lambda_2} \right)}{\ln R - 5 \ln \left(\frac{\lambda_2}{\lambda_1} \right)} \quad (6.1)$$

where, $R = \frac{I_1}{I_2}$ is the ratio of intensities at wavelengths λ_1 and λ_2 . $C' = 1.438 \times 10^7$ is an optical constant related to the instrument. In Table 6.3, schematic representation of the calculated ration

Table 6.3 Schematic matrix of calculated ratio temperatures using equation 6.1

Wavelength	λ_1	λ_2	λ_3	λ_4	λ_5	λ_6	λ_7	λ_8
λ_1	0	T_{12}	T_{13}	T_{14}	T_{15}	T_{16}	T_{17}	T_{18}
λ_2	0	0	T_{23}	T_{24}	T_{25}	T_{26}	T_{27}	T_{28}
λ_3	0	0	0	T_{34}	T_{35}	T_{36}	T_{37}	T_{38}
λ_4	0	0	0	0	T_{45}	T_{46}	T_{47}	T_{48}
λ_5	0	0	0	0	0	T_{56}	T_{57}	T_{58}
λ_6	0	0	0	0	0	0	T_{67}	T_{68}
λ_7	0	0	0	0	0	0	0	T_{78}

Table 6.4 Calculated ratio temperatures using equation 6.1 from data file ‘Temp6188.dat’

Wavelength (nm)	1200	1250	1300	1350	1400	1450	1500	1550	1600
1200	0	913.8	911.0	910.0	909.5	909.0	908.2	907.1	905.6
1250	0	0	908.0	907.8	907.8	907.5	906.8	905.6	904.0
1300	0	0	0	907.6	907.7	907.4	906.5	905.1	903.2
1350	0	0	0	0	907.8	907.2	906.0	904.3	902.1
1400	0	0	0	0	0	906.6	905.1	903.0	900.5
1450	0	0	0	0	0	0	903.4	901.0	898.2
1500	0	0	0	0	0	0	0	898.5	895.3
1600	0	0	0	0	0	0	0	0	891.9

temperature matrix was given and in Table 6.4 actual ratio temperature calculated according to the MATLAB® scripts given in appendix C was provide. For actual calculation the data file named ‘Temp6188.dat’ was used from the data set of AlSi10Mg heating experiment. The temperatures in Table 6.4 are in Kelvin. To find the unique temperature corresponding to the data file

‘Temp6188.dat’, average of all these temperatures were taken which was 905.3 K. The corresponding temperature in Celsius unit is found by subtracting 273 from the 905.3 K and doing so one would obtain 632.3 °C. The temperature output obtained from the SpectroPyrometer’s log was 628.2 °C. This is way all the calculated temperature was obtained.

Figure 6.5 shows a comparison between the temperature measured by the MW pyrometer and the calculated temperature from the raw data files. Calculation steps were also mentioned in Chapter 3 under section 3.5 and the MATLAB[®] scripts and functions used are presented in the appendix section of the thesis document. The data presented in the Figure 6.5 was obtained during the heating up to 650 °C and subsequent cooling of the AlSi10Mg powder inside the modified furnace explained in the experimental section 3.2.3. The main objective of this portion of the study was to develop capability for calculating the temperature using intensity data with the view that the algorithm could later be utilized in dedicated *in situ* monitoring instrument for LPBF AM process.

During the experiment the AlSi10Mg was heated to 650 °C from room temperature. The lowest temperature the FMPI SpectroPyrometer (FAR Associates, OH, USA) could measure was 350 °C. The reason that the instrument could only measure the temperature above 350 °C was due to the lack of radiance energy emitted from the target. Any target with a temperature lower than 350 °C would not radiate enough energy to be discerned from the background radiation. In addition, lower temperature would require longer exposure time which would compromise the speed of measurement. Therefore, experimental data for 1 hour and 40 minutes could be captured by the instrument as could be observed from the time axis in Figure 6.5 although the experiment went on for approximately 3 hours and 30 minutes. However, the region of interest i.e. the temperature during the heating and cooling stages were captured. During this period a total of

18192 data files were generated consisting of the intensity values for the wavelength range of 850 nm to 1650 nm. Data file 001 to 9800 represented the heating stage and the rest up to 18192 represented the cooling stage. As shown in the Figure 6.5, author's algorithm matched the instruments original algorithm better during the cool down stage than the heating up stage. Further study for an enhanced algorithm that would enable the development of a MW pyrometer system dedicated for metal AM processes is underway.

6.4 Emissivity Measurements of Different Powder Materials and Comparison

The furnace setup explained in section 3.2.3 was used for heating up different powder materials such as Ti-6Al-4V, Cu, AlSi10Mg, etc. Emissivity measurements of these powders were obtained using the SpectroPyrometer system. In Figure 6.6 and Figure 6.7, emissivity values obtained for the experiments with EPBF and LPBF grade Ti-6Al-4V were plotted against temperature for the heating and cooling steps of the thermal cycles, respectively.

It can be observed from Figure 6.6 that the emissivity of EPBF grade Ti-6Al-4V powder is greater than the emissivity of LPBF grade Ti-6Al-4V powders. It was determined in section 6.1 that the EPBF grade Ti-6Al-4V powder had a mean particle size of 53 μm whereas the LPBF grade Ti-6Al-4V powder had a mean particle size of 20 μm . Clearly the EPBF grade powder had a larger particle size distribution. Following from that information it could be argued that larger powder particles showed greater emissivity in the IR range of 850 nm to 1650 nm which was the measuring wavelength range of the MW pyrometer. Similar observations were made by Fletcher *et al.* [125] when working with coal particles of different size distributions; larger the particle size distribution more was the emissivity.

Interestingly, measured emissivity values were different for the heating and cooling stages of the thermal cycle as observed when Figure 6.6 Figure 6.7 were compared. Such observation

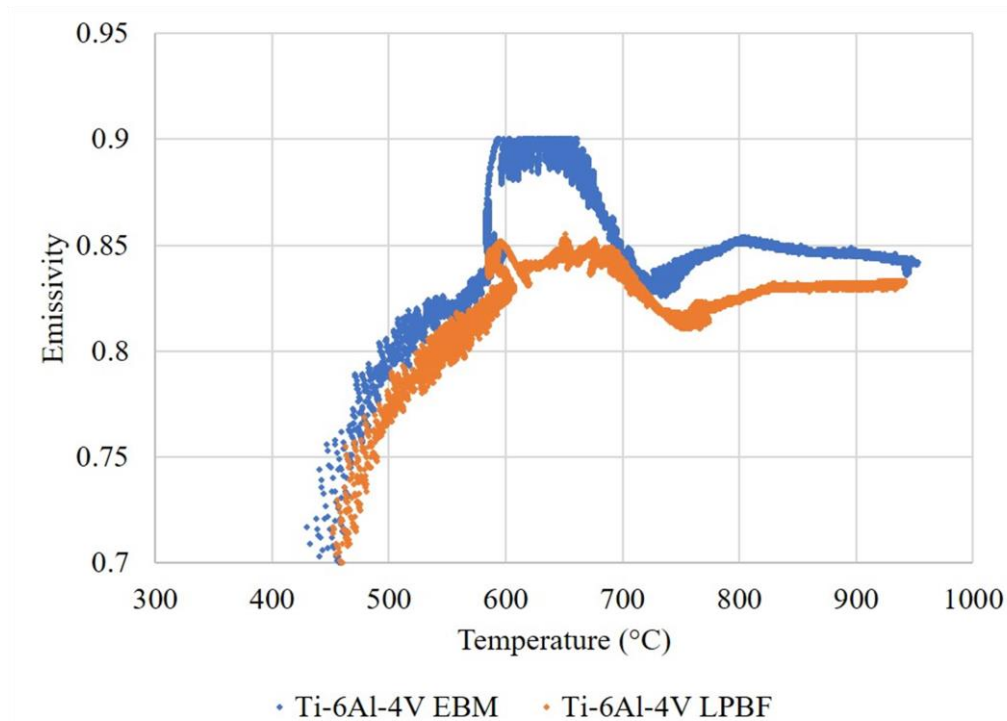


Figure 6.6 Change of emissivity with temperature during the heating of Ti-6Al-4V. Two different particle sizes, i.e. EPBF and LPBF grade powders were tested and compared

could be attributed to oxidation of the metal powder as evident from the change in powder color after the thermal cycles and XRD analysis on the samples afterwards where sharp peaks of TiO_2 was detected. During the heating up part of the thermal cycle, emissivity increased with temperature up to approximately 550 °C and remain in the range of 0.8 to 0.9 for the remaining heating and all of cooling stage. This variation of emissivity could be driven by several factors such as,

- i) change in temperature
- ii) change in chemical composition due to oxidation

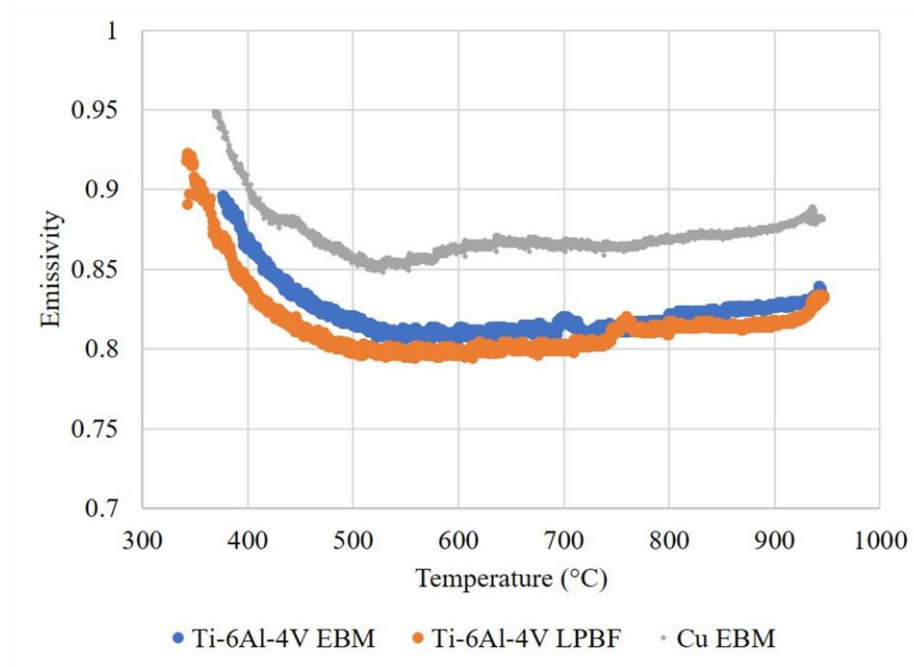


Figure 6.7 Change of emissivity with temperature during the cooling of Ti-6Al-4V. Two different particle sizes, i.e. EBM and LPBF grade Ti-6Al-4V powders and EBM powder with a different material i.e. copper powder were tested and compared. In an experimental study of emissivity of metal surfaces Li *et al.* [126] observed that emissivity of surfaces increased with oxidation and remained less affected by temperature change as more and more oxidation of the surface took place.

During the cool down stage, the emissivity of metal powders increased with decreasing temperature. Higher emissivity at lower temperatures were also observed by Sih *et al.* [127,128] for metal powder bed. On this note, the seemingly counterintuitive increase of emissivity with temperature during the heating of the powders could be explained by the

hypothesis that there could be multiple physicochemical phenomena driving the emissivity changes. One of them being the oxidation process happening during the heating process could overtake the dynamics of emissivity changes and surpass the effect of temperature on emissivity change, and thereby, resulting in overall increase in emissivity during heating up stage.

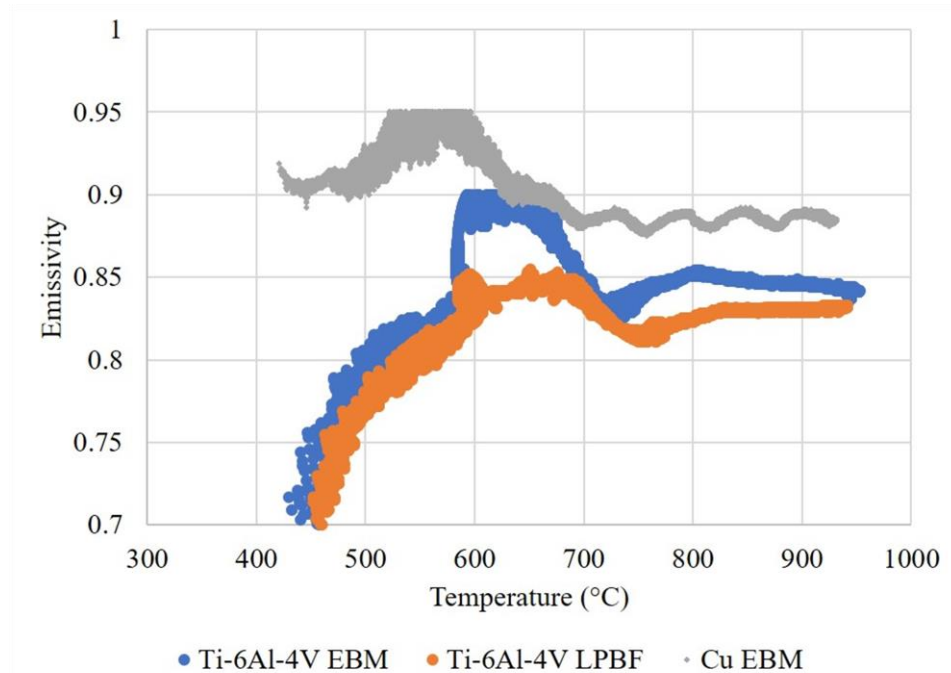


Figure 6.8 Change of emissivity with temperature during the heating of Ti-6Al-4V. Two different particle sizes, i.e. EBM and LPBF grade Ti-6Al-4V powders and a EBM powder with a different material i.e. copper powder were tested and compared

In comparison with EPBF and LPBF grade Ti-6Al-4V alloy powders, Cu powder showed greater emissivity during both, the heating and cooling stages as observed in Figure 6.7 and 6.8. One of the factors for Cu to show higher emissivity could be the different chemical compositions of the two materials. However as noted by Rozenbaum *et al.* [129] when studying the emissivity of alumina particles, the chemical composition alone could not determine the emissivity of a material, and surface morphology also influenced emissivity. Visual comparison of the SEM

images of the Cu and Ti-6Al-4V powder showed that Cu powder had more satellites than Ti-6Al-4V powder. Therefore, increased emissivity of the Cu powder could also be the result of this morphological feature. In addition, the satellites in Cu powder would increase the effective size of the powder particles as reported by Frigola *et al.* [124] which could also result in increased emissivity.

Emissivity of aluminum-based alloys such as AlSi10Mg and AA6061 powders were studied for emissivity. The general trend for emissivity variation during heating and cooling stages were maintained for these metallic materials, also. As shown in Figure 6.9, an increase in emissivity was observed during the cool-down stage.

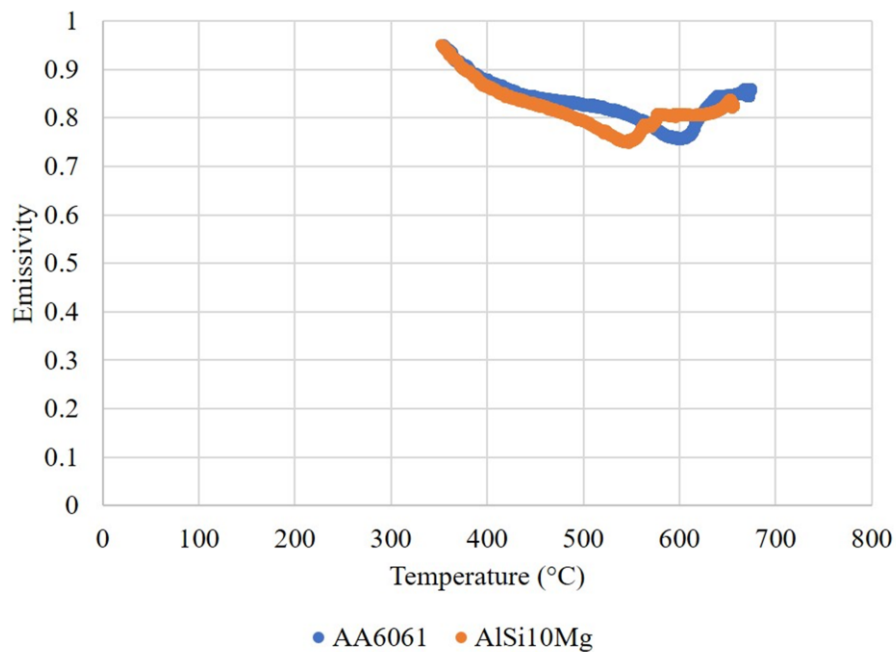


Figure 6.9 Comparison of emissivity of AA6061 and AlSi10Mg when cooled down from 650 °C to 350 °C

6.5 Results from in situ monitoring of AconityONE

One of the goals of studying emissivity of metal powders was to implement an *in situ* monitoring system for accurate surface temperature measurement in AconityONE machine. To achieve that the setup explained in section 3.4 was implemented. The measurements obtained

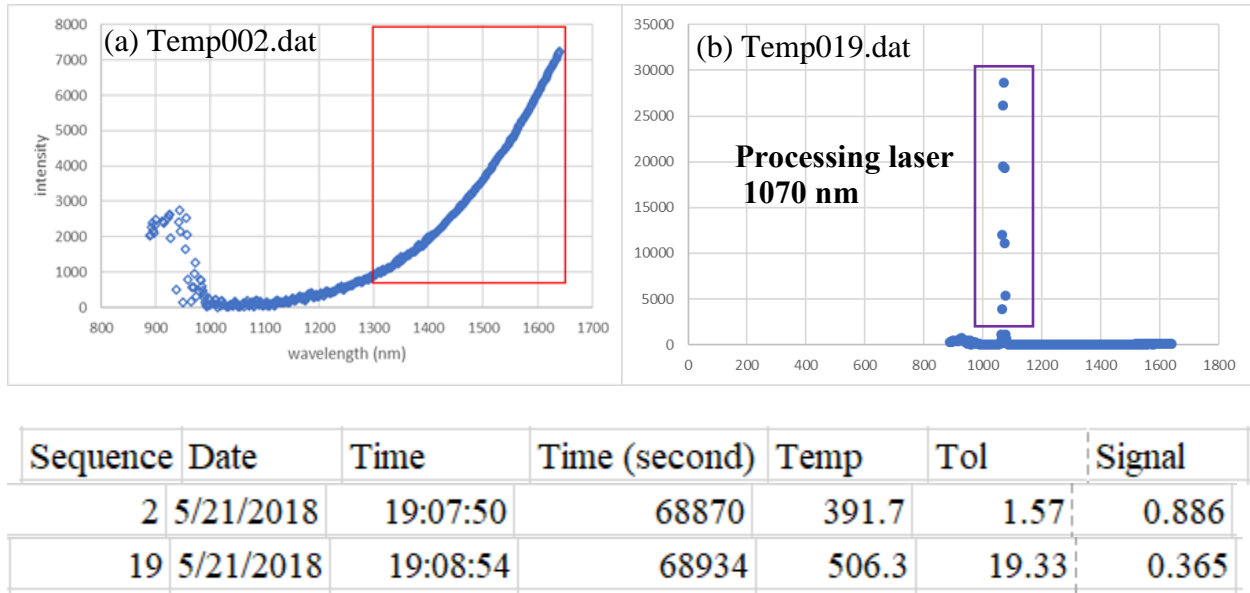


Figure 6.10 The two most typical data files obtained during the *in situ* MW pyrometer

measurement in AconityONE machine. The corresponding temperature outputs were given underneath the intensity graphs where high value of tolerance for the measurement affected with processing laser indicates lack of accuracy. The other measurement however captured the accurate surface temperature measured on a powder layer atop the pre-heated build plate

using the FMPI SpectroPyrometer (FAR Associates, OH, USA) during these *in situ* monitoring sessions consisted of two distinct intensity profiles in the near IR range of 850 nm to 1650 nm. For most of the measurements obtained, the intensity of the above-mentioned wavelengths resemble that of Figure 6.10. However, when the processing laser at 1070 nm operated, the high

intensity of the laser effectively ‘blinded’ or outweighed the thermal intensity and resulted in the intensity profile like that in Figure 6.10 (b). The temperature obtained using this intensity profile would therefore be inaccurate as rightly captured by a high tolerance value of 19.33 °C. These measurements show that the MW pyrometer could not only provide a measurement of accurate surface temperature, it also quantifies the accuracy of the measurement. Therefore, this technique of temperature measurement could be used in *in situ* monitoring of LPBF process after solving the processing laser intensity issue. Recommendations regarding the improvement of the system for such applications are provided in Chapter 7.

Chapter 7: Conclusions and Recommendations

7.1 Conclusions

An open architecture AconityONE LPBF system was used for crack free fabrication of AA6061 test coupons such as 10 mm³ cubes and tensile specimens. A commonly practiced approach of parameter modification such as experimentation with laser power, scan speed, hatch spacing, layer thickness, and powder bed heating was adopted to locate processing parameters so that crack would not occur. Use of high temperature powder bed heating could be useful for defect free fabrication of other crack prone metallic materials with similar solidification characteristics. Mechanical properties of the LPBF AM fabricated AA6061 specimens resembled that of the wrought counterparts except for a reduced ductility in the AM fabricated specimens. Enlarged precipitates were observed in the SEM images which could be a result of high temperature heating of the powder bed.

In situ measurements of the true surface temperature was deemed necessary to understand the changes in processing conditions resulting from the introduction of high temperature powder bed heating and its effect on the thermal environment of the build. A MW pyrometer system was used with modified and newly designed windows of AconityONE machine. Effect of processing laser of 1070 nm was detrimental to the temperature measurement using the MW pyrometer since the instrument had a measuring wavelength range of 850 nm to 1650 nm. A

To facilitate IR thermometry of the build area, knowledge of the emissivity of different segments of build area would be necessary. To measure and obtain emissivity profile of the metal powders, such as Ti-6Al-4V of two different size distributions, Cu, AlSi10Mg, and AA6061, a dental furnace was modified for optical access and controlled environment using argon flow and vacuum. The setup worked for the emissivity measurements, but the metallic materials heated

inside the heating chamber generally oxidized. A discussion on the tenacity of oxidation problem follows in section 7.2.1. In addition to the experimental set up for fundamental pyrometry, an algorithm to determine the temperature using intensity vs wavelength data was implemented which could be used for developing metal AM specific temperature measurement device after further improvement of the algorithm.

7.2 Recommendations for Future Work

In course of the projects that resulted in the current thesis, quite a few questions came along that could not be explored within the scope of this thesis. These unanswered questions can be formulated into future research endeavors and may result in findings worthwhile for the AM community. Following recommendation could be made based on the current study:

7.2.1 Use of High Temperature Powder Bed Heating

Use of high temperature powder bed fusion for metallic and ceramic materials can be explored in further detail. In particular, the processing of AA7075 and AA2024 using LPBF technology without the requirement for any pre-processing of the alloy, such as doping with crack deterrent foreign particle, would be of immense interest for the aerospace and automotive industry. These two alloys have solidification characteristic curves like AA6061, the observable crack free fabrication of which was demonstrated in this study. AA6061 has a range of applications, both in low cost products such as bicycle frames to high end application such as aerospace fuselage stringers. On the other hand, AA2024 and AA7075 are more specifically used in aerospace, marine and transportation industries due to their higher strengths compared to AA6061 [130]. Therefore, crack free LPBF fabrication process development of AA2024 and AA7075 might have greater industrial benefits. Since all these alloys have similar solidification characteristics, high

temperature powder bed heating could potentially solve the issue of crack formation during LPBF fabrication for all them.

In addition, development of methods for controlling the growth of precipitates beyond an acceptable limit can be pursued since such growth of precipitation could be detrimental to the fatigue properties of the parts produced using high temperature LPBF process.

7.2.2 Oxidation Problem

This issue could be analyzed from two broad perspectives relevant to the current thesis. Such as,

- i. oxidation of metal powders used in powder bed fusion (PBF) processes and corresponding manufacturing difficulty along with degradation of product quality
- ii. error in temperature measurement associated with the oxidized target i.e. LPBF powder in this case

Grell *et al.*[131] reported drastic loss of impact toughness of electron powder bed fusion (EPBF) products fabricated using a 3 wt% oxidized and 97% virgin Ti-6Al-4V powder. On the other hand, oxidation changes the emissivity of metal powder and alters temperature measurements. For example, as reported by Fletcher *et al.*[125], a dual wavelength pyrometer operating at 3 μm and 4 μm , overestimated the temperature of coal particles by 200 K i.e. when the accurate temperature would be 1500 K, the pyrometer measured 1700 K due to the emissivity variations at these wavelengths.

Oxidation of metal is a multi-physical phenomenon. It involves oxygen partial pressure, the chemical composition of the material, environment temperature, time, etc. as influencers only to name a few. Metal oxidation is not a high temperature phenomenon which is a common misunderstanding. There are two distinct types of oxidation process, high temperature process

that operates above 100 °C and low temperature process that operates below 100 °C for all the metals except the noble metals such as gold due to its low reactivity [132]. Therefore, realizing totally oxidation free process would be impractical. For example, in the testing condition of the current thesis, ultra-high purity (UHP) argon i.e. 99.9995% pure argon was introduced to the furnace at a pressure of 3 psi. Ideally, UHP argon is supposed to contain <1 ppm oxygen. Even that 1 ppm oxygen at 3 psi pressure would result in an oxygen partial pressure, P_{O_2} of 0.02 Pa [133]. Hitoshi *et al.* [134] reported oxidation of bulk iron at 573 K temperature with a P_{O_2} of 0.01 Pa. There two things to notice, one, powder materials have larger surface area than bulk materials, and two, Ti alloys are greater oxygen getters than iron. Therefore, metal powder oxidation is common.

With that acknowledgement, the following steps could be recommended to slow down the oxidation process during continuous high temperature exposure of metal powders,

- passing the UHP argon through tube furnaces containing Ti meshes at high temperature for further purification of the inert gas before introducing to the PBF process chamber
- reducing the number of external connections to the process chamber lest low pressure zone should be created around those pass throughs and air would be introduced to the system due to venturi effect

Before implementing the solution, quantification of the problem would be necessary. Therefore, oxygen analyzer should be used to determine the partial pressure of oxygen present in the furnace.

7.2.3 Establishing Temperature Mapping of Build Area in LPBF Process

Given that emissivity variation of metallic materials occurs with temperature, phase,

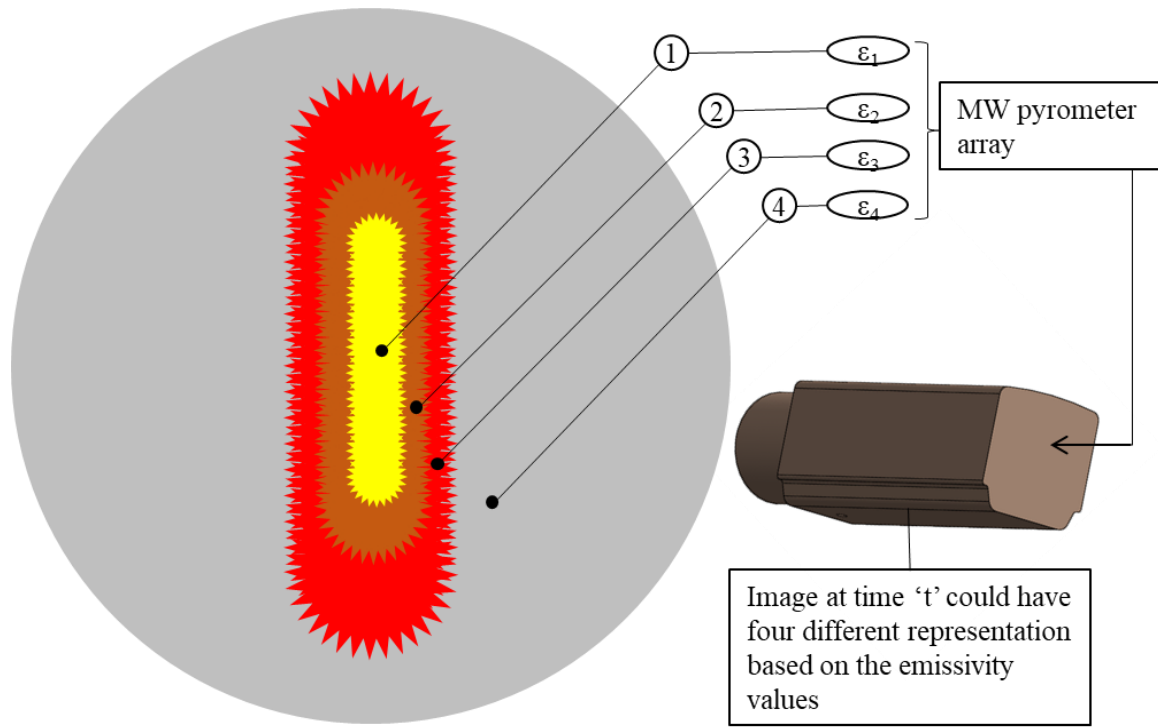


Figure 7.1 Laser-powder interaction occurs in zone 1. Zone 1, 2,3, and 4 could be different in phase and temperature and therefore differ in emissivity. To truly map the build area using an IR camera would require emissivity feedback from the MW pyrometer array

surface finish etc., establishing IR thermography to truly map the powder bed becomes even more challenging. One of the schemes could be to use a setup with the following components:

- i) equipment to measure emissivity of the powder bed at multiple spatial locations and
- ii) then use a single IR thermal camera with the available feedback of the emissivity values from those instruments

Figure 7.1 would explain the strategy with some more clarity. The image obtained using the thermal camera at any given time 't' would have four (could be more or less) different 'true' segments based on their emissivity status. In Figure 7.1, region 1 indicates the melt-pool track formed immediately upon the laser and powder bed interaction. Region 2 and 3 are high temperature zones affected by the melt-pool temperature. These zones could be solidified bulk material from last scan or un-melted hot powder receiving melt-pool heat by convection. Region 4 signifies a far field zone consisted of powder that is not within the heat affected zone. Depending on how the heat propagates from the melt-pool, region 2 and 3 could expand or shrink. The point is that all these regions would show different emissivity and knowledge of the emissivity of these regions would be necessary for accurate temperature mapping of the build area. Accurate temperature mapping of the build area would be helpful in process control, defect correction by implementing feedback control based on temperature fields and a universal measure of the quality of a build since temperature is a state property of material.

7.2.4 Removal of Laser Line from MW Pyrometer

The removal of the processing laser of 1070 nm would be necessary for accurate temperature measurement using the MW pyrometer. For this, a band rejection filter could be used in front of the SpectroPyrometer lens. The band rejection filter should be so chosen as to reject the a wavelength of ± 30 nm within 1070 nm to ensure that no laser intensity is detected by the MW pyrometer.

References

- [1] A.S. Chauhan, Tempo De Tromboplastina Parcial Ativado - Kptt Tempo De Protrombina - Tap, (2012) 10–12. doi:10.13140/RG.2.1.2600.9046.
- [2] F. Caiazzo, V. Alfieri, G. Corrado, P. Argenio, Laser powder-bed fusion of Inconel 718 to manufacture turbine blades, *Int. J. Adv. Manuf. Technol.* 93 (2017) 4023–4031. doi:10.1007/s00170-017-0839-3.
- [3] E. Louvis, P. Fox, C.J. Sutcliffe, Selective laser melting of aluminium components, *J. Mater. Process. Technol.* 211 (2011) 275–284. doi:10.1016/j.jmatprotec.2010.09.019.
- [4] L.E. Loh, Z.H. Liu, D.Q. Zhang, ... M.M.-V., Physical, undefined 2014, Selective Laser Melting of aluminium alloy using a uniform beam profile: The paper analyzes the results of laser scanning in Selective Laser Melting using a uniform, Taylor Fr. (n.d.). <http://www.tandfonline.com/doi/abs/10.1080/17452759.2013.869608>.
- [5] B.A. Fulcher, D.K. Leigh, T.J. Watt, Comparison of AlSi10Mg and Al 6061 Processed Through DMLS, *Proc. 25th Solid Free. Fabr. Symp.* (2014) 404–419.
- [6] W.S. Pellini, Strain theory of hot tearing, *Foundry.* 80 (1952).
- [7] K. Kempen, B. Vrancken, S. Bols, L. Thijs, J. Van Humbeeck, J.-P. Kruth, Selective Laser Melting of Crack-Free High Density M2 High Speed Steel Parts by Baseplate Preheating, *J. Manuf. Sci. Eng.* 136 (2014) 61026. doi:10.1115/1.4028513.
- [8] Standard Terminology for Additive Manufacturing—Coordinate Systems and Test Methodologies 1 D638 Test Method for Tensile Properties of Plastics E8/E8M Test

- Methods for Tension Testing of Metallic Materials F2792 Terminology for Additive Manufacturing Te, 52921 (2013).
- [9] International Organization for Standardization, ISO/ASTM 52900:2015 (ASTM F2792) Additive manufacturing -- General principles -- Terminology, (2015).
- [10] I. (Ian) Gibson, D.W. (David W.) Rosen, B. (Brent) Stucker, Additive manufacturing technologies : 3D printing, rapid prototyping and direct digital manufacturing, 2nd ed., Springer New York, New York, NY, n.d.
- [11] S.Z. Uddin, L.E. Murr, C.A. Terrazas, P. Morton, D.A. Roberson, R.B. Wicker, Processing and characterization of crack-free aluminum 6061 using high-temperature heating in laser powder bed fusion additive manufacturing, *Addit. Manuf.* 22 (2018) 405–415. doi:10.1016/J.ADDMA.2018.05.047.
- [12] J.R. Davis, Corrosion of Aluminum and Aluminum Alloys, ASM INTERNATIONAL, Ohio, 1991.
- [13] Y. Ding, J.A. Muñoz-Lerma, M. Trask, S. Chou, A. Walker, M. Brochu, Microstructure and mechanical property considerations in additive manufacturing of aluminum alloys, *MRS Bull.* 41 (2016) 745–751. doi:10.1557/mrs.2016.214.
- [14] D. Brackett, I. Ashcroft, R. Hague, Topology Optimization For Additive Manufacturing, in: *Solid Free. Fabr. Symp.*, Austin, TX, 2011: pp. 348–362.
- [15] C.E. Roberts, D. Bourell, T. Watt, J. Cohen, A Novel Processing Approach for Additive Manufacturing of Commercial Aluminum Alloys, *Phys. Procedia.* 83 (2016) 909–917.

doi:10.1016/j.phpro.2016.08.095.

- [16] C.E. Cross, On the Origin of Weld Solidification Cracking, in: Hot Crack. Phenom. Welds, Springer-Verlag, Berlin/Heidelberg, 2005: pp. 3–18. doi:10.1007/3-540-27460-X_1.
- [17] L. Katgerman, D.G. Eskin, In Search of the Prediction of Hot Cracking in Aluminium Alloys, in: Hot Crack. Phenom. Welds II, Springer Berlin Heidelberg, Berlin, Heidelberg, 2008: pp. 11–26. doi:10.1007/978-3-540-78628-3_1.
- [18] E. Cicală, G. Duffet, H. Andrzejewski, D. Grevey, S. Ignat, Hot cracking in Al–Mg–Si alloy laser welding – operating parameters and their effects, Mater. Sci. Eng. A. 395 (2005) 1–9. doi:10.1016/J.MSEA.2004.11.026.
- [19] T. Böllighaus, H. Herold, C. Cross, J.C. Lippold, Hot Cracking Phenomena in Welds II, 2008. doi:10.1017/CBO9781107415324.004.
- [20] S. Kou, A Simple Index for Predicting the Susceptibility to Solidification Cracking, Weld. J. 94 (2015) 374s–388s.
- [21] J.P. Bergmann, M. Bielenin, T. Feustel, Aluminum welding by combining a diode laser with a pulsed Nd:YAG laser, Weld. World. 59 (2015) 307–315. doi:10.1007/s40194-014-0218-8.
- [22] A. El-Batahy, M. Kutsuna, Laser Beam Welding of AA5052, AA5083, and AA6061 Aluminum Alloys, Adv. Mater. Sci. Eng. 2009 (2009) 1–9. doi:10.1155/2009/974182.
- [23] L.E. Loh, C.K. Chua, W.Y. Yeong, J. Song, M.M.-I.J. of ..., U. 2015, Numerical investigation and an effective modelling on the Selective Laser Melting (SLM) process with

aluminium alloy 6061, Elsevier. (n.d.).

- [24] L.E. Loh, Z.H. Liu, D.Q. Zhang, M. Mapar, S.L. Sing, C.K. Chua, W.Y. Yeong, Selective Laser Melting of aluminium alloy using a uniform beam profile, *Virtual Phys. Prototyp.* 9 (2014) 11–16. doi:10.1080/17452759.2013.869608.
- [25] J.H. Martin, B.D. Yahata, J.M. Hundley, J.A. Mayer, T.A. Schaedler, T.M. Pollock, 3D printing of high-strength aluminium alloys, *Nature.* 549 (2017) 365–369. doi:10.1038/nature23894.
- [26] H. Ali, L. Ma, H. Ghadbeigi, K. Mumtaz, In-situ residual stress reduction, martensitic decomposition and mechanical properties enhancement through high temperature powder bed pre-heating of Selective Laser Melted Ti6Al4V, *Mater. Sci. Eng. A.* 695 (2017) 211–220. doi:10.1016/j.msea.2017.04.033.
- [27] D. Buchbinder, W. Meiners, N. Pirch, K. Wissenbach, J. Schrage, Investigation on reducing distortion by preheating during manufacture of aluminum components using selective laser melting, *J. Laser Appl.* 26 (2014) 12004. doi:10.2351/1.4828755.
- [28] C. V. Sternling, L.E. Scriven, Interfacial turbulence: Hydrodynamic instability and the marangoni effect, *AIChE J.* 5 (1959) 514–523. doi:10.1002/aic.690050421.
- [29] S.-H. Hu, J.-J. Yan, J.-S. Wang, Y. Li, J.-P. Liu, Effect of temperature gradient on Marangoni condensation heat transfer for ethanol–water mixtures, *Int. J. Multiph. Flow.* 33 (2007) 935–947. doi:10.1016/J.IJMULTIPHASEFLOW.2007.03.005.
- [30] K.C. Mills, B.J. Keene, R.F. Brooks, A. Shirali, Marangoni effects in welding, *Philos.*

- Trans. R. Soc. A Math. Phys. Eng. Sci. 356 (1998) 911–925. doi:10.1098/rsta.1998.0196.
- [31] C.R. Heiple, J.R. Roper, R.T. Stagner, R.J. Aden, Surface active element effects on the shape of GTA, laser and electron beam welds, *Weld. J.* 62 (1983) 72.
- [32] P.D. Lee, P.N. Quested, M. McLean, Modelling of Marangoni effects in electron beam melting, *Philos. Trans. R. Soc. A Math. Phys. Eng. Sci.* 356 (1998) 1027–1043. doi:10.1098/rsta.1998.0207.
- [33] K. Antony, N. Arivazhagan, STUDIES ON ENERGY PENETRATION AND MARANGONI EFFECT DURING LASER MELTING PROCESS, 2015. <http://jestec.taylors.edu.my/Vol>.
- [34] S.A. Khairallah, A.T. Anderson, A. Rubenchik, W.E. King, Laser powder-bed fusion additive manufacturing: physics of complex melt flow and formation mechanisms of pores, spatter, and denudation zones, n.d. <https://arxiv.org/ftp/arxiv/papers/1512/1512.02593.pdf>.
- [35] C. Qiu, C. Panwisawas, M. Ward, H.C. Basoalto, J.W. Brooks, M.M. Attallah, On the role of melt flow into the surface structure and porosity development during selective laser melting, *Acta Mater.* 96 (2015) 72–79. doi:10.1016/J.ACTAMAT.2015.06.004.
- [36] T. Mukherjee, V. Manvatkar, A. De, T. DebRoy, Dimensionless numbers in additive manufacturing, *J. Appl. Phys.* 121 (2017). doi:10.1063/1.4976006.
- [37] COMSOL Multiphysics, The Marangoni effect, (2018). <https://www.comsol.com/multiphysics/marangoni-effect> (accessed September 25, 2018).
- [38] P.S. Wei, C.N. Ting, J.S. Yeh, T. Debroy, F.K. Chung, G.H. Yan, Origin of wavy weld

- boundary, *J. Appl. Phys.* 105 (2009). doi:10.1063/1.3065533.
- [39] K. Jurrens, National Institute of Standard and Technology, Measurement Science Roadmap for Metal-Based Additive Manufacturing, 2013.
- [40] AM Steering Group UK, The Case for Additive Manufacturing, 2015. <http://www.amnationalstrategy.uk/wp-content/uploads/2015/05/AM-Strategy-Positioning-Paper.pdf>.
- [41] S. Berumen, F. Bechmann, S. Lindner, J.-P. Kruth, T. Craeghs, Quality control of laser- and powder bed-based Additive Manufacturing (AM) technologies, *Phys. Procedia*. 5 (2010) 617–622. doi:10.1016/j.phpro.2010.08.089.
- [42] P. Lott, H. Schleifenbaum, W. Meiners, K. Wissenbach, C. Hinke, J. Bültmann, Design of an optical system for the in situ process monitoring of Selective Laser Melting (SLM), *Phys. Procedia*. 12 (2011) 683–690. doi:10.1016/j.phpro.2011.03.085.
- [43] S. Clijsters, T. Craeghs, S. Buls, K. Kempen, J.P. Kruth, In situ quality control of the selective laser melting process using a high-speed, real-time melt pool monitoring system, *Int. J. Adv. Manuf. Technol.* 75 (2014) 1089–1101. doi:10.1007/s00170-014-6214-8.
- [44] M. Doubenskaia, M. Pavlov, Y. Chivel, Optical System for On-Line Monitoring and Temperature Control in Selective Laser Melting Technology, *Key Eng. Mater.* 437 (2010) 458–461. doi:10.4028/www.scientific.net/KEM.437.458.
- [45] T. Furumoto, T. Ueda, N. Kobayashi, A. Yassin, A. Hosokawa, S. Abe, Study on laser consolidation of metal powder with Yb: fiber laser-Evaluation of line consolidation

- structure, *J. Mater. Process. Technol.* 209 (2009) 5973–5980.
doi:10.1016/j.jmatprotec.2009.07.017.
- [46] M.B. Ignatiev, I.Y. Smurov, G. Flamant, V.N. Senchenko, Surface temperature measurements during pulsed laser action on metallic and ceramic materials, *Appl. Surf. Sci.* 96–98 (1996) 505–512. doi:10.1016/0169-4332(95)00504-8.
- [47] T. Furumoto, M.R. Alkahari, T. Ueda, M.S.A. Aziz, A. Hosokawa, Monitoring of Laser Consolidation Process of Metal Powder with High Speed Video Camera, *Phys. Procedia.* 39 (2012) 760–766. doi:10.1016/j.phpro.2012.10.098.
- [48] T. Furumoto, T. Ueda, M.R. Alkahari, A. Hosokawa, Investigation of laser consolidation process for metal powder by two-color pyrometer and high-speed video camera, *CIRP Ann. - Manuf. Technol.* 62 (2013) 223–226. doi:10.1016/j.cirp.2013.03.032.
- [49] Y.N. Zavalov, A. V Dubrov, V.D. Dubrov, F.K. Mirzade, V.N. Glebov, A.M. Malutin, P.S. Rodin, The multichannel pyrometer of the spectral ratio for on-line monitoring in the powder bed additive technologies, *Unconv. Opt. Imaging.* (2018) 89. doi:10.1117/12.2307578.
- [50] M. Montazeri, P. Rao, Sensor-Based Build Condition Monitoring in Laser Powder Bed Fusion Additive Manufacturing Process Using a Spectral Graph Theoretic Approach, *J. Manuf. Sci. Eng.* 140 (2018) 091002. doi:10.1115/1.4040264.
- [51] F. Imani, A. Gaikwad, M. Montazeri, P. Rao, H. Yang, E.W. Reutzel, Layerwise in-process quality monitoring in laser powder bed fusion, *ASME 2018 13th Int. Manuf. Sci. Eng. Conf.* (2018) 1–14.

- [52] B. Yuan, G.M. Guss, A.C. Wilson, S.P. Hau-Riege, P.J. DePond, S. McMains, M.J. Matthews, B. Giera, Machine-Learning-Based Monitoring of Laser Powder Bed Fusion, *Adv. Mater. Technol.* 1800136 (2018) 1800136. doi:10.1002/admt.201800136.
- [53] A.J. Dunbar, A.R. Nassar, Assessment of optical emission analysis for in-process monitoring of powder bed fusion additive manufacturing, *Virtual Phys. Prototyp.* 13 (2018) 14–19. doi:10.1080/17452759.2017.1392683.
- [54] C.L.A. Leung, S. Marussi, R.C. Atwood, M. Towrie, P.J. Withers, P.D. Lee, In situ X-ray imaging of defect and molten pool dynamics in laser additive manufacturing, *Nat. Commun.* 9 (2018) 1–9. doi:10.1038/s41467-018-03734-7.
- [55] Aconity3D GmbH, Process parameters, 2018. (n.d.).
- [56] 3-AXIS DEFLECTION UNITS, (n.d.).
- [57] FAR Associates, FMPI SpectroPyrometer Operating Manual, (2012).
- [58] R.A. Felice, United States Patent U . S . Patent, 1 (1980) 0–9. doi:10.1057/9780230607156.
- [59] C. Zhao, K. Fezzaa, R.W. Cunningham, H. Wen, F. De Carlo, L. Chen, A.D. Rollett, T. Sun, Real-time monitoring of laser powder bed fusion process using high-speed X-ray imaging and diffraction OPEN, (n.d.). doi:10.1038/s41598-017-03761-2.
- [60] M.A. Khan, C. Allemand, T.W. Eagar, Noncontact temperature measurement. I. Interpolation based techniques, *Rev. Sci. Instrum.* 62 (1991) 392–402. doi:10.1063/1.1142133.
- [61] M. Akhloufi, A. Bendada, Fusion of active and passive infrared images for face recognition,

Proc. SPIE - Int. Soc. Opt. Eng. 8705 (2013) 87050B.

- [62] J.M. L. Michalski, K. Eckersdorf, J. Kucharski, Temperature Measurement, 2002. doi:10.1002/0470846135.
- [63] M. Planck, On the law of distribution of energy in the normal spectrum, Ann. Phys. 4 (1901) 1.
- [64] W. Wien, Ueber die Energievertheilung im Emissionsspectrum eines schwarzen Körpers, Ann. Der Phys. Und Chemie. 294 (1896) 662–669. doi:10.1002/andp.18962940803.
- [65] Keller ITS, Intensity Comparison Pyrometer Mikro Type PV 11, (n.d.) 11–14.
- [66] D. Lardner, Treatise on heat, Printed for Longman, Rees, Orme, Brown, Green & Longman, 1833.
- [67] W.E. Forsythe, Color match and spectral distribution, JOSA. 7 (1923) 1115–1121.
- [68] H.W. Russell, OPTICAL PYROMETER, (1941).
- [69] G. Ribaud, Traité de pyrométrie optique: Encyclopédie photométrique, Ed. dl Revue d'Opt. théor. et instr, 1931.
- [70] I. Bonefačić, – P Blečić, TWO-COLOR TEMPERATURE MEASUREMENT METHOD USING BPW34 PIN PHOTODIODES, Eng. Rev. 35 (2015) 259–266. <https://pdfs.semanticscholar.org/9a90/2514633b8987ac6d5506e6c61d939487e35e.pdf>.
- [71] J.H. Bach, P.J. Street, C.S. Twamley, Temperature measurement of particulate surfaces, J. Phys. E. 3 (1970) 281–286. doi:10.1088/0022-3735/3/4/308.

- [72] B. Müller, U. Renz, Development of a fast fiber-optic two-color pyrometer for the temperature measurement of surfaces with varying emissivities, *Rev. Sci. Instrum.* 72 (2001) 3366–3374. doi:10.1063/1.1384448.
- [73] X. Xu, C.P. Grigoropoulos, R.E. Russo, Nanosecond-time-resolution thermal emission measurement during pulsed excimer-laser interaction with materials, *Appl. Phys. A Mater. Sci. Process.* 62 (1996) 51–59. doi:10.1007/BF01568087.
- [74] M.A. Khan, C. Allemand, T.W. Eagar, Noncontact temperature measurement. II. Least squares based techniques, *Rev. Sci. Instrum.* 62 (1991) 403–409. doi:10.1063/1.1142134.
- [75] P.B. Coates, Multi-Wavelength Pyrometry, *Metrologia.* 17 (1981) 103–109. doi:10.1088/0026-1394/17/3/006.
- [76] M. Pyrometer, R.A. Felice, The Spectropyrometer – a Practical, *Meas. Control.* 7 (2002).
- [77] Ralph A. Felice, Temperature determining device and process, (1998).
- [78] G. Ruffino, High-speed radiation pyrometry, *High Temp.-High Press.* 8 (1976) 143–154.
- [79] F.R.A. Jorgensen, M. Zuiderwyk, Two-colour pyrometer measurement of the temperature of individual combusting particles, *J. Phys. E.* 18 (1985) 486–491. doi:10.1088/0022-3735/18/6/006.
- [80] J.-P. Hiernaut, R. Beukers, W. Heinz, R. Selfslag, M. Hoch, R.W. Ohse, Submillisecond six-wavelength pyrometer for high-temperature measurements in the range 2000 to 5000 K, *High Temp. High Press.* 18 (1986) 617–625.
- [81] A. Cezairliyan, R.F. Chang, G.M. Foley, A.P. Miiller, High-speed spatial scanning

- pyrometer, *Rev. Sci. Instrum.* 64 (1993) 1584–1592. doi:10.1063/1.1144030.
- [82] P.M. Cordero, J. Mireles, S. Ridwan, R.B. Wicker, Evaluation of monitoring methods for electron beam melting powder bed fusion additive manufacturing technology, *Prog. Addit. Manuf.* 2 (2017) 1–10. doi:10.1007/s40964-016-0015-6.
- [83] K.-D. Gruner, K. De, Principles of Non-Contact Temperature Measurement, (n.d.). http://support.fluke.com/raytek-sales/Download/Asset/IR_THEORY_55514_ENG_REVB_LR.PDF.
- [84] G. Geutler, J. Krochmann, K.D. Reibmann, K. Steglich, Über eine Anordnung zur genauen Messung von Reflexionsgrad und Transmission-grad, *Optik (Stuttg.)* 54 (1980) 397–408.
- [85] A. Rogalski, Infrared detectors: an overview, *Infrared Phys. Technol.* 43 (2002) 187–210. doi:10.1016/S1350-4495(02)00140-8.
- [86] S. Ioannou, Ebisch, S. J., Aureli, T., Bafunno, D., Cardone, D., Ioannou, S., Romani, G. L., Gallese, V. and Merla, A. (2013). Mother and child in synchrony: thermal facial imprints of autonomic contagion. *Thermology International*, 22, (3), 121–129., 2013.
- [87] P.L. Richards, Bolometers for infrared and millimeter waves, *J. Appl. Phys.* 76 (1994) 1–24. doi:10.1063/1.357128.
- [88] S.T. Liu, D. Long, Pyroelectric detectors and materials, *Proc. IEEE*. 66 (1978) 14–26.
- [89] A. Einstein, Concerning an heuristic point of view toward the emission and transformation of light, *Am. J. Phys.* 33 (1965) 367.
- [90] R.A. Millikan, On the elementary electrical charge and the Avogadro constant, *Phys. Rev.*

- 2 (1913) 109.
- [91] N. Davidson, Measurement and Detection of Radiation by N. Tsoulfanidis, *Med. Phys.* 11 (1984) 732. doi:10.1118/1.595625.
- [92] J. Saghaei, A. Fallahzadeh, T. Saghaei, Vapor treatment as a new method for photocurrent enhancement of UV photodetectors based on ZnO nanorods, *Sensors Actuators A Phys.* 247 (2016) 150–155. doi:10.1016/J.SNA.2016.05.050.
- [93] J.F. Cox, *Fundamentals of linear electronics: integrated and discrete*, Cengage Learning, 2002.
- [94] W.S. Boyle, G.E. Smith, Charge Coupled Semiconductor Devices, *Bell Syst. Tech. J.* 49 (1970) 587–593. doi:10.1002/j.1538-7305.1970.tb01790.x.
- [95] W. Budde, *Physical Detectors of Optical Radiation, Optical Radiation Measurements*, Vol. 4, (1983).
- [96] Vigo Systems S.A., *Catalogue of photodetectors*, (n.d.).
- [97] G.J. Snyder, E.S. Toberer, Complex thermoelectric materials, *Nat. Mater.* 7 (2008) 105.
- [98] A. Rogalski, GaAs/AlGaAs QWIPs vs HgCdTe Photodiodes for LWIR Applications, in: *Quantum Well Intersubband Transit. Phys. Devices*, Springer Netherlands, Dordrecht, 1994: pp. 87–96. doi:10.1007/978-94-011-1144-7_7.
- [99] J. Wieser, C. Constantin, E. Dewald, J. Jacoby, S. Udrea, D. Varentsov, *Optical Beam Diagnostics*, (n.d.). http://webdoc.sub.gwdg.de/ebook/rd/2001/gsi/www-aix.gsi.de/annual_report/ann_rep/plasma/22/jb2000.pdf.

- [100] Alluxa, What are thin-film optical filters?, (n.d.).
- [101] Sylavania, Frequently asked questions in general lighting, (2005) 1–2.
- [102] National Communications System, Federal Standard 1037C, (n.d.).
- [103] D. Seyringer, Arrayed waveguide gratings, in: SPIE, 2016.
- [104] M.R. Amersfoort, Phased-array wavelength demultiplexers and their integration with photodetectors, Delft University, 1994.
- [105] J.R. Howell, M.P. Menguc, R. Siegel, Thermal radiation heat transfer, CRC press, 2010.
- [106] J.M. Senior, M.Y. Jamro, Optical Fiber Communications: Principles and Practice, 2009. doi:10.1080/716099703.
- [107] Standard Test Method for Apparent Density of Free-Flowing Metal Powders Using the Hall Flowmeter Funnel 1, (n.d.). doi:10.1520/B0212-17.
- [108] Standard Test Methods for Flow Rate of Metal Powders Using the Hall Flowmeter Funnel 1, (n.d.). doi:10.1520/B0213-17.
- [109] P. Ponnusamy, S.H. Masood, D. Ruan, S. Palanisamy, O.A. Mohamed, Statistical analysis of porosity of 17-4PH alloy processed by selective laser melting, (n.d.). doi:10.1088/1757-899X/220/1/012001.
- [110] N.T. Aboulkhair, N.M. Everitt, I. Ashcroft, C. Tuck, Reducing porosity in AlSi10Mg parts processed by selective laser melting, Addit. Manuf. 1–4 (2014) 77–86. doi:10.1016/J.ADDMA.2014.08.001.

- [111] X. Shi, S. Ma, C. Liu, C. Chen, Q. Wu, X. Chen, J. Lu, Performance of high layer thickness in selective laser melting of Ti6Al4V, *Materials* (Basel). 9 (2016) 1–15. doi:10.3390/ma9120975.
- [112] ASTM, Standard Test Method for Density of Powder Metallurgy (PM) Materials Containing Less Than Two Percent Porosity 1, (2017). doi:10.1520/B0311-17.
- [113] ASTM, Standard Practice for Reporting Data for Test Specimens Prepared by Additive Manufacturing 1, (2014). doi:10.1520/F2971-13.
- [114] Designation: E8/E8M – 16a Standard Test Methods for Tension Testing of Metallic Materials 1, (n.d.). doi:10.1520/E0008_E0008M-16A.
- [115] S. Zia Uddin, D. Espalin, J. Mireles, P. Morton, C. Terrazas, S. Collins, L.E. Murr, R. Wicker, Laser powder bed fusion fabrication and characterization of crack- free aluminum alloy 6061 using in-process powder bed induction heating, in: *Solid Free. Fabr. Symp.*, Austin, TX, 2016: pp. 214–227.
- [116] G. Liu, L.E. Murr, C.-S. Niou, J.C. McClure, F.R. Vega, Microstructural aspects of the friction-stir welding of 6061-T6 aluminum, *Scr. Mater.* 37 (1997) 355–361. doi:10.1016/S1359-6462(97)00093-6.
- [117] ASM Handbook; Properties and Selection: Nonferrous Alloys and Special-Purpose Materials, in: ASM INTERNATIONAL, 1991.
- [118] L. Thijs, K. Kempen, J.-P. Kruth, J. Van Humbeeck, Fine-structured aluminium products with controllable texture by selective laser melting of pre-alloyed AlSi10Mg powder, *Acta*

- Mater. 61 (2013) 1809–1819. doi:10.1016/J.ACTAMAT.2012.11.052.
- [119] N.C.W. Kuijpers, W.H. Kool, P.T.G. Koenis, K.E. Nilsen, I. Todd, S. van der Zwaag, Assessment of different techniques for quantification of α -Al(FeMn)Si and β -AlFeSi intermetallics in AA 6xxx alloys, Mater. Charact. 49 (2002) 409–420. doi:10.1016/S1044-5803(03)00036-6.
- [120] M. Gao, J. Qiao, High-Entropy Alloys (HEAs), Metals (Basel). 8 (2018) 108. doi:10.3390/met8020108.
- [121] N. Coniglio, C.E. Cross, Initiation and growth mechanisms for weld solidification cracking, Int. Mater. Rev. 58 (2013) 375–397. doi:10.1179/1743280413Y.0000000020.
- [122] M. Rappaz, J. Drezet, M. Gremaud, A New Hot-Tearing Criterion, Metall. Mater. Trans. 30 (1999) 449–455.
- [123] L.E. Murr, E. Martinez, K.N. Amato, S.M. Gaytan, J. Hernandez, D.A. Ramirez, P.W. Shindo, F. Medina, R.B. Wicker, Fabrication of metal and alloy components by additive manufacturing: Examples of 3D materials science, J. Mater. Res. Technol. 1 (2012) 42–54. doi:10.1016/S2238-7854(12)70009-1.
- [124] P. Frigola, O.A. Harrysson, T.J. Horn, H.A. West, R.L. Aman, J.M. Rigsbee, D.A. Ramirez, L.E. Murr, F. Medina, R.B. Wicker, E. Rodriguez, Fabricating Copper Components with Electron Beam Melting, 2014. www.arcam.com/CommonResources/Files/www.arcam.com/ (accessed October 31, 2018).
- [125] T.H. Fletcher, L.L. Baxter, D.K. Ottesen, SPECTRAL EMISSION CHARACTERISTICS

- OF SIZE-GRADED COAL PARTICLES*, n.d. https://web.anl.gov/PCS/acsfuel/preprintarchive/Files/32_3_NEW_ORLEANS_08-87_0042.pdf (accessed October 31, 2018).
- [126] L. Li, K. Yu, K. Zhang, Y. Liu, Study of Ti-6Al-4V alloy spectral emissivity characteristics during thermal oxidation process, *Int. J. Heat Mass Transf.* 101 (2016) 699–706. doi:10.1016/j.ijheatmasstransfer.2016.05.069.
- [127] S.S. Sih, J.W. Barlow, Emissivity of powder beds, 6th Solid Free. Fabr. Symp. (1995) 402–408.
- [128] S.S. Sih, J.W. Barlow, The prediction of the emissivity and thermal conductivity of powder beds, *Part. Sci. Technol.* 22 (2004) 427–440. doi:10.1080/02726350490501682.
- [129] O. Rozenbaum, D. De Sousa Meneses, P. Echegut, Texture and Porosity Effects on the Thermal Radiative Behavior of Alumina Ceramics, *Int. J. Thermophys.* 30 (2009) 580–590. doi:10.1007/s10765-008-0510-1.
- [130] AAA Air Support, What are 7075, 2024 and 6061 Aluminum Alloys? - AAA Air Support, (n.d.).
- [131] W.A. Grell, E. Solis-Ramos, E. Clark, E. Lucon, E.J. Garboczi, P.K. Predecki, Z. Loftus, M. Kumosa, Effect of powder oxidation on the impact toughness of electron beam melting Ti-6Al-4V, *Addit. Manuf.* 17 (2017) 123–134. doi:10.1016/J.ADDMA.2017.08.002.
- [132] M. Björck, R. Elger, S. Kimab, Oxidation kinetics of copper at reduced oxygen partial pressures, 2013. http://www.skb.se/wp-content/uploads/2015/05/Bilaga-t-1371851_1410172-Oxidation-kinetics-of-copper-at-reduced-oxygen-partial-pressures.pdf

(accessed November 3, 2018).

[133] madur - Gas Analysers, (n.d.). http://www.madur.com/index.php?page=/partial_pressure
(accessed November 3, 2018).

[134] S. Hitoshi, T. Toshihide, N. Keiji, Effect of Oxygen Partial Pressure on Oxidation of Iron at 573 K, J. Nucl. Sci. Technol. 21 (1984) 844–852. doi:10.1080/18811248.1984.9731123.

Appendix A Data on AA6061 Parameter Development

SLM fabrication of aluminum alloy 6061; Parameter for 10mm(on all side) cubes

Experiment 1; Date: 2/10/17

Induction heating (°C)	Layer thickness (μm)	Hatch Spacing (μm)	Power (W)	Scan speed (mm/s)	%Relative density
350	30	100	150	1800	
350	30	100	200	1800	
350	30	100	250	1800	96.99
350	30	100	300	1800	
350	30	120	150	1800	
350	30	120	200	1800	
350	30	120	250	1800	
350	30	120	300	1800	
350	30	140	150	1800	
350	30	140	200	1800	
350	30	140	250	1800	
350	30	140	300	1800	98.07

350	30	160	150	1800	98.27
350	30	160	200	1800	97.30
350	30	160	250	1800	
350	30	160	300	1800	

Experiment 2; Date:2/16/17

Induction heating	Layer thickness	Hatch Spacing	Power (W)	Scan speed	%Relative density
(°C)	(μm)	(μm)		(mm/s)	
350	30	140	350	2800	97.01
350	30	140	300	2000	97.51
350	30	140	250	2000	97.36
350	30	100	250	2000	97.65
350	30	140	300	2500	97.28
350	30	140	250	2500	96.71
350	30	100	250	2500	97.98
350	30	140	350	2200	96.65
350	30	140	150	2000	94.02
350	30	100	150	2000	95.06
350	30	140	300	2800	96.23
350	30	140	150	1500	95.30
350	30	100	150	1500	96.03

Experiment 3; Date:2/24/17

Induction	Layer	Hatch	Scan		
heating	thickness	Spacing	speed		
(°C)	(μm)	(μm)	Power (W)	(mm/s)	%Relative density
350	30	140	350	2500	97.97
350	30	120	350	2500	98.61
350	30	100	350	2500	97.93
350	30	80	350	2500	97.85
350	30	140	350	2500	97.44
350	30	120	350	2500	98.01
350	30	100	350	2500	97.27
350	30	80	350	2500	97.71
350	30	140	350	2500	96.65
350	30	120	350	2500	97.01
350	30	100	350	2500	95.79
350	30	80	350	2500	97.55
350	30	140	350	2500	98.24
350	30	120	350	2500	97.31
350	30	100	350	2500	97.79
350	30	80	350	2500	97.77

Experiment 4; Date:3/2/17

Induction	Layer	Hatch	Scan		
heating	thickness	Spacing	speed		
(°C)	(μm)	(μm)	Power (W)	(mm/s)	%Relative density
0	30	140	350	2500	94.49

0	30	120	350	2500	96.54
0	30	100	350	2500	93.93
0	30	80	350	2500	94.71
0	30	140	350	2500	94.13
0	30	120	350	2500	95.55
0	30	100	350	2500	93.97
0	30	80	350	2500	94.51
0	30	140	350	2500	91.00
0	30	120	350	2500	95.17
0	30	100	350	2500	91.31
0	30	80	350	2500	92.16
0	30	140	350	2500	97.90
0	30	120	350	2500	98.08
0	30	100	350	2500	97.38
0	30	80	350	2500	97.24

Experiment 5; Date:3/8/17

Induction	Layer	Hatch	Scan		
heating	thickness	Spacing	speed		
(°C)	(μm)	(μm)	Power (W)	(mm/s)	%Relative density
350	30	140	350	1300	Density was not measured due to the discover of crack
350	30	140	310	2000	
350	30	120	350	2400	
350	30	120	330	2500	
350	30	140	350	1500	

350	30	140	330	2000
350	30	120	350	2300
350	30	120	330	2500
350	30	80	250	2200
350	30	80	250	2400
350	30	80	290	2500
350	30	80	270	2500
350	30	140	350	1700
350	30	140	350	2000
350	30	120	350	2200
350	30	120	370	2500
350	30	140	350	1900
350	30	140	370	2000
350	30	120	350	2100
350	30	120	390	2500

Experiment 6; Date:3/15/17

Induction	Layer	Hatch		Scan
heating	thickness	Spacing		speed
(°C)	(μm)	(μm)	Power (W)	(mm/s)

%Relative density

Experiment Failed

Experiment 7; Date:4/4/17

Induction heating	Layer thickness	Hatch Spacing	Power (W)	Scan speed	%Relative density
(°C)	(μm)	(μm)		(mm/s)	
150>200					
(after 35 layers)					
500	100	80		500	
500	100	80	250	800	
500	100	80	310	1000	
500	100	80	370	1200	
190>240(after 35 layers)					
500	100	100		500	
500	100	100	310	800	Density was not
500	100	100	380	1000	measured
500	100	100	450	1200	because we were
230>280					
(after 35 layers)					
500	100	120		500	
500	100	120	370	800	
460>400(after 31 layers)					
500	100	120		1000	
550>400(after 31 layers)					
500	100	120		1200	
270>300(after 35 layers)					
500	100	140		500	

500	100	140	430	800
-----	-----	-----	-----	-----

530>400(after

500	100	140	31 layers)	1000
-----	-----	-----	------------	------

640>400(after

500	100	140	31 layers)	1200
-----	-----	-----	------------	------

Experiment 8; Date:4/11/17; Remelting was done; Parameters repeated from experiment 3

Induction heating	Layer thickness	Hatch Spacing	Scan speed		
(°C)	(μm)	(μm)	Power (W)	(mm/s) %Relative density	
400	30	140	350	2500	
400	30	120	350	2500	
400	30	100	350	2500	
400	30	80	350	2500	
400	30	140	350	2500	
400	30	120	350	2500	
400	30	100	350	2500	Cracks were still
400	30	80	350	2500	observed
400	30	140	350	2500	
400	30	120	350	2500	
400	30	100	350	2500	
400	30	80	350	2500	
400	30	140	350	2500	
400	30	120	350	2500	

400	30	100	350	2500
400	30	80	350	2500

Experiment 9; Date:4/20/17; Energy densities were kept same

Induction heating (°C)	Layer thickness (μm)	Hatch Spacing (μm)	Power (W)	Scan speed (mm/s)	%Relative density
500	70	80	108	500	
500	70	80	173	800	
500	70	80	217	1000	
500	70	80	360	1200	
500	70	100	140	500	
500	70	100	217	800	
500	70	100	270	1000	
500	70	100	325	1200	
500	70	120	162	500	
500	70	120	260	800	
500	70	120	325	1000	
500	70	120	390	1200	

Build
Failed
partially
crack
free
Metallagrophy
not
performed
Cracked

500	70	140	190	500
500	70	140	304	800
500	70	140	380	1000
500	70	140	450	1200

Experiment 10; Date:5/8/17;

Induction heating	Layer thickness	Hatch Spacing	Scan speed				Com
(°C)	(μm)	(μm)	Power (W)	(mm/s)	%Relative density		ment
500	70	120	350	110	99.47		Crack
500	70	140	390	1300	98.54		s are
500	70	140	410	1200	98.37		there
500	70	140	350	1100	98.64		. Not
500	70	120	410	1200	98.39		all of
500	70	140	410	1300	98.70		them
500	70	140	370	1200	98.50		.I
500	70	140	400	1100	98.67		think
500	70	120	400	1300			need
500	70	140	400	1300	98.46		to do
500	70	140	200	400	98.81		meta
500	70	140	230	500	98.95		llogra
500	70	120	200	400	99.23		phy
500	70	140	475	1300	97.76		on
500	70	140	225	400	98.72		

500	70	140	270	500	99.18	the rest
-----	----	-----	-----	-----	-------	----------

Experiment 12; Date:5/30/17;

Induction heating	Layer thickness	Hatch Spacing	Scan speed	Power (W)	(mm/s)	%Relative density	Comment
(°C)	(μm)	(μm)					
500	100	140	350	1200		97.50	
500	100	140	350	1400		97.96	
500	100	140	350	1600		97.26	
500	100	140	350	1800		97.85	
500	100	140	350	2000		95.98	
500	100	140	400	1200		97.77	
500	100	140	400	1400		98.69	
500	100	140	400	1600		97.42	All
500	100	140	400	1800		97.10	crack
500	100	140	400	2000		98.06	free
500	100	140	450	1200			
500	100	140	450	1400		97.60	
500	100	140	450	1600		96.46	
500	100	140	450	1800		97.16	
500	100	140	450	2000		97.32	
500	100	140	500	1200			
500	100	140	500	1400		97.84	

500	100	140	500	1600	96.97
500	100	140	500	1800	97.13
500	100	140	500	2000	98.08

Experiment 13; Date:6/14/17

Induction	Layer	Hatch	Scan			Com
heating	thickness	Spacing	speed			
(°C)	(μm)	(μm)	Power (W)	(mm/s)	%Relative density	ment
500	100	140	360	1300	97.75	
500	100	140	360	1400	97.84	
500	100	140	360	1450	98.24	
500	100	140	360	1900	97.80	
500	100	140	360	2000	97.81	
500	100	140	360	2200	97.72	
500	100	140	380	1300	98.52	
500	100	140	380	1400	97.81	
500	100	140	380	1450	97.93	
500	100	140	380	1900	97.88	
500	100	140	380	2000	98.11	
500	100	140	380	2200	97.77	
500	100	140	420	1300	98.01	
500	100	140	420	1400	97.29	
500	100	140	420	1450	98.00	
500	100	140	420	1900	97.27	

500	100	140	420	2000	97.68
500	100	140	420	2200	97.93
500	100	140	440	1300	97.41
500	100	140	440	1400	97.69
500	100	140	440	1450	97.61
500	100	140	440	1900	97.40
500	100	140	440	2000	97.67
500	100	140	440	2200	98.10

Experiment 14,15,16; Date:6/14,20,24/17; Printing tensile bars

Induction	Layer	Hatch		Scan		
heating	thickness	Spacing		speed		Com
(°C)	(μm)	(μm)	Power (W)	(mm/s)	%Relative density	ment

Failed

Appendix B Pyrometer Measurements and Calculations

MATLAB® scripts:

```
-----START-----  
  
File name:  import_raw_data_in_series_to_calculate_temp.m  
  
clear variables;  
close all;  
clc  
  
%% To read all files that match *.dat using importdata function:  
dataFiles = dir('*.dat');  
numfiles = length(dataFiles);  
mydata = cell(1, numfiles);  
  
%% To sort data and calculate the temperature  
for k = 1:numfiles  
    A = importdata (dataFiles(k).name); % Reads all the data row and column-  
wise from the .dat files  
    B=A(:, [1 4]); % Selects the column 1 [wavelengths] and column 4  
[corrected intensity]  
    out = B(all(B>=1200,2),:); % excludes all the data below the wavelength  
of 1200 nm  
    B1 = out(:,1); % wavelength vector  
    B2 = out(:,2); % intensity vector  
    [p]=polyfit(B1,B2,2); % Fitting a 2nd order polynomial to the data  
    % to find intensity and  
    y = [1200:50:1600]; % Calculate intensity values at wavelengths 1200 to  
1600 nm  
    % in intervals of 50 nm
```

```

ysize= length(y);    % At how many points wavelength is sampled

e = [];              % Matrix 'e' will store the intensity values
calculated

                        % at the selected wavelengths

for i = 1:ysize
    e(i) = temp_prediction(p(1),p(2),p(3),y(i)); % This function would
calculate
                                                    % the intensity values
                                                    % according to the
fitted polynomial

end

e=e';                % vectorizing the data
y=y';

ysize = length(y);
esize = length(e);

T = [];              % This matrix will store the temperature
for i = 1:1:ysize    % Loop to apply Planck's law to the wavelength
and intensity
                        % pairs to calculate T_12,T_13,...T_(n-1)n
    for j = ysize:-1:2
        if i~=j
            T(i,j)= plancks_law(y(i),y(j),e(i),e(j));
        else break
    end
end
end

```

```

end

s = nonzeros(T);

% Tavg (k) = mean2(T);

savg (k) = mean2(s);          % Taking an average value of the calculated temp.

and

                                % reporting as the consensus temp which I
                                % believe is not the correct way to do it i.e
                                % NOT the correct way to find the consensus
                                % temp

end

% Tavg = Tavg';

savg = savg';

% fileID = fopen('temperature.txt','w');

% fprintf(fileID, 'Calculated Temp\n\n');

%

% fprintf(fileID,'%6.2f %12f\n', savg,Tavg);

```

-----END-----

File name: plancks_law.m

-----START-----

```

function T = plancks_law(y1,y2,i1,i2)

c2 = 1.438e7; %second constant

a = 1/y1; %reciprocal of the second wavelength

b = 1/y2; %reciprocal of the first wavelength

```

```
ir = i1/i2;
```

```
wr = b/a;
```

```
numerator = c2*(b-a);
```

```
denominator1 = log(ir);
```

```
denominator2 = 5*log(1/wr);
```

```
denominator = denominator1 - denominator2;
```

```
T = (numerator)/(denominator);
```

```
-----END-----
```

```
File name: temp_prediction.m
```

```
-----START-----
```

```
function e = temp_prediction(a,b,c,x)
```

```
e = a*x^2 + b*x + c;
```

```
-----END-----
```

Appendix C Permission to Reuse Published Article in Chapter 5

Email correspondences:

From: Uddin, Syed Zia <suddin@miners.utep.edu>
Sent: Tuesday, October 9, 2018 2:53 AM
To: Permissions Helpdesk <permissionshelpdesk@elsevier.com>
Subject: About reusing articles in thesis

*** External email: use caution ***

Dear concern,

I obtained the right to use my article for my thesis using Rightslink as shown in the screenshot:



The screenshot displays the Elsevier RightsLink interface. At the top, there is a navigation bar with the Copyright Clearance Center logo, the RightsLink® title, and links for Home, Account Info, Help, and an email icon. Below this, the user is logged in as Syed Zia Uddin, with a Logout button. The main content area shows details for a specific article: Title (Processing and characterization of crack-free aluminum 6061 using high-temperature heating in laser powder bed fusion additive manufacturing), Author (Syed Z. Uddin, Lawrence E. Murr, Cesar A. Terrazas, Philip Morton, David A. Roberson, Ryan B. Wicker), Publication (Additive Manufacturing), Publisher (Elsevier), and Date (August 2018). A copyright notice at the bottom of this section states "© 2018 Elsevier B.V. All rights reserved." Below the article details, a paragraph explains the user's rights as the author, noting that they retain the right to include the article in a thesis or dissertation, provided it is not published commercially. It also provides a link to the Elsevier copyright policy. At the bottom of the interface, there are buttons for BACK and CLOSE WINDOW, and a footer with copyright information and contact details for the Copyright Clearance Center, Inc.

Copyright © 2018 Copyright Clearance Center, Inc. All Rights Reserved. [Privacy statement](#) [Terms and Conditions](#)
Comments? We would like to hear from you. E-mail us at customerservice@copyright.com

My school publishes the thesis using ProQuest who ask for a fee to anyone trying to access the full version of the thesis. Under the circumstances, would I be violating part of the above clause (“provided it is not published commercially”) which is red marked in the picture if I use my article in my thesis verbatim? Your support is much appreciated.

Thanks,

Syed Zia Uddin

Graduate Research Assistant

W.M. Keck Center for 3D Innovation

Department of Mechanical Engineering

The University of Texas at El Paso

500 W University Ave., El Paso, TX-79902

Cell Phone: (915) 356 8889

suddin@miners.utep.edu

Reply

Dear Syed,

As an Elsevier journal author, you retain the right to Include the article in a thesis or dissertation (provided that this is not to be published commercially) whether in part or in its entirety, subject to proper acknowledgment; see <https://www.elsevier.com/about/our-business/policies/copyright/personal-use> for more information. As this is a retained right, no written permission from Elsevier is necessary.

As outlined in our permissions licenses, this extends to the inclusion of your thesis in ProQuest's Dissertation on Demand services:

19. Thesis/Dissertation: If your license is for use in a thesis/dissertation your thesis may be

submitted to your institution in either print or electronic form. Should your thesis be published commercially, please reapply for permission. These requirements include

permission for the Library and Archives of Canada to supply single copies, on demand, of

the complete thesis and include permission for Proquest/UMI to supply single copies, on demand, of the complete thesis.

Should your thesis be published commercially, please reapply for permission. Theses and dissertations which contain embedded PJAs as part of the formal submission can be posted publicly by the awarding institution with DOI links back to the formal publications on ScienceDirect.

Best of luck with your thesis and best regards,

Laura

Laura Stingelin

Permissions Helpdesk Associate

ELSEVIER | Global E-Operations Books

+1 215-239-3867 office

l.stingelin@elsevier.com

Contact the Permissions Helpdesk

+1 800-523-4069 x3808 | permissionshelpdesk@elsevier.com

Vita

Syed Zia Uddin was born in Gouripur, a small town 120 miles north to the capital of Bangladesh. He was born to Syed Golam Sorwar and Arshade Begum. After attending elementary and high school in Gouripur, he got an opportunity to study engineering at country's most prestigious school, Bangladesh University of Engineering and Technology in Dhaka. He graduated with a bachelor's degree in Mechanical Engineering in March 2016 and attended The University of Texas at El Paso for master's beginning the fall of 2016. During his master's in Mechanical Engineering, he worked as a graduate research assistant at W. M. Keck Center of 3D Innovation. He authored a conference and a journal article with research on laser assisted 3D printing of aluminum 6061 alloy. During the latter days, he worked on temperature measurement of metal alloys using multi wavelength pyrometry.

Permanent address: 346 Uttar Bazar, Gouripur

Mymensingh-2270, Bangladesh.

syedzia.buet@gmail.com

This thesis was typed by Syed Zia Uddin